Mechanical Perturbation and Stimulation of *Drosophila* Wing Imaginal Discs

---

Dissertation

zur

Erlangung der naturwissenschaftlichen Doktorwürde

(Dr. sc. nat.)

vorgelegt der

Mathematisch-naturwissenschaftlichen Fakultät

der

Universität Zürich

von

Thomas Schluck

aus

Deutschland

Promotionskomitee

PD Dr. Christof Aegerter (Vorsitz)
Prof. Dr. Hugo Keller
Prof Dr. Damian Brunner

Zürich, 2014

Contents

Introduction v

1 Biological Backgrounds 1
- 1.1 Principles in Development . . . 1
  - 1.1.1 Cell Differentiation . . . 1
  - 1.1.2 Pattern Formation and Morphogenesis . . . 2
  - 1.1.3 Growth and Size Control . . . 3
- 1.2 Development of Drosophila melanogaster . . . 6
  - 1.2.1 Embryogenesis of Drosophila . . . 7
- 1.3 Organogenesis of Imaginal Discs . . . 10
- 1.4 The Wing Imaginal Disc . . . 10
  - 1.4.1 Patterning and Morphogenesis . . . 11
  - 1.4.2 Growth and Size Control . . . 14
- 1.5 Growth Models . . . 14
  - 1.5.1 Memory, Threshold and Inhibitor Model . . . 15
  - 1.5.2 The Opposing Growth Pathways Model . . . 15
  - 1.5.3 The Spatial Gradient Model . . . 15
  - 1.5.4 The Temporal Gradient Model . . . 16
  - 1.5.5 Mechanical Feedback Models . . . 16

2 Experimental Setup and Methods 20
- 2.1 Experimental Setup . . . 20
  - 2.1.1 Relation between Seflection and Force . . . 21
  - 2.1.2 Calibration of the Cantilever Setup . . . 23
  - 2.1.3 Experimental Preparations . . . 26
- 2.2 Materials and Methods . . . 26

3 Elastic Properties of the Tissue 28
- 3.1 Force-Extension Measurements . . . 30
- 3.2 Poisson's ratio of the Wing Imaginal Disc . . . 32
- 3.3 Stress-Strain Measurements . . . 35
- 3.4 Determinaton of the Photo-Elastic Constant . . . 40
- 3.5 Dynamical Response of the Wing Imaginal Disc . . . 47

4 Mechanical Regulation of Growth 53

5 Summary 58

Curriculum Vitae 60

Acknowledgments 61

Abstract

Growth regulation and growth cessation of developing tissue are still open and actual questions in the field of developmental biology. A well established model system to approach these questions and gain an understanding about growth is the *Drosophila* wing imaginal disc. Based on this model system many theories have been proposed to explain the growth in this mostly autonomous growing organ of the larva. Most of these growth models have been shown to be incomplete or have been rejected by experimental data. However, in recent years it was proposed to consider the physical constrains of a developing tissue as a possible growth regulator like the mechanical forces between the tissue's cells. Models based on this assumption have been very successful in explaining the growth in the wing imaginal disc.
In this thesis the mechanical properties and mechanical constrains of the wing imaginal disc were studied with regard to the main basic assumptions of the so-called "mechanical feedback models". These basic assumptions are, that mechanical stress accumulates within the wing imaginal disc due to growth and that this stress in return regulates growth. To test these assumptions a stretching device was developed and built, which allowed to exert a known and adjustable uniaxial force on wing imaginal discs. The applicable forces are in the order of 10 µN to 1000 µN. Concurrently the tissue's mechanical response was monitored by microscope. The conducted experiments allowed to determine the tissue's effective spring constant, Young's modulus, Poisson-ratio, photo-elastic constant and timescale of its visco-elastic response. The wing imaginal disc was found to be highly elastic, i.e. showing no plasticity and obeyed Hooke's law. Its response time to an external temporary straining is in an order of magnitude, that allows accumulation of stress via proliferation and simultaneously damps very short termed mechanical perturbations. By stress-birefringence measurements the absolute stress values for different areas, namely the wing disc proper and hinge-notum region, of the wing imaginal disc have been quantified. Finally, wing imaginal disc were stimulated to proliferation by stretching the tissue and thereby providing experimental evidence for a relation between tensile stress and growth promotion.

Zusammenfassung

Wachstumsregulation und Wachstumsstop von sich entwickelndem Gewebe sind weiterhin aktuelle und ausstehende Fragen der Entwicklungsbiologie. Ein fest etabliertes Modellsystem, um sich diesen Fragen zu nähern und ein Verständnis für Wachstum zu gewinnen, ist die Imaginalscheibe des Flügels der *Drosophila*. Fußend auf diesem Modellsystem wurden etliche Theorien vorgeschlagen, um das Wachstum innheralb dieses vornehmlich autonom wachsenden Organ der Larve zu erklären. Die meisten dieser Wachstumsmodelle zeigten sich jedoch ungenügend oder wurden von experimentellen Befunden widerlegt. In den letzten Jahren wurde vorgeschlagen, die physikalischen Randbedingungen eines sich entwickelnden Gewebes als einen möglichen Wachstumsregulator in Betracht zu ziehen, wie etwa die mechanischen Kräfte, die zwischen den Zellen des Gewebes herrschen. Modelle, die auf dieser Annahme basieren, konnten das Wachstum in der Imaginalscheibe des Flügels erfolgreich beschreiben.
In dieser Doktorarbeit wurden nun die mechanischen Eigenschaften und Randbedingungen der Imaginalscheibe des Flügels im Hinblick auf die Hauptannahmen solcher sogenannten "mechanischen Feedback-Modelle" untersucht. Um diese Annahmen auf die Probe zu stellen wurde eine Zugvorrichtung entwickelt und gebaut, die es erlaubte eine bekannte und einstellbare uniaxiale Kraft auf Imaginalscheiben des Flügels auszuüben. Die anlegbaren Kräfte waren in einer Grössenordnung von 10 µN bis 1000 µN einstellbar. Gleichzeitig wurde die mechanische Antwort des Gewebes mittels eines Mikroskops beobachtet. Die damit durchgeführten Experimente ermöglichten es folgende Eigenschaften der Imaginalscheibe des Flügels zu bestimmen. Ermittelt wurden die effektive Federkonstante, das Young's–Modul, die Poisson-Zahl, die photoelastische Konstante und die Zeitskale ihrer visko-elastischen Antwort. Die Imaginalscheibe des Flügels erwies sich hochelastisch und gehorchte dem Hookeschem Gesetz. Die Zeitskala ihrer mechanischen Reaktion auf kurzzeitige externe Dehnungen wurde in einer Grössenordnung gefunden, die es erlaubt mechanische Spannungen aufgrund von Proliferation zu akkumulieren und kurzzeitige mechanische Störungen zu dämpfen und damit auszuschließen. In Spannungs-Doppelbrechungsmessungen wurden die Absolutwerte der mechanischen Spannungen unterschiedlicher Gebiete bestimmt, und zwar die der sogenannten Pouch und der Scharnier-Notum Region. Zuletzt wurden Flügelscheiben durch mechanische Streckung des Gewebes zu Zellteilungen angeregt und damit der experimentelle Nachweis für einen Zusammenhang zwischen Zugspannung und Wachstumsanregung erbracht.

Introduction

What regulates growth and determines the size of an organ?
This is a lasting question in developmental biology, that fueled the endeavors of researches for many years and although a host of knowledge on intracellular signaling pathways has been accumulated, several issues in organ growth are still unanswered. Probably due to these kind of intractable conundrums the focus in biological investigations has shifted from a single gene perspective to a more holistic and systemic approach, in which the questioned process is described and simulated by mathematical models [1]. These models' main feature is the quantitative description of the entire system, which is why they depend on a quantitative data of the investigated system and thus set higher standards to the experiment.
To tackle the unsolved question on growth control, models predicated on one of the most prominent model systems in biology [2], the wing imaginal disc of *Drosophila melanogaster*, have been developed the past few years [3]. The wing imaginal disc is a proto-organ that develops into the wing of the adult fly during metamorphosis and originates from a cluster of about 30 cells in the embryo [4] and grows into a two-dimensional ephitelial tissue of approximately 30000 cells by the end of larval development [5]. Growth in the wing imaginal disc almost exclusively takes place via cell proliferation and the final size of this larval structure largely predetermines the size of the adult wing [6].
The emergence of patterns in the wing imaginal disc is fairly well understood and can be explained as an interplay of extracellular proteins, which are known as morphogens and form spatial concentration gradients within the ephitelial tissue. These concentration gradients are highest in the middle of the tissue and decrease to the periphery, thereby providing spatial information. Besides their fundamental role in organ patterning, morphogens also have been shown to be of great influence on growth via different biochemical pathways, such that they also act as growth factors [7].
Two observations concerning growth in the wing imaginal disc stimulated scientific investigations for years. Firstly, the wing imaginal disc autonomously ceases its growth at a certain size of the organ. This is known from dissected wing imaginal discs, that were cultured in the abdomen of female flies and stopped growing without any external cue, when they reached the size of non-dissected discs in larvae [4]. Secondly, cell proliferation is roughly uniform throughout the imaginal tissue and thus shows no direct, respectively observable relation to the spatial morphogen concentration gradients [8, 9, 10]. In order to explain the spatially uniform distributed growth as well as the cessation of growth at a certain size, models were proposed which consider complementary growth modulators like mechanical stress between the cells of the tissue [11, 12, 13, 14, 15].
The thesis presented here addressed the mechanical feedback model of Aegerter-Wilmsen et al. who assumed in [13], that growth is induced when cells are experiencing tensile stresses and that cells which experience compressional stresses are inhibited in growth. This model can explain the observed growth distribution within the wing imaginal disc and the autonomous cessation of growth when the organ reached a certain size. According to the model, growth is biochemically promoted in the center, which in turn leads to a distribution of compressional stresses in the center and net tensional stresses in the peripheral regions. While the high morphogen concentration in the center promotes growth it is simultaneously antagonized by the present compressional stresses. Accordingly, the tensile stresses in the peripheral regions stimulate cell proliferation and thus compensate for the absence of any biochemical growth promoter. The larger the disc becomes, the larger becomes the peripheral region and thus the total mass compressing the centre of the disc. When the total compression reaches a certain threshold, proliferation in the center ceases and therefore in the whole disc.

This mechanical feedback model is based on two non-trivial assumptions:

1. Mechanical stress accumulates over time within the tissue due to growth.
2. Growth is regulated by mechanical stress.

Assumption one is supported by several publications. Firstly, photo-elastic measurements of the wing imaginal discs were used to retrieve information about the peak retardance distribution in the wing imaginal disc during its development [16].[1] The peak retardance was used as a read-out of the tissues internal stress distribution. This experiment has shown an inhomogeneous retardance distribution, that increases during the development of the wing imaginal disc. However, due to the lack of the photo-elastic constant C a quantitative determination of the occuring stresses in the tissue was not possible. Secondly, Ishihara et. al. [17] used Bayesian statistics to estimate the tension of cell contacts in the wing imaginal disc. Starting from experimentally determined geometries of the cells they found a negative correlation of apical cell area and compressional stress. Thirdly, deformation of the apical cell area and the strain of the cells were determined by Aegerter-Wilmsen et al. [14]. The apical cell area and the cellular deformation were determined using image analysis on images of apical cell outlines retrieved by fluorescent confocal microscopy. They found a circumferential direction of the strain in the proximal region and a reduction in apical cell area in the center of the imaginal discs, similar to Ishihara et. al. [17]. Studies to test assumption two directly were not done so far.

The objective of the thesis presented here is the investigation of the wing imaginal discs mechanical properties to scrutinize the eligibility of the mechanical feedback model and to offer quantitative data about the imaginal tissues general mechanical properties.
What are the wing imaginal tissue's mechanical characteristics? On what time scale a strain must be exceeded, such that stress builts up within the tissue? Assuming that mechanical forces do influence growth, is there any influence due to the peristaltic movement of the larva? Does tensile stress promote proliferation and compressional stress inhibit proliferation?
I have addressed these questions experimentally by stretching wing imaginal discs in-vitro. For this purpose I designed and built a forcing apparatus that allowed the application of an uniaxial force in the order of $10\,\mu\text{N} - 1000\,\mu\text{N}$. The apparatus mainly consists of a cantilever beam, which is bent in a controlled manner and thereby exerts a controlled force. The setups dimensions were kept small enough to be installed on any inverted microscope, such that the organs response to the mechanical perturbation could be monitored simultaneously. The setup and the experimental procedure are described in detail in chapter 2. Chapter 3 describes how wing imaginal discs were stretched in a step-wise manner, i.e. in steps of the applied force, such that the average Young's modulus E and Poisson-ratio ν could be inferred, namely for the hinge-notum and pouch region of the wing imaginal disc. Similarly, the pulling setup was used in combination with a polarization microscope to perform stress-birefringence measurements. This allowed the identification of the tissues photo-elastic constant C of the tissue and in turn the quantification of the stresses in unperturbed late third instar discs (chapter 3.4). In chapter 3.5 elongation and release experiments on the wing imaginal disc are described, which shed some light on the dynamical response of the tissue and revealed the time-scale τ on which a strain is transferred into stress. Finally, wing imaginal discs were constantly stretched over the time course of one hour and their proliferation rates concurrently monitored, such that a direct link between proliferation rate and tensile stress could be established. Details about these experiments can be found in the last chapter 4.

A concise introduction into the basic concepts of developmental biology (section 1.1) and the development of the fly (section 1.2) will be preceeded before pattern formation (section 1.4.1) and growth (section 1.4.2) in the wing imaginal disc will be presented.

[1] In these experiments the wing imaginal discs were perpendicularly illuminated with polarized light, which became shifted in phase due to the birefringent property of the tissue. The phase shift equals a retardation of the light and is proportional to the mechanical stress within the tissue.

1 Biological Backgrounds

1.1 Principles in Development

Development is the coordinated process of cell behavior and cell specification in space and time. Research in the field either concentrates on single cellular responses and behavior and their influence on development or on the regulation and emergence principles of multicellular structures like tissues, organs or whole organisms. Typically development is classified into the aspects of cell differentiation, pattern formation, morphogenesis and growth [18] and models can address one or several of these aspects. All models can be roughly classified into two main types. One very predominant approach is to see emergence of structure coming from biochemical reaction-diffusion processes, such that the shape and size of a tissue are the results of a "mechanical execution by the cells of a pre-existing chemical pattern" [19]. Another approach presumes cell mechanics to have a structuring and patterning function, such that chemical processes and cell mechanics complement each other. Then the geometry of a tissue is also controlled by cell mechanics [19, 20]. In the next chapters we will have a brief look on the different aspects of development.

1.1.1 Cell Differentiation

A multicellular organism consists of different types of cells, each of them having its own purpose. But all cells in the organism stem from one ancestor cell – the zygote – and therefore cells must somehow differentiate during the course of development, meaning they have to change their property and behavior dependent on their spatiotemporal position. The genome, i.e. the sum of genetic information, is certainly at the base of development and corresponds to the set of instructions to build the organism. Due to developmental cues cells express different sets of genes, i.e. produce different proteins, whereby their traits and eventually behavior changes. Regulatory proteins are such cues. They bind at the control regions of a gene and either repress or activate the transcription of a gene into messenger RNA (mRNA). The mRNA of a transcribed gene must then be further translated by ribosomes to obtain the target protein. Every step in this cascade is a potential place of intervention and control and even after translation a post-translational modification might be necessary to gain its biological function.
Still, the most important point in control is the initiation of transcription [21] and therefore the regulatory regions of developmental genes are divided into more or less independent control modules to ensure activation of these genes only at the right time and place in development.
Differentiation of a cell can be divided into two main states: Specialization and determination. When cells express different types of genes due to regulatory cues coming from their local environment they develop different types of traits and specialize for different types. But the specialization of a cell can be reversed if the local environment changes and thereby the regulatory cues change. As soon as a cell fixes its specialization it is fully determined to its type and inherits its traits to its descendants.
Cells must coordinate their behavior by means of intercellular signaling. This can be achieved via uptake of an extracellular diffusive molecule, direct transport of a molecule between two cells through gap junctions or direct linkage of complementary surface molecules. Furthermore, cells must memorize the received information and maintain the adjustments made. This requirement is either fulfilled by internal feedback-loops of gene expression [22] or chemical and structural changes in chromatin structure [23]. Depending on the sequential signals a cell received during its course of development it gradually differentiates into a distinct type. Differentiation may change a cell drastically in its physical characteristics,

gives a tissue its specific function and is an important aspect of pattern formation and morphogenesis as can be seen in boundary formation (see chapter 1.4.1) or gastrulation (see chapter 1.2.1). Beside the genetic cues that control cell differentiation the shape of a cell can be a cue for cell differentiation [24, 25] due to direct mechanical interaction with its environment [26].

1.1.2 Pattern Formation and Morphogenesis

In developmental biology pattern formation describes the emergence of spatially organized different cell activities in an initially rather unstructured and homogeneous system [27]. Therefore, it is necessary that a cell retrieves information about its position and the function it has to fulfill there. This can be achieved in a self-organized or boundary-organized manner.
In 1952 Turing predicted a chemical mechanism for self-organized pattern formation based on a reaction-diffusion mechanism [28]. He showed that non-uniform and stable concentration patterns can form in space and time, when two substances interact with each other and one of the substances diffuses faster than the other. Further work from Meinhardt et al. elaborated self-organized pattern formation as an interplay of a locally restricted self-enhancing activator and a long-range inhibitor [29, 30, 31].[1]
The activator has a non-linear positive effect on its own production rate and the production rate of its antagonist; the activator diffuses at a slower rate than the inhibitor and has a shorter half-value time. Thus, starting from homogeneously distributed activator and antagonist concentrations, a small asymmetry in activator/antagonist concentration is sufficient to be amplified and to form complex concentration patterns.
Such self-organized pattern depends on the geometry and size of the field. Whenever the differences in diffusion rates can take effect, patterns may occur. The consequence of this dependence and the fact that size and geometry are changing during development is that self-organized reaction-diffusion patterns are transient. To transfer the initial pattern into a more permanent state, a completive strategy must take over. Boundary-organized patterning by morphogen gradients fulfills this task. A morphogen is a substance that acts directly on cells and triggers different specific responses depending on the local concentration a cell is subjected to [32].[2]
To provide cells with spatial information using a morphogen, only a few specialized cells express the substance at a previously established landmark. The morphogen spreads from this local source and forms a spatial concentration gradient. Depending on concentration thresholds different target genes are activated [33],[3] such that cells can read out their position in relation to this landmark. These landmarks are often realized as cell lineage boundaries that are formed by two adjacent but not intermingling cell populations. Boundary formation is an important patterning process in the wing imaginal disc and will be discussed in more detail in chapter 1.4.1.
This kind of sequential patterning and subdivision by auto-catalysis and lateral inhibition, followed by long-range morphogen gradients, can be continued many times [30]. The patterns of investigated tissues often scale to their size, but scaling is not an intrinsic property of Turing processes neither can it easily be integrated [35, 36]. Morphogen concentration gradients do not give scaling naturally when based on the principle of diffusion. Nevertheless morphogen gradients like Dpp in the wing imaginal disc have been found to scale with field size and rather simple mechanisms for scaling have been proposed (see chapter 1.4.1).
While pattern formation can be seen as rather focused on the biochemical generation of pattern, morphogenesis has its focus on the formation of shape. In morphogenesis the behavior of a cell and its physical property are most important as they determine how cells connect to each other, exert forces

[1] One of Meinhardt's fundamental observations was, that all pattering mechanisms involve local activation and long-range inhibition. Even things like the patterns in sand dunes, where there are no chemicals.
[2] Originally, the term morphogen was invented by Turing describing substances that "are reacting chemically" and "which [...] are diffusing". He stated himself, that "the word being intended to convey the idea of a form producer" and "is not intended to have any very exact meaning" [28].
[3] Please refer to [34] for the possible principles how genes are switched on or off depending on a morphogen concentration threshold.

within the tissue and thereby build or change morphological structures, respectively patterns.
In epithelial tissues cells are closely bound together through different kind of junctions to maintain tissue integrity. Some of these junctions anchor a cell to the extracellular matrix or other cells, some facilitate transport of molecules and some seal gaps between cells, making the sheet impermeable [22, 23].
In animal development the formation of shape results from the rearrangements of cells and their directed movement due to cell growth, division, cell competition, apoptosis, which is the controlled removal of cells by programmed cell death, and cellular properties like its shape, adhesiveness and motility.
How important physical traits of cells and mechanical processes within a tissue can be for pattern formation, can be seen in cell sorting due to cell differentiation.
Cell sorting or the segregation of cells, which is most important for boundary formation, can be explained using a thermodynamical approach, also known as the differential adhesion hypothesis (DAH) [37].
In this model, tissue is compared to a liquid consisting of cells. The only generic properties of the cells are cohesion and mobility. Individual aspects of the cells like shape or their mechanics are neglected and the tissue in total is described by its surface tension [38]. While the surface tension of a liquid can be related to the cohesive interactions between molecules, the surface tension of the tissue is mainly related to the surface density of trans-membrane adhesion molecules like cadherin [38, 39]. According to the DAH different types of cells express different types of cadherins and preferably associate with cells expressing the same cadherins. This was experimentally confirmed in [39, 40]. On top of this, depending upon the relative strength of homophilic and heterophilic association,[4] reproducible configurations of different adjacent cell groups were observed in vitro corresponding to the prediction of the DAH [37, 39, 41]. The segregation of cells is thus comparable to the segregation of two immiscible fluids with different surface tensions [42].
However, the binding specifity of cadherins alone is not sufficient to fully explain cell sorting. Cell sorting was shown to become unspecific when cells expressing different types of cadherins were allowed to bind to different purified cadherin substrates instead being allowed to bind to other cells [43].
More sophisticated approaches like the differential interfacial tension hypothesis (DITH) [44, 45] take cell motility into account and thus consider the individual abilities of cells to generate mechanical tension through reorganization of their cytoskeleton and thereby influence their contact surface to neighbor cells [46]. Cell motility thus comprises a cell's ability to change its shape actively and its ability of migration.
Typical processes observed in morphogenesis are epiboly, the decrease in thickness and increase of area of a cellular layer; convergent extension, the narrowing of a tissue in width or height and extensions of it in length; and invagination, the spatial and temporal controlled buckling of a tissue. Apical constriction and basal and laminar lengthening of locally designated cells is the main driving force for invagination [47]. Epiboly and convergent extension are driven by overall changes of cell shape and intercalation [25], wherein cells change their position by anisotropic remodeling of their adhesive contacts [48].
Proliferative growth and morphogenesis very often happen simultaneously. Then a tissue's development depends very much on the coordination of growth and in return growth is a result of morphological regulation. How proliferation is controlled and coordinated during development is a contemporary question. [49].

1.1.3 Growth and Size Control

Growth is an increase in size and thus associated with an increase in mass and can be realized by the synthesis of cellular components. In multicellular organisms the deposition of extracellular material is a further possibility for growth, but the majority of an organism's mass distributes among cells. The size of an organism or organ thus mainly depends on cell mass and cell number.
Growth and proliferation, which is an increase in cell number, are sometimes used interchangeably,

[4] The binding affinity of similar or different molecules at the contacting cell surface [38]

although they describe two distinct processes [50, 51]. This is sometimes misleading and confusing, but derives from the circumstance, that cell growth is often coupled to cell-cycle progression. In other words, most proliferating cells first grow, duplicate their content and then divide.[5]
A unicellular organism like yeast will reproduce as rapidly as possible under the given environmental condition and each individual maintains a constant mean size. Yeast controls cell division by a cell size check-point and only when the weight of a cell exceeds a given threshold the cell-cycle may proceed [52, 53].
Animal cells, by contrast, are usually well and constantly nourished, but still, they only grow and proliferate when new cells are needed. Nutrition supply thus is not the only crucial regulator [54, 55]. In a multicellular organism the fundamental processes of size regulation are controlled by intracellular programs and extracellular signals. The fundamental processes are cell growth, proliferation and apoptosis and the corresponding regulative factors can be distinguished by their functions into mitogens, growth factors and survival factors. Mitogens interfere with the cell-cycle and permit its progression, thus stimulating cell division; growth factors up regulate protein synthesis and other bio-synthetic processes, so that intracellular synthesis exceeds the degradation of proteins and thereby increasing the cell's mass; finally survival factors constantly inhibit a cells intracellular suicide program [22, 56]. The concentrations of these factors are crucial and limiting, because cells compete for these molecules in the sense that they take them up and then degenerate them. Increasing the concentration of these factors artificially also amplifies the respective behavior of the responding cells until the cells' saturation for this factor is reached [56].

The potential mechanisms in a multicellular organism to coordinate cell growth and division are multiple. Cell division could be controlled like in yeast by an intracellular cell size check-point, but there is evidence that such threshold control for cell size is not always used in multicellular organisms [57, 58].
Besides the control of proliferation by cell size, two more molecular principles are known. Firstly, cell growth and division can be controlled by separate extracellular factors to each of which cells respond independently. Then cell division and growth becomes a problem of the ratio between the factors. Secondly, an extracellular factor can have several functions and can boost cell growth and cell-cycle progression simultaneously [51, 58].
Interestingly, a rather small number of evolutionarily conserved regulatory genes, respectively their signaling pathways, are used repeatedly in the morphogenesis of many different organisms and for a wide variety of structures [25] without any direct discernible correspondence between homologous genes and morphological traits [59]. Therefore, it is in [26] argued that the phenotype of a gene is best described as context-dependent and individual cells do not only react to genetic signals, but also react as much to physical cues like the mechanical stresses of their environment [60]. Evidence for this argument comes from different experiments. Mammalian cell culture experiments using micro-fabricated structures to confine cells in simple geometries resulted in proliferation patterns that directly corresponded to regions of high tractional stress generated in the sheet. The stress distribution in the tissue was derived from finite-element simulations [61]. In early experiments epithelial cells have been grown on a substrate and stretched, sequentially showing a significant increase in cell proliferation rate [62]. In other experiments cultured cells were kept under static pressure, which decreased their growth and proliferation rates significantly [63]. In conclusion it can be said that the growth of cells and their multiplication by division generates mechanical stresses within a tissue, which then feeds back and influences the cellular behavior.
The regulation of growth of an organism can be distinguished into systemic regulation and autonomous regulation [56]. Transplantation experiments indicate, that many organs control their size and shape autonomously [56] like the imaginal wing disc does (see chapter 1.4). Such an organ grows until it reaches a set-point in size and then ceases its growth independently without receiving any further

[5] In later chapters, which are related to the wing imaginal disc and the control of its growth, we will refer to growth as cellular growth with subsequent cell division, if not stated otherwise (see also chapter 1.4.2).

systemic termination signal [56, 64]. These autonomously regulated organs must still receive some systemic information to adapt with the whole organisms development, which in turn is adapted to the organisms environment. For example, if nutrition is scarce, many organism develop into small adults that contain fewer and smaller cells than usual,[6] but their body proportion stays the same.
Thus the growth of some organisms can be seen as partly modularized and organs that have been demonstrated to develop autonomously are valuable model systems to study multicellular growth and growth control.
But what makes an organism or autonomously regulated organ determine its final size and what makes it stop growing after reaching its correct size? The size of an organism or an organ does not have to follow directly the size of its cells. In many cases total cell mass seems to be the control parameter instead of the total number of cells . Illustrating experiments were done in salamander, wherein cell size was increased tremendously by changing their ploidy [66].[7] Although the cells of the salamander of different ploidy differed about fivefold in size, their bodies and organs were of the same sizes compensating the effect of cell size by down-regulating cell number. Cell competition observed in the imaginal wing disc indicate similar results (chapter 1.4.2).
Different possible mechanisms for size regulation have been discussed and proposed. For example, cells could compete for a limited amount of extracellular factors and proliferate and grow until a steady state is reached between production and degeneration of extracellular signaling molecules. Cells also could constantly produce a growth inhibition factor that is accumulated over time and when a threshold is surpassed growth stops [68]. Feedback regulation of growth has long been known in mammalian liver. In experiments rat livers were artificially enlarged by continuously injecting the rats with a growth stimulating drug. After ceasing the treatment the organs shrunk back to their original size due to an increase of apoptosis [69]. Surgical experiments showed, that when up to two-thirds of a rats liver was removed, the liver would still fully regenerate by proliferative growth [70]. These results are mainly discussed in terms of the mentioned biochemical mechanisms.
In an epithelial system like the wing imaginal disc (chapter 1.4.2) evidence for a different mechanism of growth termination was found. Bryant and Schmidt describe two types of loss-of-function mutations [71]. One is causing a failure in gap-junction communication and causes hyperplasia, i.e. overgrowth due to an increase in cell number. The other leads to a neoplastic tissue, i.e. a tumorous overgrowing tissue that looses its structure and ability to differentiate. The mutated gene leading to the neoplastic growth encodes for cell adhesion molecules (e.g. cadherins). This suggests, that for the control of growth termination a different biomechanical mechanism could be used. More regulation models are presented in 1.5 based on the investigated model organ of the Drosophila wing disc.

[6] Sensing of nutrition is known to be connected to the evolutionary conserved TOR-regulatory network, which can be found in all eucaryotes. In animals an additional level of nutrition related control exists by the pathways of insulin and insulin-like growth factors, which control nutrition uptake and cell growth (for details refer to [54, 22, 65].)

[7] In all organism a cells size increases with its ploidy, i.e. the number of chromosome sets in the nucleus. A diploid cell is half the size of a tetraploid cell, i.e. a diploid cell only contains half the number of ribosomes and synthetic capacities. [67]

1.2 Development of Drosophila melanogaster

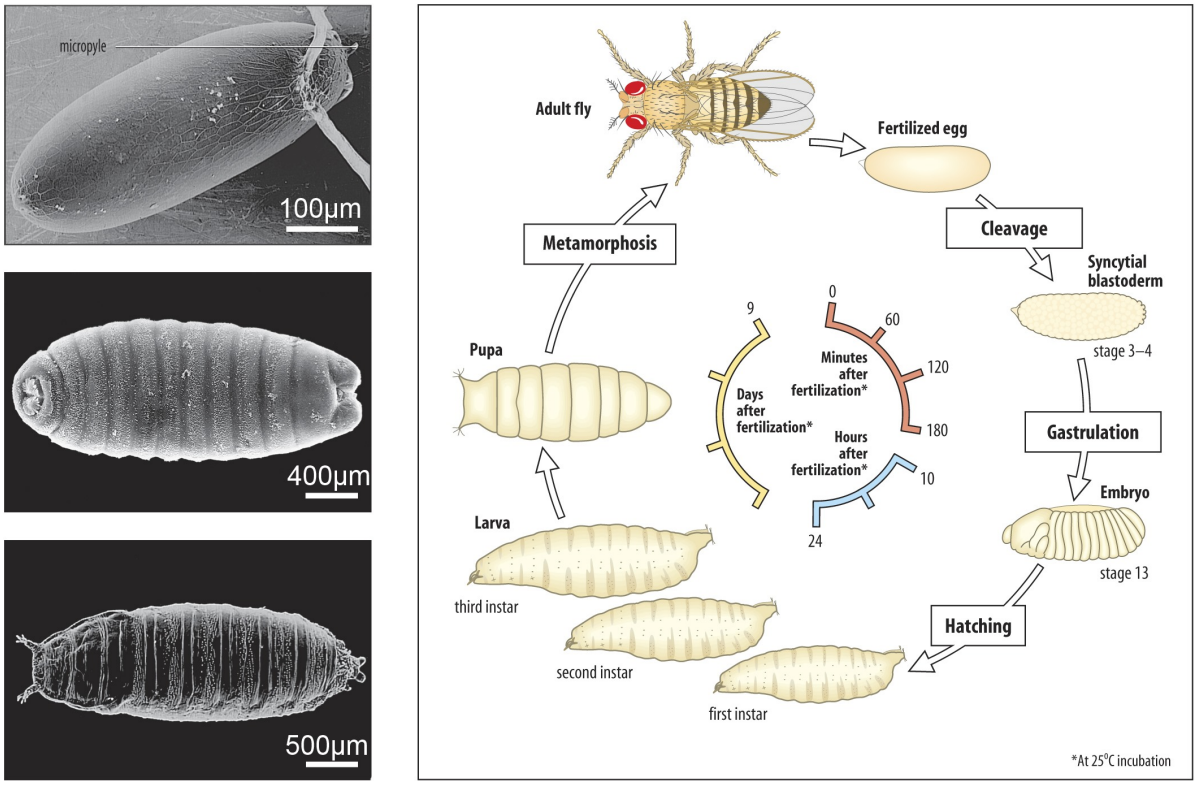

Figure 1.1 – After fertilisation through the micropyle the embryo undergoes cleavage within three hours, followed by gastrulation such that within one day a larva hatches. Then three so-called instar stages of the larval development follow which are divided by moults of the larva where it sheds cuticle, spiracle, mouth and hooks. The first moult occurs two days after the egg was layed, the second moult three and the third moult five days after egg laying. With the last moult at day five the third instar larva enters into pupariation. During pupariation the final metamorphosis to the adult fly or imago takes place which emerges between day eleven and thirteen. The given timing is for 25°C At 18°C development takes twice as long, but leads to an increase in body size [72, 73]. The electron micrographs showing an egg before fertilization (top), a second instar larva (middle) and a pupa (bottom) (adapted from [18]).

Drosophila melanogaster is one of the best understood organisms in genetics and developmental biology. It has a short generation time (about ten days at 25°C), high fecundity (a female lays about 100 eggs per day), is cheap to breed and easy to mutate. Due to decades of research the whole genome is known today and many genetic tools are available such as balancer chromosomes[8] or a high variety of genetic markers, be it the flie's phenotype or fluorescent proteins [72]. Most of Drosophila's genes and mechanisms that regulate development are similar to those in higher organisms and thus evolutionary conserved.[9] In contrast to higher organisms genetic redundancy is less prevalent in Drosophila, i.e. one gene more often codes for one function whereas in vertebrate several homologue genes code for the one and same function. This makes Drosophila such a valuable model organism. Mutations in the fly with its more economical set of genes more easily unveil the core function of the mutated gene, while the same mutation in a more complex organism would have no observable effect [22].
Drosophila is homometabolous and thus undergoes four developmental stages from egg, larva and pupa to the adult fly. Its body is divided into head, thorax and abdomen in which thorax and abdomen

[8] Balancer chromosomes consist of multiple chromosomal inversions that disrupt synapsis and thus make it possible to maintain fly stocks carrying homozygous lethal mutations [74].
[9] For instance, the proteins Amyloid Precursor Proteins (APP) is present in Drosophila and humans and is a key protein in treating Alzheimer [75].

can be further split into several segments. This pattern of segmentation already arises during early embryogenesis and becomes most obvious in the larval stages [22].

1.2.1 Embryogenesis of Drosophila

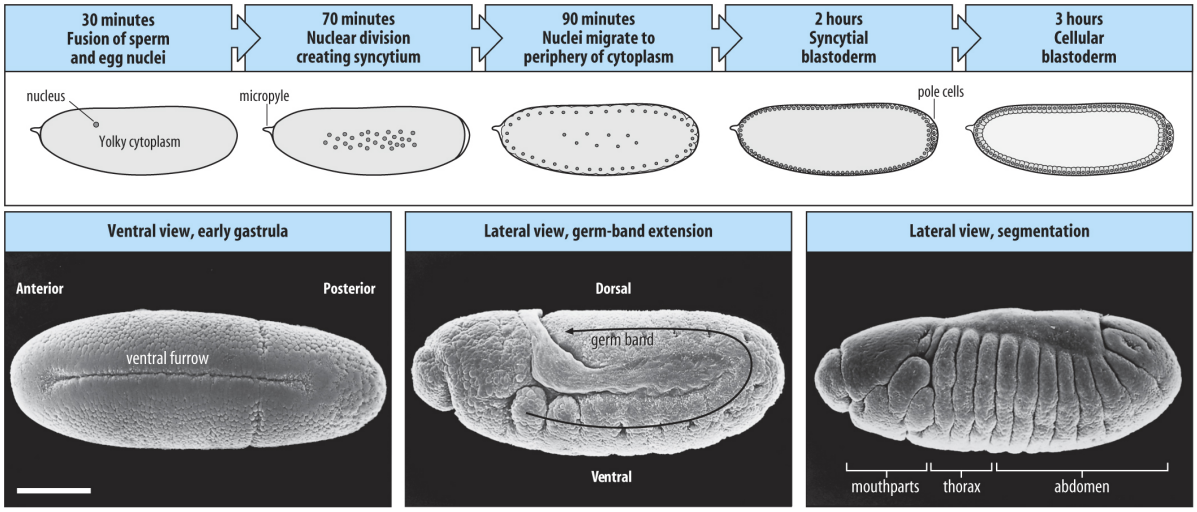

Figure 1.2 – The top row shows cleavage in Drosophila with its special stage of syncytical blastoderm. The bottom row pictures three different important morphological changes during gastrulation: At early gastrulation cells invaginate inside the embryo through the ventral furrow forming the first internal structures. Later on, the germ-band with its parasegments extends and drives the future tail on the dorsal side. Finally, the germ-band is retracted again and the embryo clearly segmented (from [23]).

Drosophila embryogenesis is one of the best investigated processes in developmental biology. During embryogenesis the body plan develops from a fertilized egg by genetic patterning and morphogenesis. After fusion of the sperm with the egg's nucleus, a series of rapid mitotic devisions starts, occurring about every nine minutes. After nine devisions the nuclei migrate to the surface forming a syncytial blastoderm. Plasma membranes start growing inwards from the surface to enclose the nuclei. After the thirteenth round of mitoses all nuclei are finally enclosed and the syncytial blastoderm becomes a cellular blastoderm.
Before the cellular blastoderm is finished, gastrulation starts and initiates many complex morphological changes. At the beginning a deep furrow forms on the ventral side when mesodermal cells migrate inwards. Pole cells, which are the precursor cells for the germ cells of the fly, migrate along the dorsal side from the posterior end (tail-side) towards the anterior side (head-side) and invaginate after half of the way. Meanwhile, a crest develops separating a region, which will later develop into the head, mouthparts and foregut. At this stage of germ-layer extension the future tail of the body elongates at the ventral side and finally folds upwards onto the dorsal side. Body segments then become defined. The first three segments on the anterior side will give head and mouthparts, the next three to the thorax and the remaining to the abdomen. Eventually, germ-layer retraction takes place, i.e. the rear end retracts back to the ventral side straightening out the embryo. This is followed by dorsal closure, the closing of the gap in the embryos epidermis on the dorsal side.

In the first three hours, during the formation of the egg as a syncytium, the egg can be understood as a colossal, single cell with multiple nuclei, thus all nuclei are directly exposed to gene regulatory proteins expressed in the common cytoplasm. At this stage positional information can be efficiently provided by

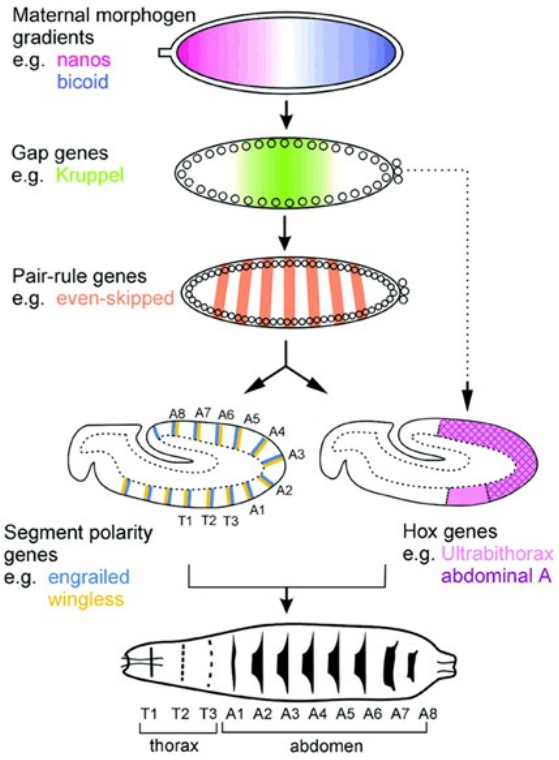

(a) Schematic overview of gene expression in embryogenesis (from [76]).

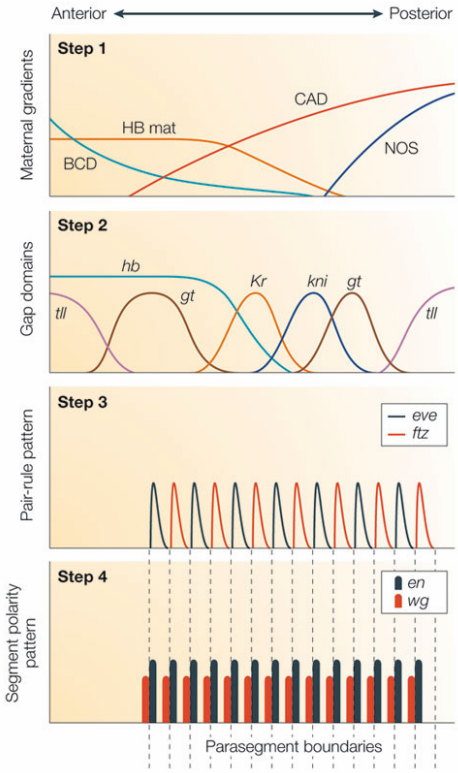

(b) The first transcription factor cascades leading to segmentation into parasegments (from [77]).

Figure 1.3 – The different stages of gene expression patterns during embryogenesis. Fig. (a) shows pattern formation along the A/P-axis in relation to the morphological stages of the embryo. Maternal morphogen gradients and the gap genes are active during cleavage and syncytial blastoderm, while the pair-rule genes, segment-polarity and hox genes act during different stages of gastrulation and on the cellular embryo. In Fig. (b) the focus is on the principle interaction of the same genes and how they relate to each other. In this figure the parasegment boundaries are illustrated, which are later on shifted by half a segment. For names and details please refer to [76, 22, 18, 65].

morphogen gradients [23, 65].
Already at oogenesis – the making of the egg – maternal mRNA is transfered into the oocyte, which is transcribed after successful fertilization. The transcribed maternal-effect genes or *egg-polarity genes* are the very first step in pattern formation. Their products establish the morphogen gradient bicoid, which provides global positional information and thereby defines the anterior and the posterior side.[10]. In a similar gradient-dependent manner the dorsal-ventral axis is established. Here the morphogen decapentaplegic (dpp) already appears, which is also very important for the development of the imaginal wing disc (see chapter 1.4.1) The egg-polarity genes are also responsible for the differentiation into somatic and pole cells and the transcription of the *segmentation genes* along the A/P-axis [22]. The segmentation genes subdivide into three groups and, named according to their mutant phenotype, can be thought of as being expressed chronologically with some overlap in their expression.
The first expressed zygotic-effect genes are about six *gap-genes* followed by a set of eight *pair-rule genes* and ten *segment-polarity genes*. While the gap-genes are expressed in particular regions of the embryo, but not periodically, pair-rule genes and segment-polarity genes evolve a pattern of periodic stripes along the anterior-posterior axis. Figure 1.3b illustrates in detail the interplay of the different gap-genes and how they interact to express the pair-rule genes. The interplay of different combinations and concentrations of the products of gap-genes and egg-polarity genes form single stripes or at least pairs of stripes, such that the non-periodic expression patterns of the gap-genes and egg-polarity genes give raise to periodic structures of pair-rule and then segment-polarity genes. This is possible due to multiple binding sites for different regulatory proteins in the non-coding regulatory region of the involved genes. Depending on the combination of proteins bound to the regulatory region of a gene, the gene is translated and finally expressed or not. This solution of regulatory modules in the non-coding DNA of a gene allows the generation of almost any pattern of gene expression and to alter one part of a pattern without affecting the rest of it and to reuse regulatory genes and proteins.
In each step of gene expression a more complex pattern evolves, finally defining fourteen parasegments of the embryo's body by progressively subdividing the embryo into a more and more refined pattern. As development proceeds through gastrulation and beyond, the products of egg-polarity, gap- and pair-rule genes disintegrate, but the segmental organization is maintained by the segment-polarity genes. Segment-polarity genes work at the cellular blastoderm stage and some of them are expressed at the compartment boundaries to delimit a cell-lineage boundary such that cells from one segment can not cross over to another. Up to this stage all segments are genetically equal and it is the activity of the *homeotic selector genes* that determine each segment's identity. They are divided into the Bithorax and Antennapedia complex and are also present in nearly all animals, including humans. The DNA of this Hox complex contains multiple binding-sites for all the products of egg-polarity, gap-, pair-rule and segment-polarity genes and interprets these multiple items of positional information. The order in which the homeotic selector genes are expressed along the embryo's axis corresponds closely to the sequence these genes are ordered along the chromosome. This suggests that these genes are activated sequentially by a graded process with the more posterior genes, which are activated later, overruling the earlier and more anterior genes.

[10] On the mechanism of morphogen formation refer to [78].

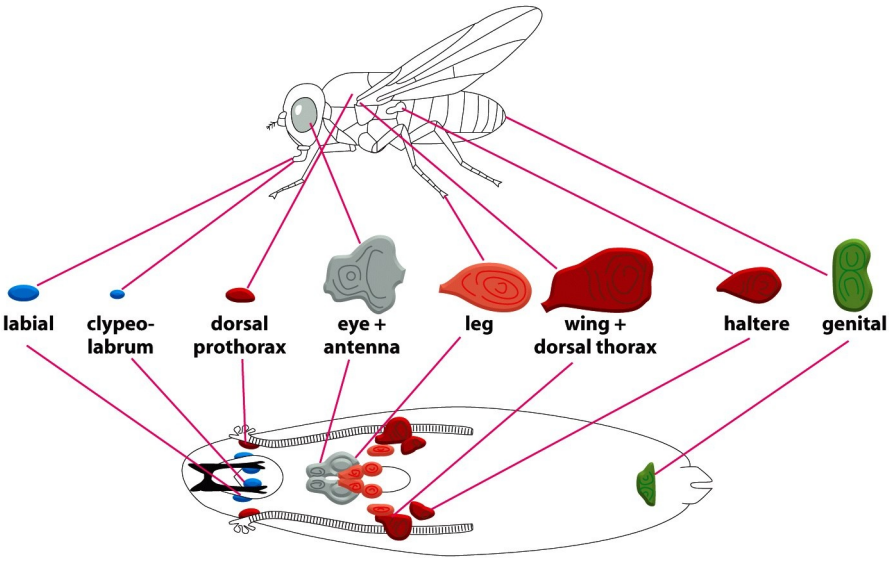

Figure 1.4 – Outline of somoe imaginal discs and the corresponding adult structures they give rise to. (from [22])

1.3 Organogenesis of Imaginal Discs

Drosophila's appendages and organs develop from discrete groups of precursor cells which are set apart during embryogenesis. During the subsequent larval stages these clusters of 20 to 30 cells grow about 1000-fold forming pouches of epithelial tissue called imaginal discs. The fruit fly's larva contains nineteen such discs, which all develop into a corresponding adult structure such as the eye, antenna, leg, haltere or wing during the pupal stage. Imaginal discs are formed by two contiguous epithelia, the disc proper which is a columnar layer and the peripodial membrane which is a squamous layer (see figure 1.6). Although the imaginal discs look rather similar, their fate is already determined according to the segments they developed from.
During the cellular blastoderm phase groups of cells at the parasegment boundary are determined to develop into the imaginal discs. Engrailed (En), Decapentaplegic (Dpp) and Wingless (Wg) mark out an orthogonal grid as shown in figure 1.5. The cells near by their intersection become determined to develop into imaginal discs [79]. One of the appendages mostly used as a model system in developmental biology is the wing imaginal disc. It has a simple structure and pattern and is most easy to work with due to being the largest of all the larva's precursor organs.

1.4 The Wing Imaginal Disc

Also starting from a cluster of 20 to 40 cells, the discs grow roughly exponentially at the beginning of disc development [4] and then continuously slows down its growth rate [81]. The decrease in growth rate can be described by an exponentially decaying growth rate [81] until growth ceases at the end of the late third instar and the beginning of metamorphosis. The wing imaginal disc then roughly consists of roughly 30000 cells [5]. During final metamorphosis the cells of the imaginal wing disc undergo one additional round of cell division and form the wing by eversion of the wing pouch along the dorsal-ventral boundary (seen in figure 1.6). Thus the wing's final size is predetermined by the final size of the imaginal wing disc at the end of the third instar [6]. Many developmental questions concerning growth and size control, pattern formation, scaling, self-organization and others are addressed in the

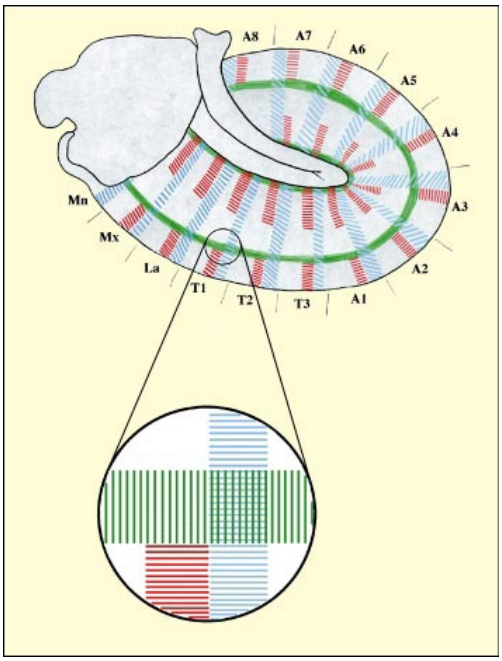

Figure 1.5 – Gene expression patterns of Engrailed (blue), Wingless (red) and Dpp (green) to determine the cells location and cells of the imaginal discs. The circled region of the thorax T1 is the location where the first leg primordium is formed nearby. Right next to it in the T2 segment the imaginal wing disc develops. The picture shows the stage of germ-band-extension with the future tail folded upwards to the dorsal side [from [80]].

imaginal wing disc. It is an experimental system that intrinsically and autonomously regulates its size as transplatation experiments [82, 4] have shown. In [4] for instance, wild-type[11] discs were transplanted into the abdomen of females and kept there for up to 28 days. Although the transplanted discs were kept in this culture and nutrition environment for such a long time, they did not overgrow and ceased to grow at normal size. Of course systemic factors like nutrition play an important role in growth and development of the whole larva [83]. An advantage of the imaginal disc is that it is a two-dimensional epithelial sheet, which reduces the analysis to two dimensions.

1.4.1 Patterning and Morphogenesis

Pattern formation and morphogenesis are driven by long-range morphogenetic factors like Decapentaplegic (Dpp) or Wingless (Wg). The formation of a pattern in the wing imaginal disc already begins during the segmentation process in the embryo. Local cell-cell interactions establish a transient expression of the selector gene *engrailed* via autocatalysis (see figure 1.5 and chapter 1.1.2). The expression domain of *engrailed* defines the posterior territory while the remaining cells not ruled by *engrailed* become anterior cells. During this initial and transient phase the gene expression boundary is not a lineage-restricting boundary and cells still may cross the border and adapt their behavior to their new environment. This changes when the expression of *engrailed* becomes heritable and the constant input from higher-order signaling becomes obsolete. This ensures a stable and permanent expression of the selector gene and unties patterning of the wing disc from the embryonic patterning machine. However it also makes it necessary to have a mechanism allowing for to avoid of the intermingling between different compartments [85]. An important role in A/P compartmentalization and further patterning is played by the short range signal hedgehog (hh), which is synthesized in posterior cells. Simultaneously, posterior cells are made insensitive to the effect of hedgehog by engrailed [86]. Hedgehog diffuses on a short scale into the anterior compartment. On the one hand, this is important for the mechanical segregation

[11] The term "wild-type" is rather ambiguously used for flies unchanged in the investigated genes of interest.

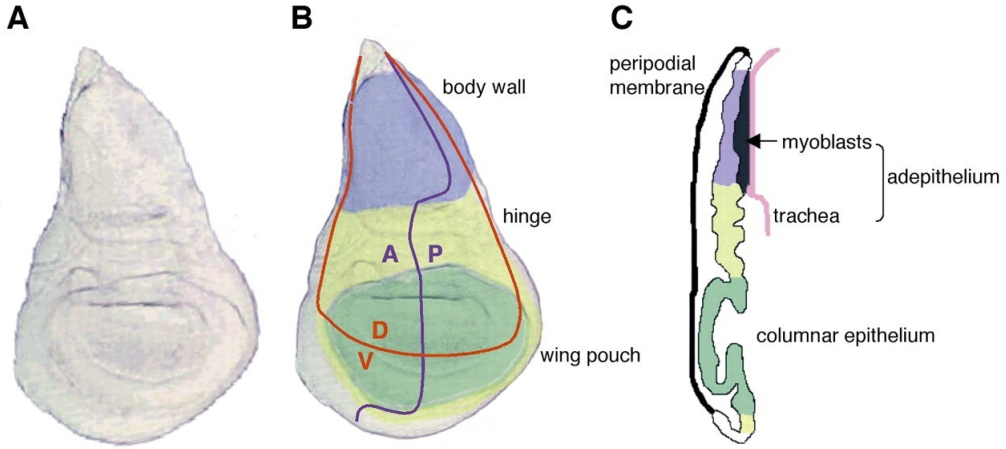

Figure 1.6 – Wing disc fate map from [84]. **A:** Dissected late third instar wing imaginal disc. **B:** Fate map of the wing disc from the top, showing the anterior-posterior (AP) and dorsal-ventral (DV) compartment boundaries. The different regions give rise to different structures in the adult: The blue region evolves into a part of the thorax (the mesonotum), the yellow region gives rise to the hinge that connects mesonotum and the wing blade, which develops from the wing pouch (green). **C:** Side view of a wing disc showing the columnar epithelium and the squamous epithelium or peripodial membrane. The small adepithelium consisting of myoblasts and tracheal cells will develop into the flies wing muscle and airtubes.

of anterior cells from posterior cells and thus the erection of the A/P-boundary [87, 88, 89]. On the other hand, this initiates a small stripe of anterior cells adjacent to the A/P-boundary to express the long-range morphogen-gradient Decapentaplegic (Dpp) [86].
Dpp then acts directly on every cell [90, 91] binding to specific cell receptors. Dpp represses the intracellular transcription inhibitor brinker, which in turn is the default repressor of dpp target genes [92, 7]. Thus an intracellular reciprocal concentration gradient of brinker is established [93]. More information about the dpp and its molecular pathway can be found in the reviews [7, 94].
It is agreed upon, that dpp spreads non-directionally, is degraded while spreading and thus establishes an exponential gradient in space. How the dpp gradient is established is a topic discussed with controversy [95]. In 2002 Lander et al. [96] proposed dpp gradient diffusion via restricted extracellular diffusion, whereas others strongly argue for receptor-mediated transcytosis (repeated uptake and release of the molecule) as a transport mechanism, either due to FRAP-measurements[12] of kinetic factors [97], or modeling of gradient formation with robustness as a performance objective [98]. These findings were challenged by loss-of-function and gain-of-function mutations for dpp receptors [71] and a collection of fluorescent measurements [99] strongly argue for diffusion. Reviews on dpp and morphogen formation can be found in [100, 101].

Lawrence and Struhl [102, 103] referred to this form of pattern formation as the ”central dogma” of epigenesis and summerized it as follows:

1. Define a subset of cells with different fates by a (transient) morphogen gradient.
2. Establish compartments and linear boundaries as spatial reference points by short-range signaling.
3. Raise a long-range morphogen gradient outgoing from the reference points.

During the second larval instar the dorsal-ventral boundary starts to form by the expression of *apterous* in dorsal cells [104, 105]. The dorsal-ventral compartment boundary is established and a complex inter-

[12]FRAP: Fluorescence recovery after photobleaching.

play of selector gene and short range signals [105] drives the cells along both sides of the boundary to establish the morphogen gradient of wingless (Wg) [106, 107]. A review about wingless signaling and its role in patterning can be found in [108]. The wing imaginal disc is subdivided into four compartments [103].
Genetic mosaic experiments in Drosophila first revealed that cells of different compartments do not intermingle [109]. In these experiments single somatic cells are mutated at a later stage in development and thereby an organism of multiple genotype is created. This is commonly achieved by an induced recombination between maternal and paternal chromosomes in flies heterozygous for the genes of interest in the crossed-over chromosomal region. For instance, the induction of recombination can be done by a heat-shock ($\sim 35°C$) at the desired moment of development. If the heat-shock is correctly adjusted the recombination will occur only in one or a few cells scattered at random and the organism then consists of cells with different genotypes and thus becomes a genetic mosaic. The occurrence of recombination is visualized by a marker lying on the same chromosome arm as the genes of interest [22]. Following marked single cells and their descendants ('clones'[13]) revealed the compartmentalization of the wing imaginal disc. Compartment boundaries are not connected to any morphological trait, but can be inferred from the shape of a clone when it grows at a compartments edge. Then the clone forms a straight line [109, 85, 103] while clones within a compartment grow as wiggly, but contiguous and coherent patches [85] as cell contacts are not remodeled during mitosis and daughter cells remain in contact [110] (please refer to chapter 1.5.5).
Proliferation within a tissue can change cell position and cellular topology, which could compromise and deform a linear boundary. Therefore position and integrity of the boundaries has to be specifically maintained. In particular along the compartment boundaries in the wing disc an increased cell bond tension is observed, which is generated by contractile elements like actomyosin filaments at the cell cortex [111, 112]. This increased cell bond tension is used in [113, 114] to explain the segregation mechanism along the A/P boundary in detail.

When the D/V boundary is established during the second instar not only the morphogen wingless is expressed, but also *vestigial*, which is another important selector gene specifying the wing primordium and defining the nascent proximal and distal axes. Starting from a stripe of vestigial expressing boundary cells, cells with a high level of vestigial entrained neighbor cells to upregulate vestigial. Vestigial is thus iteratively upregulated from neighbor cell to neigbhor cell and in addition mediated by a quadrant enhancer [115], which in turn is under the control of wingless [116] and Dpp [116, 115, 117].
Thus three coordinate systems sequentially arise during the development of the wing imaginal disc. The intersection of the A/P and D/V boundary pins down the position of later wing blade and directs the last step of patterning into proximal and distal regions.

A phenomena in wing imaginal disc pattern formation is the adaption of pattern to size. Starving Drosophila larvae will stop growing and directly initiate metamorphosis as soon as they have reached their necessary critical weight,[14] resulting in tiny adults but with normal proportions [118]. In the wing the scaling of pattern to size can be quantified by the relative position of the wing veins relative to the overall wing size. For instance, vein two is known to be directly controlled by the expression of Dpp target genes [119] and adapts its relative position and proportion to the total size of the wing [120, 121]. Direct studies [122, 123, 124] have shown that the activity of the Dpp gradient adapts to tissue size during growth. Different mechanisms of scaling are proposed [123, 125], but they all are based on a decrease of dpp degradation (reviewed in [94]).

[13] Generally, a clone can be defined as the group of all descendants of a founder cell from a specific stage of development.
[14] The critical weight is a developmental threshold. After surpassing the critical weight a larva will continue its development even if it encounters starvation. In contrast, the minimal viable weight reflects the amount of energy storage a larva needs to survive metamorphosis. In Drosophila critical weight and minimal viable weight are reached at the same time. [83]

1.4.2 Growth and Size Control

Cells in the wing imaginal disc proliferate at roughly the same rates irrespective of their spatial position in the tissue. Growth can be described as uniformly distributed [8, 9, 10], while the growth rates decrease over time [126, 123]. The tissue's growth is thus more or less homogeneous and the tissue's proportions scale [3, 94]. In [3] Schwank and Basler discuss that homogeneous growth is not a prerequisite for scaling, but they argue that homogeneous growth could increase precision and robustness of pattern formation as it provides more flexibility in time for patterning events.
These flexibility in time is not purely hypothetical and actual needed sometimes. For instance, a delay in development can be seen in cell competition experiments. In these experiments some cells become weakened by a mutation like *Minute* [127]. *Minute* slows down the cellular protein production and thus its overall growth. Cells growing at normal speed will compete with these *Minute* cells for space and remove them by the induction of apoptosis as if the wings area is already predefined [6, 128]. However, if the weak and strong populations are separated by a compartment boundary, both populations survive. In the circumstance that the larva consists of weak cells and a few strong cells, the compartments of strong cells fill up and wait for the compartment consisting of weak cells to reach its full size. This illustrates that size seems to be a predefined and important objective and that growth is controlled by patterning in a not necessarily time dependent manner [6].
To test size regulation of the wing imaginal disc, the cell-cycle progression was experimentally changed and either accelerated or decelerated repsectively blocked. Cells that were hindered in cell-cyle progression overgrew, while accelerated cells were in average much smaller in size than unperturbed cells. The result in size difference was up to four to fivefold, but the disc compensated for these changes in cell size by adapting the total cell number [129, 130]. The size of the wing is thus not a function of cell number and for the cessation of growth the disc must find a way to measure its dimensions.
First evidence for a connection between pattern formation and growth came from regeneration. Classic experiments are the surgical grafting of cockroach legs, in which the missing parts of the legs were filled in from juxtaposed fragments [131], i.e. the pattern reestablished by means of growth. In [132, 133] wing discs also showed regeneration when they were systematically cut into pieces and then cultured in larvae.
Molecular experiments have shown that morphogenes like Dpp or Wg are not only patterning agents, but also growth factors. Flies lacking either one of these fail to develop wings [134, 135, 136] and clones unable to transduce Dpp or Wg are sorted out from the wing field [137, 138]. Ectopic expression in the case of Dpp leads to overgrowth in the lateral domains of the disc and massively enlarged discs [90, 91, 139, 135], which is the reason Dpp is seen as a paradigm of a morphogen and growth promoter. Although it became clear that dpp is necessary for growth, the link between dpp distribution in a spatial exponential gradient and uniform growth is not obvious.
Today virtually all known morphogens are growth regulators and most of these are growth promoters [140, 7, 108].

1.5 Growth Models

To model tissue growth two main questions have to be answered:

- Why are growth rates in the imaginal disc uniform in spite of the fact that the promoting growth factors form spatial gradients?
- What makes a tissue measure its size and stop growing?

Different growth models for the wing imaginal disc were proposed. They can be classified either by the problem they address, their complexity or the function of the morphogen gradient. All models address the question of homogeneous growth, but only some of them also propose a mechanism to explain the cessation of growth. Models differ in their complexity in the sense that some models integrate

complementary growth regulators to explain growth while others try to explain growth only by the morphogen's properties. The classification by complexity is a similar approach like the classification by morphogen function. In some models the morphogen has a "permissive" function, i.e. it promotes growth over a certain concentration threshold, while in other models it has an "instructive" function similiar to its function as a patterning agent and promotes growth proportional to several concentration thresholds.
We will start with models addressing the question of homogeneous growth and then discuss models that explain size measurement and growth cessation.

1.5.1 Memory, Threshold and Inhibitor Model

The memory model proposes a sensitizing effect of Dpp. Cells that arise early in development and thus are exposed to the morphogen longer are sequentially trained to respond with a mitogenic activity on lower levels of dpp. As a consequence lateral cells become more sensitive than medial cells and compensate for the morphogen gradient. This model predicts homogeneous growth if Dpp is ubiquitously secreted from the beginning of development. However, these kind of experiments result in an increase of growth in the lateral regions and leads to overgrowth along the D/V boundary of the disc [91, 141, 139].
According to the threshold model growth is switched on as soon as cells experience even a marginal concentration of Dpp. Again ubiquitous expression of dpp can not be explained by this model.
The inhibitor model is based on the assumption that parallel to the Dpp gradient a gradient of an inhibitor is formed, such that the net effect of growth promotion is uniform in space [80, 142]. Under the assumption that both growth promoter and inhibitor are produced at different rates converging over time, the termination of growth can be explained. If the inhibitor is under the control of Dpp, homogeneous expression of Dpp should result in spatially homogeneous growth rates. This leaves the possibility of an independent inhibitor. However, up to now such a system has not been identified, making this model highly speculative [3].

1.5.2 The Opposing Growth Pathways Model

This model is based on experiments of Schwank et al. [9, 143]. Their work showed, that Dpp promotes growth the way it patterns the disc: Dpp represses brinker (brk). In discs in which Dpp and brk (or only brk) were switched off they observed non-uniform growth due to an increase in growth rates in the lateral regions and a decrease in medial regions [9]. The authors interpreted their results as evidence for a permissive role of Dpp, meaning that the gradient is irrelevant for growth. To explain the different growth rates an additional Dpp-independent growth input was proposed that complements the growth repressing effect of brk. In [143] they present their "opposing growth pathways" model with fat as brk complementing growth repressor of brk. Before fat was identified as an additional growth factor, it was speculated if mechanical feedback could be this regulating mechanism [3] (refer to chapter 1.5.5).

1.5.3 The Spatial Gradient Model

In spatial gradient models cells do not measure the absolute level of dpp, which are exposed to, but neighboring cells measure difference in concentration levels, that is the slope of the gradient. If the slope of the dpp gradient is sufficiently steep cells will proliferate. One of the first proposed models came from Day and Lawrence [6], who assumed a linear gradient, which is fixed at the center of the disc and its edge and stretches as the tissue grows. If the size of the tissue reaches a certain size the slope of the gradient becomes too shallow and proliferation terminates. First support for this model came from cockroach regeneration [131]. However this model fails in explaining wing imaginal disc overgrowth, when Dpp is ubiquitously expressed.
A modified spatial gradient model was presented in 2005 by Rogulja et al. [139]. They assumed that lateral cells became programmed differently during early wing imaginal disc development, such that

they will react to both – the slope of the Dpp gradient and its absolute level. In contrast, medial cells still only react to the slope of the gradient. The presented experimental evidence for their gradient model was based on transient cell proliferation, which they observed at the boundaries of constitutively active Thick-vein clones (Tkv^{QD}).[15] This corresponds to a local increase of the slope and corresponding to this model should result in a local promotion of cell proliferation. Furthermore, they ubiquitously expressed Dpp in the wing imaginal disc and found an increase laterally in cell proliferation and a medial suppression of cell proliferation. Corresponding to their model the slope in the medial region was too shallow to trigger cell proliferation, but in the lateral region's cells could respond to the absolute level of Dpp and enter mitosis.
The experiments of Schwank et al. [9] refute this model as they produce the same results of ubiquitous Dpp expression in double mutant discs for Dpp and brk.

1.5.4 The Temporal Gradient Model

The temporal gradient model was lately proposed by Wartlick et al. [123] and assumes that temporal rather than spatial differences in concentration are the crucial signal for proliferation. The model is based on the authors observations that Dpp activity scales with tissue size and that cell signaling is increased by the same percentage as the gradient lengthens [94]. If a cell measures a relative increase of α in Dpp signaling since the beginning of its cell-cycle, then it will divide. Due to the relative increase in signal the model can account for uniform growth and termination of growth. When the relative increase in Dpp activity slows down the cell cycles will lengthen. At some point cell cycle duration will be excessively long and will stop proliferation de facto. For the wing imaginal disc Wartlick et al. determined this relative marginal value to $\alpha = 0.5$ [123].
Hamaratoglu et al. also investigated the scaling mechanism of Dpp in the wing imaginal disc and tested this model with their data. In [122] they could only partly confirm Wartlick et al. results. While they also found the spatial Dpp gradient to scale with tissue size, Hamaratoglu et al. disagree with the main assumption of Wartlick et al. that an overall relative increase in Dpp signaling occurs. Furthermore, this model offers no explanation for the increased growth in wing imaginal disc where brk and Dpp were removed [9], leaving this model at least incomplete and highly controversial.

1.5.5 Mechanical Feedback Models

A different approach to explain uniform growth and size determination comes from models integrating mechanics of the tissue as a regulating parameter. In these models growth is affected by the mechanical stress between the cells of the wing imaginal disc.
The regulating effect of mechanical forces for the wing imaginal disc was first proposed by Shraiman who presented a model to explain uniform growth and cell competition [11]. This model treats the wing imaginal disc as a two-dimensional sheet, which is described in a continuum approach. This approach seems reasonable, because the wing imaginal disc consists of cells that are joined together near their apical side by adheren junctions (see chapter 1.1.1) and thus build an tissue-wide elastic network. Furthermore, global and massive cell movement and rearrangements including permanent remodeling of adheren junction were not observed in the wing imaginal disc besides local rearrangements due to cell division [110].
Shraiman describes the displacement of cells in a continuum mechanics, assuming that tissue's length-scales are large compared to cell size. He derives an expression relating the local change in pressure p that a cell experience to its local growth rate γ:

$$\frac{\mathrm{d}p(\mathbf{r},t)}{\mathrm{d}t} = \frac{\mu K}{K+\mu}[\gamma(\mathbf{r},t) - \langle\gamma(t)\rangle] - \frac{1}{\tau}p(\mathbf{r},t), \tag{1.1}$$

[15] Punt and Thick-vein (Tkv) are the cell-membrane receptors Dpp binds to. Tkv^{QD} is a constantly active form of Tkv and keeps the pathway permanent active.

K is the bulk modulus and μ the shear rigidity. According to this model non-uniform growth, that is the difference between the average growth rate of the tissue $\langle\gamma(t)\rangle$ and the local growth rate of a patch of cells $\gamma(\mathbf{r}, t)$, results in a local increase of pressure. The last term of equation 1.1 considers slow rearrangement and thus a relaxation of the tissue that is limiting the effect of non-uniform growth on the time scale of τ. The pressure a patch of tissue is exposed to equals the time integral of equation 1.1. To balance the differences in growth rates Shraiman proposes that the pressure cells are exposed to feeds back on them by decreasing their growth rate, i.e. $\gamma = \gamma(\mathbf{r}, t, p((r), t))$. The possibility of negative growth rates is explicitly taken into account, which effectively means that cells are removed by high pressure induced apoptosis.
Thus cells with higher growth rates than their environment are consequently tuned in to the average growth rate by the extra pressure that is acting on them. This high pressure is proposed to decline on a spatial length scale w, which is assumed to be comparable with the size of a cell. As a consequence cells with a lower growth rate adjacent to fast proliferating cells can be exposed to such high levels of pressure that these are removed. Therefore this model provides an explanation for the mechanism of cell competition [6, 127, 128] and uniform growth. Based on Shraimans model two models have been proposed for final size determination in the wing imaginal disc.

One was proposed by Hufnagel et. al [12] and is founded on a non-scaling Dpp gradient. In this "mechanical compression model" the size of the disc is given by the distance, at which the morphogen concentration falls below a threshold that is necessary to promote cell proliferation. Peripheral cells will stop growing when crossing this threshold. The more cells cross the border to the non-proliferating periphery the more increases the compression on the central regions. When compression is high enough, its inhibiting function fully counteracts the growth promotion of the morphogen. In this model the rate of morphogen secretion at the source and the decay length of the gradient terminates the disc's size. In [12] Hufnagel et al. present data supporting their assumption of a non-scaling Dpp gradient, although in an earlier work two of the authors presented evidence for the adaption of the Dpp-gradient to a change in posterior compartment size, altered by Insulin signaling [95]. Besides further recent support for scaling of the Dpp gradient [122, 123] it is left unclear how the threshold concentration of the morphogen is determined by the cells when absolute concentration levels are low and the gradient is shallow.

Other models on mechanical growth control that are able to explain final size control and uniform growth were proposed by Aegerter-Wilmsen et al. The basic concepts of these models were already incooperated in their first work [13], in which they assume that compression has an inhibiting function on growth, while stretching above a certain threshold promotes growth. Similar to the model of Hufnagel et al. growth is initialized by high levels of morphogen concentrations, which are assumed to be highest in the central area of the wing imaginal disc due to the intersection of Dpp and a further growth factor expressed along the D/V boundary. This leads to a high rate of growth for central cells, which will push neighbor cells, proliferating and growing at lower rates, to the periphery. As a consequence these displaced cells become stretched tangentially and in turn compress the central area of the wing imaginal disc. When a stretching threshold is surpassed the cells eventually divide, such that mitosis also occurs in lateral areas where no molecular growth factor is present. Under the condition that stretch induced cell division will not fully compensate for the internal stress, pressure acting on the central region continuously builds up as the wing imaginal disc becomes larger. Growth in the center terminates when the effects of compression and morphogens are balanced. This also stops growth in peripheral regions as they are not further stretched.
Besides homogeneous growth and its termination the model is able to explain overgrowth due to ubiquitous expressed Dpp qualitatively. When Dpp is uniformly distributed the highest growth factor concentration is along the D/V boundary and not solely in the center of the disc [141]. Growth is then mainly promoted by growth factors along the entire D/V boundary. This additional growth results in stretching of regions peripheral to the boundary. This stretch pulls the cells along the D/V boundary towards the center of the disc, creating compression in the medial area and resulting in lower growth rates in the medial regions of the disc.

Aegerter-Wilmsen et al. simulated the pouch of the wing imaginal disc as a radial symmetric flat area subdivided into several concentric rings [13]. Growth was equated with an increase in area, which is calculated separately for each of the rings considering growth by growth factors, stretching or compression.
To study the possible influence of mechanical growth regulation on epithelial topology Aegerter-Wilmsen et al. [14] evolved their simulations based on a vertex model, similar to the model presented by Farhadifar et al. in [45]. In this approach single cells are considered and described as polygons that are defined by their edges, i.e. their vertex positions and the apical shape of a cell is a result of mechanical force balance. Farhardifar et al. determined the force balance by local minimization of an energy function, which considered cell elasticity, line tension along the individual cell junctions and cell contractility for each cell. They studied epithelial packing considering uniform growth, cell division at random, apoptosis and cell rearrangements in their simulations and compared them to experimentally observed polygon distributions.[16] Aegerter-Wilmsen et al. adapted their model and compared the polygon numbers of different scenarios with experimental data. The first two scenarios were similar to those of Farhardifar et al. either considering uniform growth or uniform growth combined with cell rearrangements. The second two scenarios integrate a dependency of growth rate on the apical deformation of the cell and either consider rearrangements of cells or not. Coming directly from the model design this dependency on apical deformation effectively equates to a dependency on local stress a cell is exposed to. While Farhardifar et al. consider the polygon distribution of all cells, Aegerter-Wilmsen et al. in addition consider the polygon distribution of mitotic cells. Both authors succeeded to reproduce the polygon number distribution for all cells, when assuming uniform growth and cell rearrangement. However, Aegerter-Wilmsen et al. showed that reproducing the polygon distribution for all cells and mitotic cells is not possible using this scenario, but by using a scenario that integrates the mechanical control of growth [14]. These results indirectly argue in favor for a role of mechanical forces in growth control.
The latest model for mechanical growth control of the wing imaginal disc is also presented by Aegerter-Wilmsen et al.. It includes a regulatory network of experimentally confirmed molecular interaction and hypothetical effects of mechanical forces on this network [15]. The simulations of the wing pouch consists of two parts, which are interacting with each other. The first part calculates the growth rate for each cell depending on the concentration of active proteins, the second part calculates a cell's apical shape based on the vertex model. This model explicitly integrates the Dpp gradient with the principles of the Vg feed-forward mechanism [117, 144]. The main assumption of growth termination by compression remains, although it becomes refined such that growth terminates when compression in the center of the disc is above a threshold and the slope of compression from center to the edge of the wing pouch is below a certain threshold. This model is able to reproduce most of the key experiments and observations like uniform growth in wild-type wing imaginal discs [8, 143], a decrease of cell division frequency during the course of disc development [4, 81], growth of clones along the proximal distal axis [145, 146] and overgrowth of lateral regions of the disc due to uniform expressed Dpp [9, 139].
The regulation of growth by mechanical forces is an attractive model to explain growth and autonomous growth termination. A main assumption the model makes, is the increase of compression in the center of the pouch during the course of development. Experimental support comes from Nienhaus et al. [16], who investigates the wing imaginal disc, taking advantage of its photo-elastic property. Their measurements showed an increase in birefringence in the middle of the pouch, which for a photo-elastic material like the wing imaginal disc can be interpreted as an increase in mechanical stress. This is in accordance to the mechanical growth model. Furthermore, Nienhaus et al. cut the wing imaginal disc from the middle of the pouch to the outside and observed a decrease of birefringence in the pouch, which is pointing to a release in stress. Support for compressional stress in the pouch of the wing imaginal disc also comes from Ishihara et al. [17]. They developed a framework based on Bayesian statistics to estimate the pressure on each cell and the tension at each cell contact from the geometry of cells and confirmed their approach with artificially generated data. Using the images of apical cell shapes of

[16] The polygon distributions complies with the number of neighbors a cell has.

the wing imaginal disc they determined the local forces at each vertex of the cell. Consequently they showed a negative correlation of apical cell area with the compression of the cell and find cells with small apical cell area mainly distributed in the central region of the wing pouch.
However, the main assumption of a regulating effect on growth rate, i.e. proliferation rate, is still hypothetical. Does tensional stress promote growth and does compressional stress inhibit growth? I address this question in my thesis. To test the fundamental assumptions of the growth model the wing imaginal disc was stretched in vitro, while simultaneously determining the tissue's mechanical responses and proliferation rates.

2 Experimental Setup and Methods

2.1 Experimental Setup

Requirements. To investigate the responses of the wing imaginal disc upon mechanical stress and determine its mechanical properties a setup was needed that complies with different requirements.

1. Forces should be exerted on the tissue in a quantitative and reproducible manner.
2. The mechanical responses of the wing imaginal discs had to be monitored.
3. The method should be non-invasive for the wing imaginal disc such that it should not be cut, clamped, stabbed or harmed in any other way.

Based on typical values of Young's moduli for biological tissues, which range from a fraction of a kPa to several hundred of kPa I estimated that the setup should be able to exert forces in the range of several hundred µN to several mN.

Setup overview. To cope with these requirements a uni-axial pulling setup was designed and custom built with the versatility to be installed on inverted microscopes. The setup is sketched in figure 2.1 and consists of a cantilever beam of total length L and a stiff arm perpendicular to the cantilever beam at length $x = w$, which was used to deflect the beam. The support of the cantilever beam at $x = 0$ is installed on a linear three-axis positioner with a resolution of $\sim$5 µm [147] to provide the necessary flexibility when preparing for an experiment (see also 2.1.3). The deflection $z = d$ at point $x = w$ is adjusted either using a linear piezo-driven positioner with a resolution of $\sim$50 nm [148] or a high-accuracy micropositioning stage with a resolution of $\sim$100 nm [149], onto which the arm is mounted. A slice of cover slip glass (#0 slides with a thickness $\sim$ 80 µm) is fixed at the end of the cantilever beam. By means of an attachment factor the wing imaginal disc is attached with its basal-dorsal end to the glass slice and with its basal-ventral end to the microscope slide.
Depending on the experiment, modified respectively unmodified microscope slides were used (see section 3 and 4).

Setup variations. For experiments focusing on the mechanical properties of the wing imaginal disc microscope slides were used with an additional cover slip glued to it (figure 2.1, side-view, A). The purpose of this additional slide was to compensate for the height of the moveable glass slice, such that a stretching of the tissue could be done in plane. However, experiments focusing on the relation between applied stress and cell proliferation, i.e. monitoring cells' outlines, were done having the wing imaginal discs directly attached to the microscope slide (figure 2.1, side-view, B) and thus were pulled under a slight inclination. The reason for this distinction lies in the different types of microscope objectives used for the different types of experiments. While experiments that investigated the mechanical properties were done using $10X$ and $20X$ objectives with working distances between 4.0 mm to 0.4 mm, the experiments to monitor cell outlines and cell proliferation were done using a $40X$ oil-immersion objectives with a working distance of 0.17 mm, which equals the thickness of the used microscope slide (#1 slides). Thus, the working distance of the $40X$ objective did not allow to use setup variation A. Efforts to circumvent this restriction were made using #0 microcope slides, but these were found too elastic to be used as sample carrier as they followed the movement of the immersion objective when focusing (see

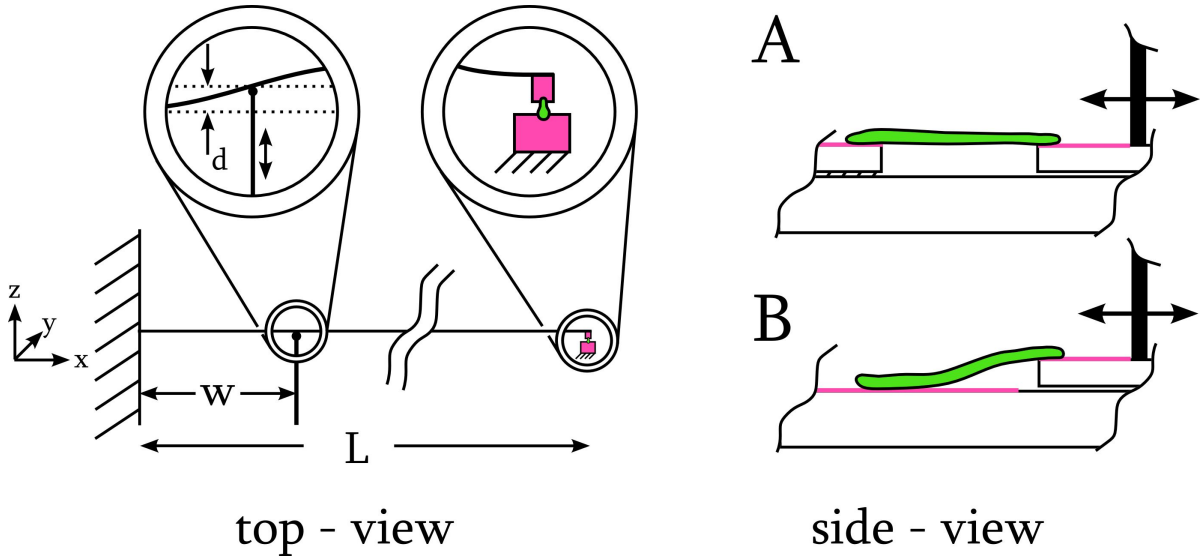

Figure 2.1 – **Top-view:** Non-proportional schematic of the uni-axial pulling setup realized via a cantilever beam. The point of deflection of the beam and the point where the wing imaginal disc is pulled are magnified. The support of the beam at length $x = 0$ is adjustable in three directions. At length $x = w$ the perpendicular arm deflects the cantilever beam about the distance $z = d$ from its neutral position. At length $x = L$ the wing imaginal disc (green) is attached at two points and slightly stretched due to the deflection of the cantilever beam. The Poly-L-Lysin coating is shown in violet. **Side-view:** Two proportional schematics of the setup variations used to stretch the wing imaginal disc.

section 3 and 4).

Attachment factor. The used attachment factor was Poly-L-Lysine, which is a synthetic amino acid widely used as a coating to enhance cell attachment and cell adhesion to plastic and glass hardware [150]. Due to its positive charge it enhances electrostatic interaction between negatively charged ions of the cell membrane and the surface it was adsorbed to [151, 152]. There are many different coating protocols giving detailed instructions on how to prepare the surface with Poly-L-Lysine [151]. Several protocols were tested and in conclusion it can be said that most of the proposed steps were unnecessary for my purposes, though there are some critical parameters for coating and preparing the surfaces. For instance, the surfaces should be free of any organical remainings, which only was an issue when reusing the equipment. Reused equipment was best cleaned using tap water. All the other important parameters relate to the Poly-L-Lysine and in particular to its molecular mass, its dilution and its freshness. Undiluted, not more than half a year old Poly-L-Lysine with maximal molar mass ($m_a \geq 300000\,\mathrm{Da}$) worked best and ensured the best adhesion.

2.1.1 Relation between Seflection and Force

The constitutive equation for the cantilever beam, and thus a relation between the deflection d of the beam at point $x = w$ and the applied force $F(x = L)$ on the tissue, can be derived from the Euler-Bernoulli beam theory [153]. Starting point is the differential equation of the deflection curve, which relates the curvature M/EI to the second derivate of the beams deflection z

$$EI\frac{\mathrm{d}^2 z}{\mathrm{d}x^2} = M, \tag{2.1}$$

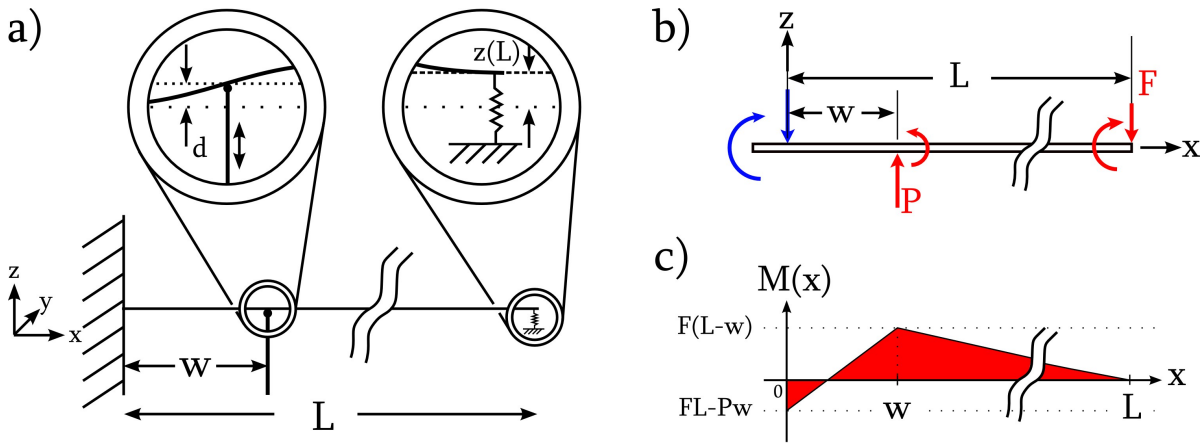

Figure 2.2 – The schematic in **a)** shows the cantilever beam deflected at length w about $d = z(w)$ and bended back at length L by the wing imaginal tissue, which is depicted as a spring. At the end of the beam the resulting deflection $z(L)$ of the stretched tissue equals to the deflection of the beam. The sketch in **b)** shows the applied forces of the deflecting stage P at $x = w$ and of the tissue at F at $x = L$ and the thereof resulting torques on the cantilever beam. In blue the resulting static force and torques at the cantilever's support are given. The diagram in **c)** shows the bending moment of the cantilever beam as a function of x.

where E is the Young modulus of the beam, I the second moment of area of the beam and M the bending moment acting on the beam. For beams with an rectangular cross-section the second moment of area can be calculated by

$$I = \frac{a^3 b}{12}, \tag{2.2}$$

where a is the depth of the beam parallel and b the height of the beam perpendicular to the applied load of the beam.
In figure 2.2 a) the tissue is modeled as a spring that resists the deflection of the beam at its end $x = L$. The deflection of the beam $d = z(w)$ equals a load $P = P(w)$, whose resulting deflection at the end of the beam $z(L)$ is resisted by the restoring force $F = F(L)$ of the tissue. To determine the stretching force of the tissue the constitutive equation for the beam was derived starting from a free body diagram. This is shown in figure 2.2 b) considering all forces and torques given by the structures constraints. Considering the distinct torques

$$\begin{aligned} -Pw + FL \quad & \text{at } x = 0 \\ F(L - w) \quad & \text{at } x = w \end{aligned}$$

the diagram in figure 2.2 c) can be deduced.
The bending moment $M(x)$ of the beam is thus

$$EIz''(x) = \begin{cases} -F(L-x) - P(x-w) & \text{for } x \leq w \\ -F(L-x) & \text{for } x > w. \end{cases}$$

Here, relation 2.1 was used. Integrating over x the shear force $V(x) = EIz'(x)$ is obtained:

$$EIz'(x) = \begin{cases} -FLx + \frac{1}{2}Fx^2 - \frac{1}{2}Px^2 + Pwx + C_1 & \text{for } x \leq w \\ -FLx + \frac{1}{2}Fx^2 - Px^2 + C_2 & \text{for } x > w. \end{cases}$$

Considering the boundary condition $EIz'(x=0)=0$ resolves the first integration constant to $C_1=0$. The necessity of continuity between both segments determines the second constant of integration to

$$C_2=\frac{1}{2}Pw^2.$$

Integrating over x for a second time and taking the boundary condition $EIz(x=0)=0$ and the continuity condition at $x=w$ into account the resulting constitutive equation is

$$EIz(x)=\begin{cases}-\frac{1}{2}FLx^2+\frac{1}{6}Fx^3-\frac{1}{6}Px^3+\frac{1}{2}Pwx^2 & \text{for } x\leq w\\ -\frac{1}{2}FLx^2+\frac{1}{6}Fx^3+\frac{1}{2}Pw^2x-\frac{1}{6}Pw^3 & \text{for } x>w.\end{cases} \tag{2.3}$$

The relation between the deflecting force P and the resulting force on the tissue F is found solving the constitutive equation for $x=w$:

$$P=\frac{F}{2w}(3L-w)+\frac{3EI}{w^3}d. \tag{2.4}$$

The deflection at the end $x=L$ is

$$EIz(L)=\frac{1}{6}Pw^2(3L-w)-\frac{1}{3}FL^3. \tag{2.5}$$

The force P is eliminated by insertion of equation 2.4, such that an expression for the effective applied force F on the wing imaginal tissue is found, which only depends on the properties of the used spring sheet and its deflections:

$$F=\frac{12EI\left(z(L)-\frac{(3L-w)}{2w}d\right)}{w(3L-w)^2-4L^3} \tag{2.6}$$

The deflection at $x=w$ was controled and set in a stepwise manner, while the resulting deflection $z(L)$ was measured under the microscope. Thus this formula was applied to specify and calculate the exerted force upon the wing imaginal disc. Rearranging this expression in a manner, such that the resulting force can be read as a result of the deflection $d=z(w)$ and is corrected by a term related to the deflection at the end of the beam $z(L)$, one obtains:

$$F=\underbrace{\frac{6EI}{w^2(3L-w)}\left(\frac{4L^3}{w(3L-w)^2}-1\right)^{-1}}_{D}\left(d-\underbrace{\frac{2w}{(3L-w)}}_{f}z(L)\right). \tag{2.7}$$

2.1.2 Calibration of the Cantilever Setup

Calibration measurements were done using a microforce sensing probe capable of measuring forces in a range of $\Delta F=1000\,\mu\text{N}$ with a specified resolution of $\sim 0.05\,\mu\text{N}$ [154].[1] The calibration of the cantilever beam was done by locking the beam in neutral position and approaching the cantilever beam at $x=L$ until contact was made. Thus the deflection of the beam at the end $x=L$ was zero, i.e. in equation 2.6 it is $z(L)=0$ for all times and the relation can be written as

$$F=\frac{6EI(3L-w)}{4L^3w-w^2(3L-w)}d. \tag{2.8}$$

Note, in this case everything except for d is constant throughout the experiment, and thus the equation is linear.

[1] The probe itself, which was a MEMS (Microelectromechanical system) device, could not be used to exert forces on the wing imaginal discs due to some limitations of the sensing probe. Firstly, the tissue could not be attached properly. Secondly, the probe's design did not fit to the experimental layout and lastly it can not be operated in wet environments as it would have been necessary.

Configuration	a [µm]	b [mm]	L [mm]	w [mm]	E [10^{11} Pa]	I [10^{-17} m^4]	D [N/m]	f
I	45(2)	13(1)	86(2)	29(1)	2.06(6)	9.9(7)	0.43(4)	0.253(7)
II	90(2)	13(1)	93(2)	26(1)	2.06(6)	79(3)	5.3(3)	0.205(5)

Table 2.1 – Set of parameters for the two configurations used throughout this work. Notation is as follows: a - depth of the beam, b - height of the beam, L - length of the beam, w - deflection point along the beam, E - Young's modulus of the beam, I - second moment of area, D - effective calculated spring constant for the cantilever beam and f the prefactor given in equation 2.7.

After unlocking the beam $F(d)$ was experimentally determined. The uncertainty in step size of the deflection stage was estimated to be in the range of $\delta_d = 1\,\mu\text{m}$ and the uncertainty of the measured force was estimated to be about $\delta_F = 10\,\mu\text{N}$. The estimated uncertainties are in a much broader range than the equipment's uncertainties, because vibrations, residual air flows within the laboratory and the off-set in deflection were taken into account.
Two different cantilever beams were deployed throughout this thesis, which mainly differed in the depth a, length L and the point of deflection w. The parameters for both configurations are presented in table 2.1 along with their uncertainties.[2]
The results of the calibration measurements for configuration I and II are presented in figure 2.3 together with the theoretical description of the respective configuration. In both diagrams the calculated and experimental determined forces match, which is why the effective spring constant D defined in equation 2.7 describes the cantilever beam properly. Therefore equation 2.7 was used to calculate the forces applied on wing imaginal discs.

[2]The number in parenthesis denotes the uncertainty in the last digit of the quoted value.

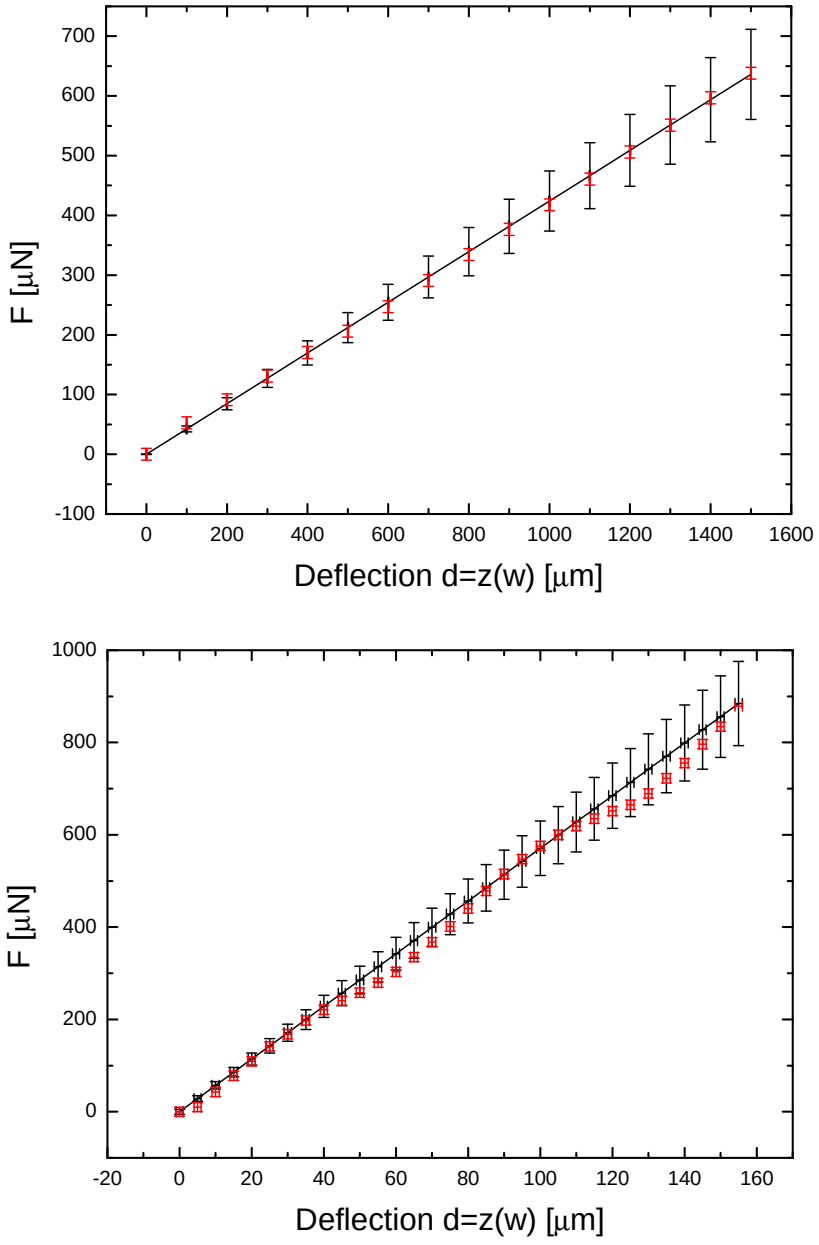

Figure 2.3 – Force-deflection curves in direct comparison for both configurations used. Configuration I is depicted on **top**; configuration II is depicted at the **bottom**. In **red:** Experimentally determined force-deflection curves. The error bars in d and F are considering uncertainties due to vibrations in the laboratory. In **black:** Calculated force-deflection $F(d)$ function. The error bars consider the uncertainties in the cantilever dimensions a, b, L, the deflection point w and the deflection d.

2.1.3 Experimental Preparations

This section will give an overview of the experimental preparation in a step-by-step manner:

1. *Preparation of microscope slides.* If using modified microscope slides these were prepared and assembled a day before usage. Directly before conducting an experiment an small area of the microscope slide was wetted with a droplet of Poly-L-Lysine and left to dry out. To quicken the drying process a hot-air gun was used. The movable coverslip was cleaned and coated with Poly-L-Lysine in a similar way.

2. *Dissection of the wing imaginal disc.* Late third instar larvae were dissected in isotonic PBS (phosphate buffered solution) and separated from their wing imaginal disc.

3. *Transfer of the wing imaginal disc.* The coated microscope slide was wetted with PBS and the wing imaginal disc transfered from the dissection stage to the microscope slide using a glass pipette.

4. *Attachment to the sample carrier.* The wing imaginal disc was placed at the desired position on the microscope slide by pulling the wing imaginal disc at residues of trachea. Its apical side was facing the microscope slide attaching the tissue only at its ventral end.

5. *Installation on the microscope.* The microscope slide with the attached wing imaginal disc was transfered to the microscope and aligned on it. Major criteria for the alignment has been that the symmetry axis of the wing imaginal disc was perpendicular to the edge of the movable coverslip, such that a homogeneous application of forces was warranted. Minor criteria has been the position of the sample relative to the objective.

6. *Attachement to movable cover slip.* The coverslip attached to the cantilever beam was positioned under the wing imaginal disc. The movement of the beam and thus the coverslip was monitored using the microscope, its height was controlled using the focus. An additional micro-manipulator with a glass finger was used to press the wing imaginal disc up on its dorsal side if necessary, such that the coverslip could be positioned beneath the disc. The glass finger was then used to attach the disc to the cover slip.

7. *Change of medium.* Finally the PBS was removed by suction and exchanged with a culture medium to supply a healthier and nutrient enriched environment for the tissue. In our case Clone 8 was used [155].

The procedure starting with dissection to the change of medium took about 10 min. The reason the larvae were dissected in PBS and not directly in the culture medium is that Clone 8 contains a lot of different biological molecules which bind to the coating and disable it.
Only late third instar wing disc were used for the conducted experiments as it was technically not feasible to install younger wing imaginal discs due to their small size. For some experiments the cantilever beam was deflected before the wing imaginal disc was attached to the cover slip of the cantilever beam. This preparation allowed in principle compression of the tissue by decreasing the deflection of the beam.

2.2 Materials and Methods

During this thesis the setup was used to built on two inverted microscopes: An *Olympus IX71* with an additional polarization unit and a *Leica SP1* confocal microscope.
The Olympus IX71 with polarization unit: The available contrast methods of the IX71 were brightfield microscopy and fluorescence microscopy due to a mercury lamp module [156]. A 4X, 10X, 20X and a 60X objective were installed of which the 60X was an oil-immersion objective [157]. Besides these standardized Olympus components an additional polarization unit, the "LC-PolScope", was integrated [158]. This polarization unit exploits the polarizing effect of liquid-cristals (LC) and extends the

traditional design of a polarization microscope. Instead of a compensator the LC-PolScope uses a unit consisting of two variable liquid cristals having their slow axis shifted about 45°to each other. This LC-unit is able to retard and shift the light in any direction. After acquiring five images at predetermined retarder settings, which takes between one and a few seconds, the associated software instantaneously calculates the retardance and slow axis for each pixel. Depending on the given setting the results are then displayed as heat map images. The sensitivity of the LC-PolScope can be up to 0.05 nm and better.
The Leica SP1: The Leica TCS-SP1 is the first generation of the Leica laser scanning confocal microscope series and was originally equipped with an Argon laser (458, 476, 488, 496, 514 nm) and a ultra-violet laser (405 nm) system. However, the SP1 used during this thesis was modified and the Argon laser system was replaced with a home-built light source, consisting of two solid state laser of the wavelengths 473 nm and 532 nm. During this thesis only the 473 nm wavelength was used for the experiments. The microscope was equipped with 10X, 20X and 40X objective of which the 40X was an oil-immersion objective. Additional modifications were made to the stage of the SP1. The microscope slide holder was redesigned and exchanged with a home-built one to maximize the area of support for the slides, a flute for the cantilever beam was milled out, such that it was on the same level as the microscope slide and the linear stage was mounted on top of the stage.

Stocks used:

1. E-Cad-GFP-III [159]
2. w; Lac-YFP (CPTI-002601)/(SM6a) [160]

In E-Cad-GFP-III flies epithelial cadherin (E-cadherin) is fused with the green fluorescent protein (GFP) [161, 162]. E-cadherin is enriched in the zonula adhesion that surrounds epithelial cells like a small belt and is localized most appically in invertebrate [163, 164]. In my experiments the fluorescent signal was found in a thickness of approximately 1 µm. These stocks are commonly used for fluorescent in-vitro imaging of the apical cell outline. Therefore, they were initially designated to explore the effect of stress on proliferation, but then were replaced with samples from Lac-YFP stocks. Finally, specimens from E-Cad-GFP-III stocks were mainly used to investigate the global elastic properties of the tissue; without actually using the fluorescent read-out.
In Lac-YFP flies the yellow fluorescent protein (YFP) is expressed in the septate junction complex, which is broader than the zonula adhesion and localized basal to it [165], such that it also can be utilized to identify the apical area of a cell. The fluorescent signal was found in a thickness of approximately 10 µm. These stocks were used to perform the experiments concerning the relation between proliferation rate and introduced stress, because the identification of mitotic cells was easier than in E-Cad-GFP-III samples. On the one hand the YFP signal was found to have a better signal-to-noise ratio, on the other hand mitotic cells could be identified over a $z-$range of 10 µm instead of 1 µm, making data analysis less error-prone.

3 Elastic Properties of the Tissue

In contrast to the bottom-up approach of Ishihara et al. [17], who calculated the forces between the cells of the wing pouch, I chose a top-down approach and considered the wing imaginal disc as a continuous medium. The relation between uniaxial applied planar stress and the resultant strain was studied in late third instar wing imaginal discs. The global elastic moduli E and Poisson's ratios ν were specified for the tissue in total and its partial regions: the hinge-notum region and the wing pouch.
The conducted experiments were force-extension measurements during which an external force F was applied in discrete steps. Top-view pictures were taken for the initial relaxed state of the wing imaginal disc and for each step in load. These pictures were analyzed using the open-source software *ImageJ* [166]. For each step in load the mechanical responses of the wing pouch region, the hinge and body-wall region and the tissue in total have been extracted from the taken pictures. These responses were the extension in length $\Delta L = L - L_0$ in $x-$direction and the constriction in width $\Delta w = w - w_0$ in $y-$direction. Here, L_0 is the beginning length and w_0 the beginning width of the wing imaginal disc in its relaxed state, while L is the length and w is the width of the wing imaginal disc under an applied load (please also refer to figure 3.1).
The tissue's response in height, i.e. in $z-$direction was not observable and thus could not be taken into consideration. The lengths were measured directly and sufficiently accurate using well traceable reference points. These reference points were the edges of the dorsal and ventral sides and folds and furrows within the wing imaginal disc. To find the average width of the tissue, it was necessary to take an intermediate step and calculate it using the area A of the respective regions. The width is then given by $w = A/L$ (see figure 3.1).
The uncertainties in length δ_L were found to be in the range of $\delta_L = \pm 3 - 4$px equaling a relative uncertainty in length of 1 - 3%. The relative uncertainties in area δ_A was of the same order, such that the uncertainty in width was of the order $\delta_w = \sqrt{2} \cdot \delta_L$.
The elongation of the tissue ε_x and its constriction ε_y were determined[1] from the inferred mechanical responses and from these physical variables the Poissons-ratio ν was derived (see section 3.2). The strains ε_x and ε_y were calculated deploying the true strain:

$$\varepsilon_x = \int \mathrm{d}\varepsilon_x = \int_{L_0}^{L} \frac{\mathrm{d}L}{L} = \ln\left(\frac{L}{L_0}\right) \tag{3.1}$$

$$\varepsilon_y = \int \mathrm{d}\varepsilon_y = \int_{w_0}^{w} \frac{\mathrm{d}w}{w} = \ln\left(\frac{w}{w_0}\right). \tag{3.2}$$

The uniaxial applied load F lead to an additional planar stress distribution within the tissue that is given by the true stress

$$\sigma = \frac{F}{A} = \frac{F}{w \cdot h} \tag{3.3}$$

with $A = w \cdot h$ the true cross-section for each step of applied load.
Most measurements were performed using the Olympus IX71 allowing to inquire concurrently the tissue's changes in shape and in its global retardance distribution (see section 3.4). However, due to the high convolution along the path of light (brightfield microscope), it was unfeasible to reliably focus on the

[1] The experimental design can only accounts for changes in lengths in a specific direction (normal strains) and not for changes with respect to two directions, i.e. in angle (shear strain). The normal strains ε_{xx} and ε_{yy} are thus referred to as ε_x and ε_y.

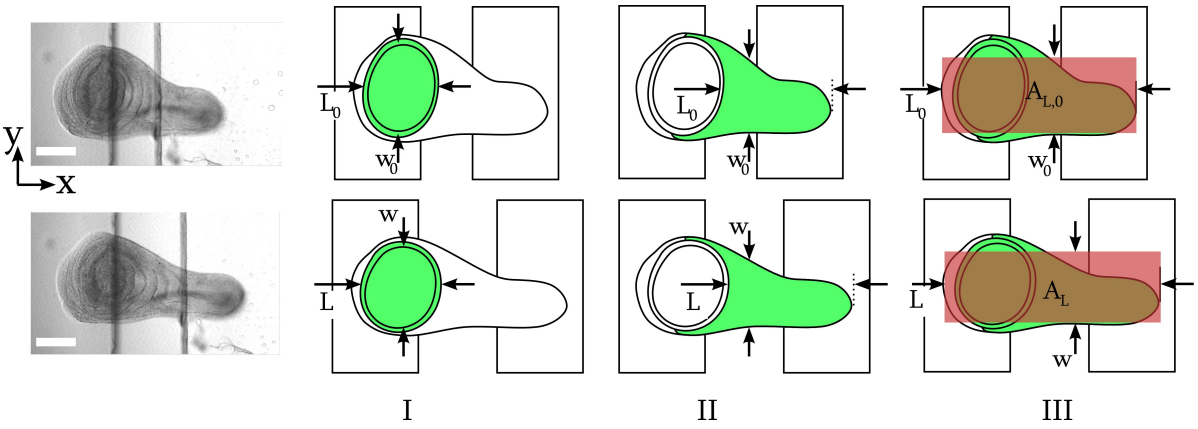

Figure 3.1 – The top row shows sketches of an unstretched wing imaginal disc directly after mounting on the pulling setup; the bottom row depicts the same disc, which is stretched due to an externally applied force F (and is thus under additional normal stress σ). The monitored responses are the length L and width w of the wing pouch (scheme **I**) the hinge and body wall region (scheme **II**) and the total length of the wing imaginal disc (scheme **III**). To obtain a reliable value for the average width of the particular region the width was determined via the area A of the region (only shown for scheme **III**). Scale bar equals 100 µm.

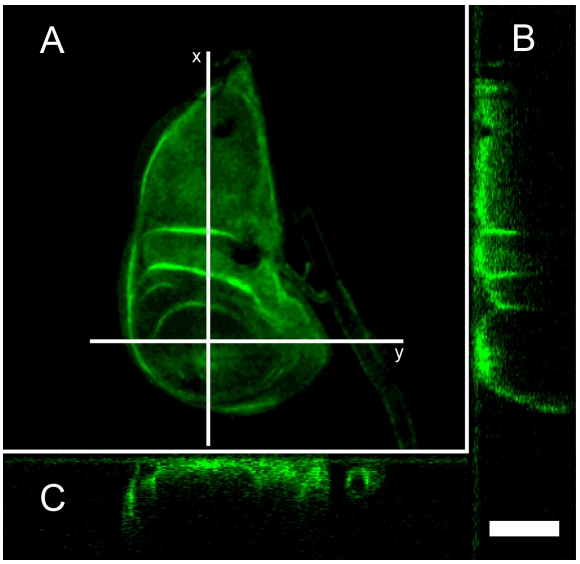

Figure 3.2 – **A:** Averaged projection of a confocal $z-$stack. The specimen was a late third instar wing imaginal disc in culture medium marked with E-Cad-GFP-III. The positions of the taken xz cross-sections (**B**) and yz cross-section (**C**) are shown by white lines. The xz cross-sections does not allow any conclusions on the thickness of the tissue, but reveals the folded structure of the tissue, which is typical at that stage. Scale bar equals 100 µm.

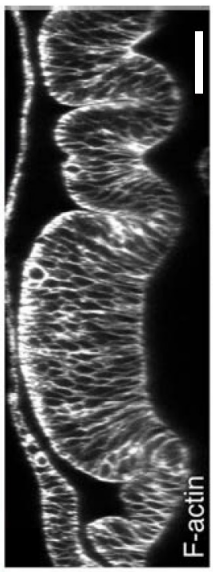

Figure 3.3 – Cross-section of a late third instar wing imaginal disc, stained for filamentous (F-)actin, reveals the topology of a late third instar wing imaginal disc. The thickness of the wing pouch and of the folded hinge region seem similar to be in thickness when neglecting the folded topology of the hinge region. Taking the folded topology into account, the true thicknesses differ by a factor of 1.4. Scale bar equals 25 µm. Figure taken and modified from [167].

Averaged spring constants			
k_p [N/m]	k_{hn} [N/m]	k_t [N/m]	k_{eff} [N/m]
2.3(1)	1.2(1)	0.8(1)	0.8(1)

Table 3.1 – Average spring constants for the wing pouch k_p, the rest of the tissue k_r and the wing imaginal disc in total k_t. The effective spring constant k_{eff} was calculated considering the wing pouch region in series with the hinge-notum region.

apical or basal surface of the sample. Thus it was not possible to measure the height h and especially the constriction in height Δh. Using the Leica SP1 would in principal have allowed to determine the depth of the investigated sample if a sufficient markers were available. When the experiments were conducted no such marker was available or known of that would have allowed for a precise determination by live tissue microscopy. Indeed, the apical and the basal side of the wing imaginal discs are normally visualized by immunostaining the tissue. Figure 3.3 shows an example of late third instar wing imaginal disc immunostained for filamentous (F-)actin [167]. The thickness of the tissue as well as its topological structure is well outlined. In contrast to images of immunostained samples confocal images of live E-Cad-GFP-III or Lac-YFP wing imaginal discs are neither suited to determine the tissue's thickness nor its constriction in height. Figure 3.2 shows an example of late third instar wing imaginal disc floating in culture medium.
Thus, to calculate the true stress that was applied on the tissue, averaged thicknesses were used, taken from [167] and [168]. Nevertheless, the tissue's constriction in height was considered under the assumption of being an isotropic material (also refer to chapter 3.3).

3.1 Force-Extension Measurements

The acquired raw data were the responses in length and width due to the externally applied load. A typical force-extension curve for the different parts of a late third instar wing imaginal disc for the change in length ΔL and the related change in width Δw are shown in figure 3.4. Cubic regressions made, quickly pointed to the fact, that the responds of the tissue and its regions can be approximated by Hooke's law. In figure 3.4 the linear approximation are provided with its residues. For the same applied load ΔF the different regions of the tissue showed different mechanical responses, such that they can be described by different spring constants. In general, the wing pouch region (in red) elongates much less than the hinge-notum region (in green). An instance of a single wing imaginal disc is shown in figure 3.4, its wing pouch region corresponding to a spring constant of $k_p = 2.7(1)\,\text{N/m}$ and its hinge-notum region corresponding to a spring constant of $k_{hr} = 1.4(1)\,\text{N/m}$. While the extensions in length ΔL_p and ΔL_{hn} add up to the total extension in length ΔL_t the total constriction in width w_t is mainly given by the response of the hinge-notum region.
Force-extension measurements on nine different samples had been made to determine the elastic properties of the wing imaginal disc. The collected raw data is shown in figure 3.5. The residues of the linear fits show a high fluctuation due to the natural variation in elastic properties.
Considering the hinge-notum region and the wing pouch as springs in series the calculated effective spring constant for the data in figure 3.4 is $k_t^{-1} = k_p^{-1} + k_{hn}^{-1} = 0.8(1)\,\text{N/m}$ and equals the experimentally determined value for the tissue in total $k_t = 0.9(1)\,\text{N/m}$.
The average of spring constants k_p, k_{hn} and k_t and their standard deviations can be found in table 3.1. Note, the different spring constants can either result from the different geometries of the areas or from different inherent mechanical properties. This issue is thus further addressed in chapter 3.3.

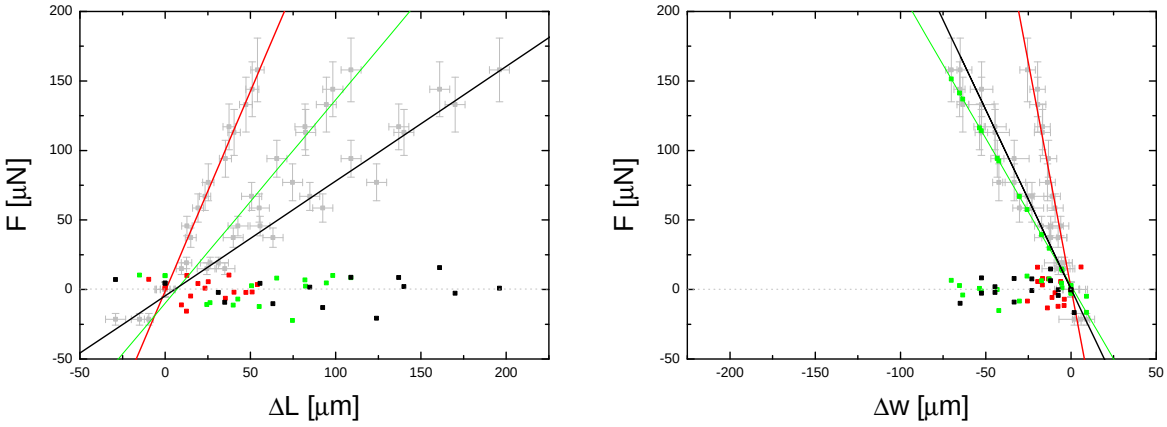

Figure 3.4 – On the left a typical force-extension curves for the length of a wing imaginal discs. On the right the corresponding force-constriction curves. Raw data is indicated in grey, while the linear approximation and residues are coded in different colors. The wing pouch region is indicated in red, the hinge-notum region in green and the wing imaginal disc in total in black.

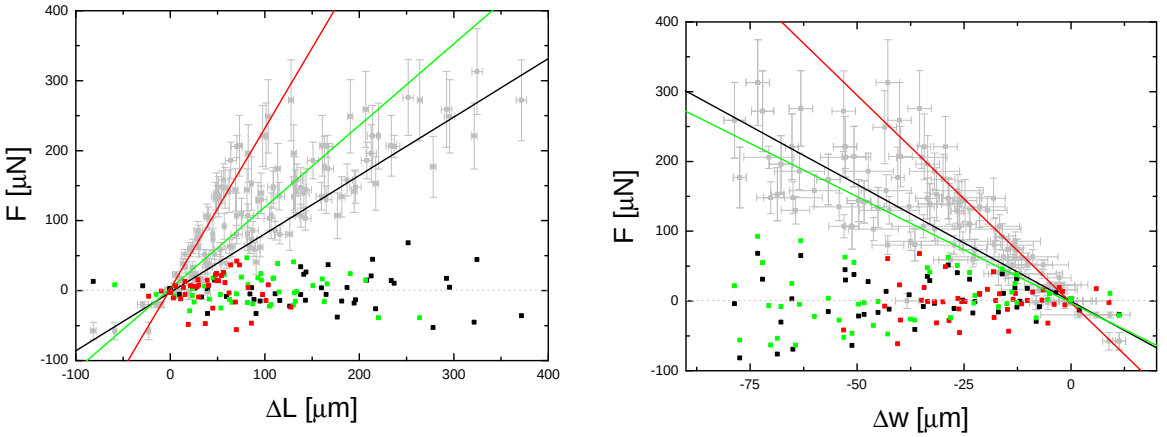

Figure 3.5 – Force-extension, respectively force-constriction curves of $N = 9$ wing imaginal discs. Due to the natural variation the residue fluctuation is much higher.

	$\varepsilon_x \leq 0$	$\varepsilon_x \geq 0.25$
$\overline{\nu_p}$	0.33(15)	0.41(8)
$\overline{\nu_{hn}}$	0.29(19)	0.74(13)
$\overline{\nu_t}$	0.24(19)	0.61(14)

Table 3.2 – Averaged Poisson-ratios for compressional strains $\varepsilon_x \leq 0$ and tensional strains $\varepsilon_x \geq 0.25$ of the wing pouch $\overline{\nu_p}$, the hinge-notum region $\overline{\nu_{hn}}$ and the tissue in total $\overline{\nu_t}$.

3.2 Poisson's ratio of the Wing Imaginal Disc

The Poisson's ratio is defined as the negative ratio of transverse strain to longitudinal strain and thus is calculated as

$$\nu = -\frac{\varepsilon_y}{\varepsilon_x}. \tag{3.4}$$

In classical elasticity theory the numerical limits for an unconstrained isotropic material are found to be in the range of $-1 < \nu < 0.5$. The reason for ν to lie within these boundaries comes from the physical requirement of material stability and derives from the condition that the Young's modulus E, the bulk modulus K and the shear modulus G must be positive.[2] The Poisson's ratio reveals the tendency of a material to undergo a change in shape or volume when subjected to mechanical loading and virtually all common materials have a positive Poisson's ratio ranging from $0 < \nu < 0.5$, because most materials resist a change in volume (determined by the bulk modulus B) more than a change in shape (determined by the shear modulus G) [169, 170].
Poisson's ratio of $\nu \sim 0.5$ thus describes a highly incompressible material that conserves its volume when stretched by constricting in both transversal directions. However, objects can exceed this upper limit of ν and still be stable. These objects are either constrained at or by their surface, such that the constriction in one dimension is neglectable or they are elastic anisotropic. Then an incompressible material can show a conservation of area, rather than volume, such that the upper limit of Poisson's ratio becomes $\nu \sim 1$ and the transversal strain of only one dimension mainly compensates for the increase in longitudinal strain.

In figure 3.6 the distribution of Poisson's ratio for the wing pouch and the hinge-notum region are shown. The distribution for the entire tissue is depicted in the left diagram of figure 3.7. On the right diagram of figure 3.7 the reduced data of all three distributions are shown in comparison. Samples are the same as in section 3.1.

The Poisson's ratios ν have been found to increase in the range of $0 < \varepsilon_x \lesssim 0.25$ and approximately constant for compressional strains $\varepsilon_x < 0$ and tensional strains $\varepsilon_x \gtrsim 0.25$. While the Poisson's ratio for the wing pouch is only increased about 24% for tensional strains $\varepsilon_x > 0.25$ and still below the theoretical limit of 0.5 for a bulk material, the hinge-notum region and the tissue in total increase about 155% and exceeds the classical limit for $\varepsilon_x \gtrsim 0.25$. The Poisson-ratios are given in table 3.2. The behavior of the total tissues Poisson's ratio ν_t reflects a combination of the Poisson-ratios of the wing pouch ν_p and the hinge-notum region ν_{hn} and is thus dominated by the behavior of ν_{hn}. The total tissues Poisson's ratio was found to be given by the mean $\nu_t = (\nu_p + \nu_{hn})/2$, such that for the further discussion mainly the partial regions will be regarded.
Main results are the different margins of the Poisson's ratio for the two regions and the strong dependency of Poisson's ratio on the uniaxial strain, especially for the hinge-notum region. The observed margin of ν_p indicates that the wing pouch could be described as a three dimensional or bulky material

[2] For instance this can be seen in the relations between Young's, bulk and shear moduli $E = 2G(1+\nu)$ and $K = E/(3(1-2\nu))$ can be considered.

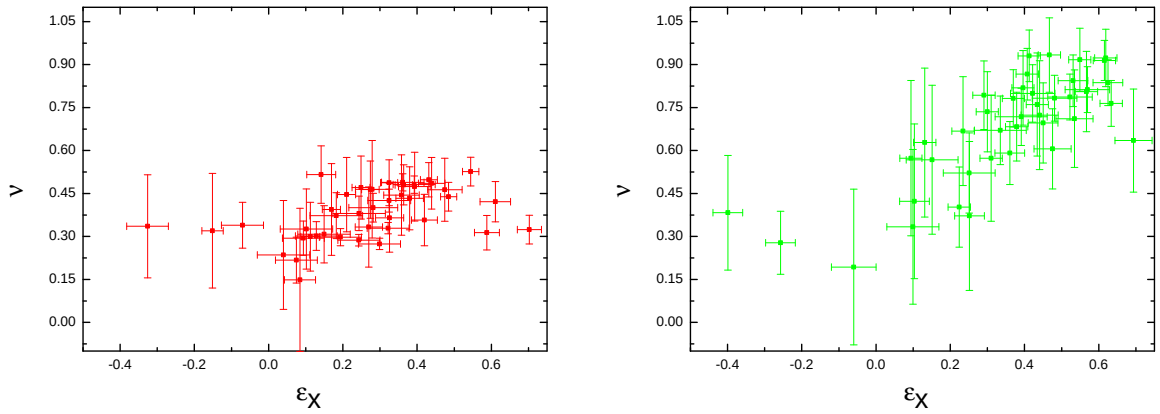

Figure 3.6 – Poisson's ratio distribution $\nu = \nu(\varepsilon_x)$ for the wing pouch (in red) and the hinge-notum region (in green).

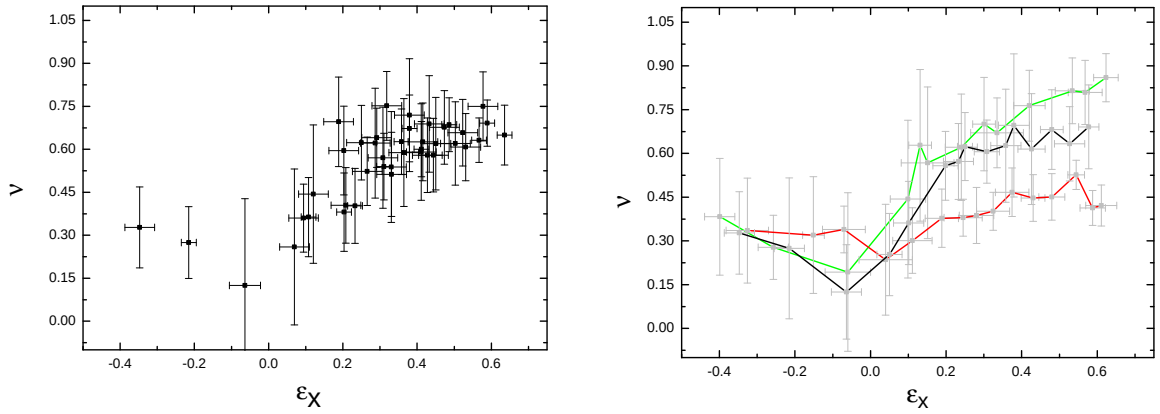

Figure 3.7 – **Left:** The Poisson's ratio $\nu = \nu(\varepsilon_x)$ for the wing imaginal disc in total. **Right:** All Poisson-ratios $\nu = \nu(\varepsilon_x)$ in comparison. The number of data points was reduced by a factor of three by averaging all points within a relative distance of $\varepsilon_x = 0.017$. The Poisson-ratios for the hinge-notum region, wing pouch and the tissue in total show similar behaviors. For negative strains the Poisson-ratios can be considered equal and rises for intermediate longitudinal strains $0 \lesssim \varepsilon_x \lesssim 0.25$ and converges to different high values for higher strains.

that compensates for its change in volume by equal constriction in widht w and height h. In this description the wing imaginal disc is seen as an elastically isotropic material. The Young's moduli for the lateral and transversal axis were found to be equal (see section 3.3), but no information was retrieved about the Young's modulus as the height was not accessible for the reasons mentioned above. Based on the margin and behavior of ν_p the assumption is made that the wing disc shows the same elastic property in height as it does in plane.
In contrast, the upper margin of ν_{hn} indicates that the hinge-notum region should be described otherwise. Possibly, the tear-drop form of the wing imaginal disc and especially the narrowing of the hinge-notum region could have an important influence and lead to a bias in ν_{hn}. The narrowing of the tissue from the ventral to the dorsal side could lead to an additional transversal force which then results in an additional and so far disregarded constriction. To decide whether or not this additional constriction is significant for the calculation of the Poisson's ratio, the following considerations are made: These additional transversal force can be estimated by $F\tan(\alpha)$, when α is the angle between the axis of uniaxial applied force F and the outline of the hinge-notum region. The additional constriction then would be $\Delta w \cdot \tan(\alpha)$, such that the observed Poisson's ratio would be increased by the geometrical factor $(1 + \tan(\alpha))$ compared to an unbiased Poisson's ratio. If the hinge-notum region's Poisson's ratio is biased and genuinely below 0.5, the correction of the geometrical factor should be in the order of ~ 2 and as a consequence the angle α has to be near $\sim 45°$. For unstretched wing imaginal discs the highest angle is observed, which is in the order of approximately 25°. During stretching the angle decreases until it reaches $\alpha = 10°$. This contradicts the observation that the Poisson's ratio increases for increasing tensile strains. Furthermore, the observed angle and the resulting correction factor are too small to decrease the maximal values of ν_{hn}, sufficiently. Considering all these arguments, the idea of a major influence of the wing imaginal discs geometry and an significant influence of an additional disregarded constriction on the Poisson's ratio ν_{hn} was discarded.
Under the premise, that the Poisson's ratio ν_{hn} is genuine, the hinge-notum region's unusual behavior can be understood as the result of different circumstances. Firstly, the cellular structure of the wing imaginal disc should have a reasonable effect. The transmission of force mainly happens through the upper layer of the apical side, where the cells of the wing imaginal disc are mainly interlinked by adheren junctions. Secondly, the hinge-notum region is considerably thinner than the disc pouch and thus could be approximated as a plane stress system. As a rule of thumb a system is considered to be representable by planar stress when its thickness h is small, typcially 10% or less than the shortest in-plane dimension [153, 171]. Taking an average thickness of $h_{hn} = 35(5)\,\mu\text{m}$ and average width $w_{hn} = 215(20)\,\mu\text{m}$ the ratio becomes 16(3)%. The ratio for the wing pouch using the average thickness $h_p = 50(3)\,\mu\text{m}$ and average length[3] $L_p = 150(30)\,\mu\text{m}$ is about 33(7)%. Values for the heights were taken from [167, 168]. Although the ratio for the hinge-notum region does not meet the empirical criterium perfectly, it is in its order of magnitude and by a factor of two smaller than the relation of the wing pouch. In this case, all applied stresses are restricted to the $xy-$plain and all stresses in regard to the $z-$axis are neglectable. Then the constriction in thickness Δh is neglectable compared to Δw_{hn} and ΔL_{hn} and the height can be treated as constant during the course of experiment. The different dimensions of the two regions can thus be assumed to be the reason for the different margins of their Poisson-ratios.

The observed increase of ν_p and ν_{hn} in the interval of $0 < \varepsilon_x \lesssim 0.25$ from one plateau to the other correlates with a increase of the Young's modulus at $\varepsilon_x \sim 0.25$ (see section 3.3). This phenomena can be explained wrinkled or folded structure of late third instar wing imaginal discs. Assuming the unfolded length of late third wing imaginal disc is about one fourth longer than the folded length, then the wing imaginal disc is mainly to be unfolded in the range $0 < \varepsilon_x \lesssim 0.25$ before the tissue itself becomes stretched. When considering an hypothetical, ideal folded plate without any boundary restrictions a planar and uniaxial applied load will unfold the structure. During the unfolding process no transversal constriction will be induced and thus the Poisson's ratio equals zero until the observed plate

[3]For the wing pouch L is the smallest dimension.

is completely unfolded. Then the Poisson's ratio will change to its true value. However for late third instar wing imaginal discs the Poisson's ratio does not equal zero for any strains ε_x. Up to this stage the reasons for this deviated behavior can only be assumed. A possible explanation could be the boundary restriction of the wing imaginal disc. On the one hand the folds do not completely run-through the tissue from side to side and are better described as furrows slightly encircling the wing pouch. Thus the wing imaginal disc are enclosed by a stripe of unfolded tissue. On the other hand there is the peripodial membrane that spans over the columnar layer and could dominate the elastic behavior for strains $0 < \varepsilon_x \lesssim 0.25$, where the contribution to the elastic response of the columnar layer is low. For a detailed understanding finite-element simulations should be considered.

3.3 Stress-Strain Measurements

In section 3.1 the different regions of the wing imaginal disc were described as different linear elastic springs in series.
However, the spring constant k not only depends on the material itself but also on the dimensions of the material, why for the characterization of a material under tensile stresses the elastic modulus or Young modulus E is used. If Hooke's law holds for the material the Young's modulus can be directly determined from

$$\sigma = E\varepsilon \tag{3.5}$$

and then the spring constant can be written as $k = E \cdot A/L$.[4] Whether the observed spring constants differ due to different geometry of the tissue or an inherent difference of the material itself is part of this section, in which the determination of the Young's modulus of late third instar wing imaginal discs is described and discussed.
The applied load F on the wing imaginal disc results in a normal stress that in principle is $\sigma = F/A$ with A the cross-section normal to the load. For each investigated region the cross-section $A = w \cdot h$ had to be calculated using the actual height h and width w. The calculations of the normal stresses were taking into account that the height of the wing pouch constricts while the height of the hinge-notum region can be considered constant at h_0. The constriction in thickness of the wing pouch can be considered by deploying its Poisson-ration ν_p and the engineering strain $\varepsilon_z = \Delta h/h_0$. Then the height can be expressed as $h = h_0 + \Delta h = h_0(1+\varepsilon_z) = h_0(1+\varepsilon_x\nu)$. According to equation 3.3 the stresses for the wing pouch and hinge-notum region are then calculated by:

$$\sigma_p = \frac{F}{w_p \cdot h_{0,p}(1+\varepsilon_x\nu_p)}, \qquad \sigma_{hn} = \frac{F}{w_{hn} \cdot h_{0,hn}} \tag{3.6}$$

The strains ε_x and ε_y were calculated using equations 3.2 for the true strains. All uncertainties were completely propagated for all calculated quantities.
Figure 3.8 shows the calculated stress-strain curves for five force-extension experiments conducted on a single wing imaginal disc. Figure 3.9 shows the stress-strain curves for the set of nine samples. The left column of figure 3.8 and 3.9 shows the axial while the right column shows the transversal stress-strain curves. The top row shows the retrieved data for the wing pouch, the middle row for the hinge-notum region and the bottom row for the wing imaginal disc in total. Similar to the course of the Poisson-ratios the stress-strain curves of the axial applied stress changes at $\varepsilon_x \gtrsim 0.25$ having the slope of the curve increasing significantly. The observed kink truncates the data into two intervals of linear functions $\sigma(\varepsilon_x \lesssim 0.25)$ and $\sigma(\varepsilon_x \gtrsim 0.25)$. The position of the kink in the transversal stress-strain curves was found at $\varepsilon_y = \varepsilon_x\nu$. Linear regression was done in each interval separately. The linear approximation and its residues of the intervals $\varepsilon_x \lesssim 0.25$ were color-coded in blue, the color-code for the intervals $\varepsilon_x \gtrsim 0.25$ was chosen according to the particular probed region.
The longitudinal stress $\sigma_x = \sigma$ causes a transversal stress $\sigma_y = -\nu\sigma$, which again causes the monitored

[4] Note, that this relation is derived using the engineering strain $\varepsilon = \Delta L/L$.

	E_x [kPa]		E_y [kPa]	
	$\varepsilon_x \lesssim 0.25$	$\varepsilon_x \gtrsim 0.25$	$\nu\varepsilon_x \lesssim 0.25$	$\nu\varepsilon_x \gtrsim 0.25$
wing pouch	43(13)	130(26)	44(38)	115(48)
hinge-notum region	41(9)	128(19)	44(34)	109(36)
tissue in total	44(8)	122(17)	41(43)	109(43)

Table 3.3 – Young's moduli for the x and y direction for $N = 9$ samples for the intervals $\varepsilon_x \lesssim 0.25$ and $\varepsilon_x \gtrsim 0.25$, respectively $\nu\varepsilon_x \lesssim 0.25$ and $\nu\varepsilon_x \gtrsim 0.25$ with $\nu = \nu(\varepsilon_x)$. (with $\nu = \nu(\varepsilon_x)$)

	E_x [kPa]		E_y [kPa]	
	$\varepsilon_x \lesssim 0.25$	$\varepsilon_x \gtrsim 0.25$	$\nu\varepsilon_x \lesssim 0.25$	$\nu\varepsilon_x \gtrsim 0.25$
wing pouch	47(41)	132(66)	47(60)	97(60)
hinge-notum region	36(11)	125(38)	40(41)	103(40)
tissue in total	43(10)	116(20)	40(36)	103(46)

Table 3.4 – Young's moduli for x and y direction to the data of the wing imaginal disc in figure 3.8 for the intervals $\varepsilon_x \lesssim 0.25$ and $\varepsilon_x \gtrsim 0.25$, respectively $\nu\varepsilon_x \lesssim 0.25$ and $\nu\varepsilon_x \gtrsim 0.25$. (with $\nu = \nu(\varepsilon_x)$)

constriction in width ε_y [172]. Thus in case of a linear relation the Young's modulus in direction of the axial applied load E_x and in the transversal direction E_y can be calculated by:

$$\sigma = E_x\varepsilon_x, \qquad -\nu\sigma = E_y\varepsilon_y. \tag{3.7}$$

The stress-strain curves in figure 3.8, that were acquired by stretching a wing imaginal disc five times, illustrate two intriguing observation that have been made. First, no mechanical hysteresis was observed. Second, the slope changed reproducibly, rather sharp and independently of the tissue's region.
The data in figure 3.8 was acquired over a period of an hour during which the wing imaginal disc was kept in Clone8 culture medium. The self-imposed restriction to an hour was made to be sure that the observed sample is in a considerably good state of health even if kept in a phosphate-buffered solution (PBS) instead of culture medium. Wing imaginal discs kept in PBS for longer than an hour were very likely to frazzle on their edges and then suddenly showed loss of elasticity, respectively plastic behavior (compare to chapter 3.5).
The change of slope of the stress-strain curves for stretches of approximately 25% is most obvious for the hinge-notum region, respectively for the entire tissue. The specified elastic moduli for the wing imaginal disc in figure 3.8 are listed in tabular 3.4 and in tabular 3.3 the average elastic moduli for all samples are found (see figure 3.9). The elastic moduli for the transversal and longitudinal direction are in good agreement, such that the wing imaginal disc can be characterized at least in plane as an isotropic elastic material. Apparently the stiffness of the wing imaginal disc increases approximately 2 – 2.5 times for tensile strains higher than 0.25. The reason is probably the folded topology of late third

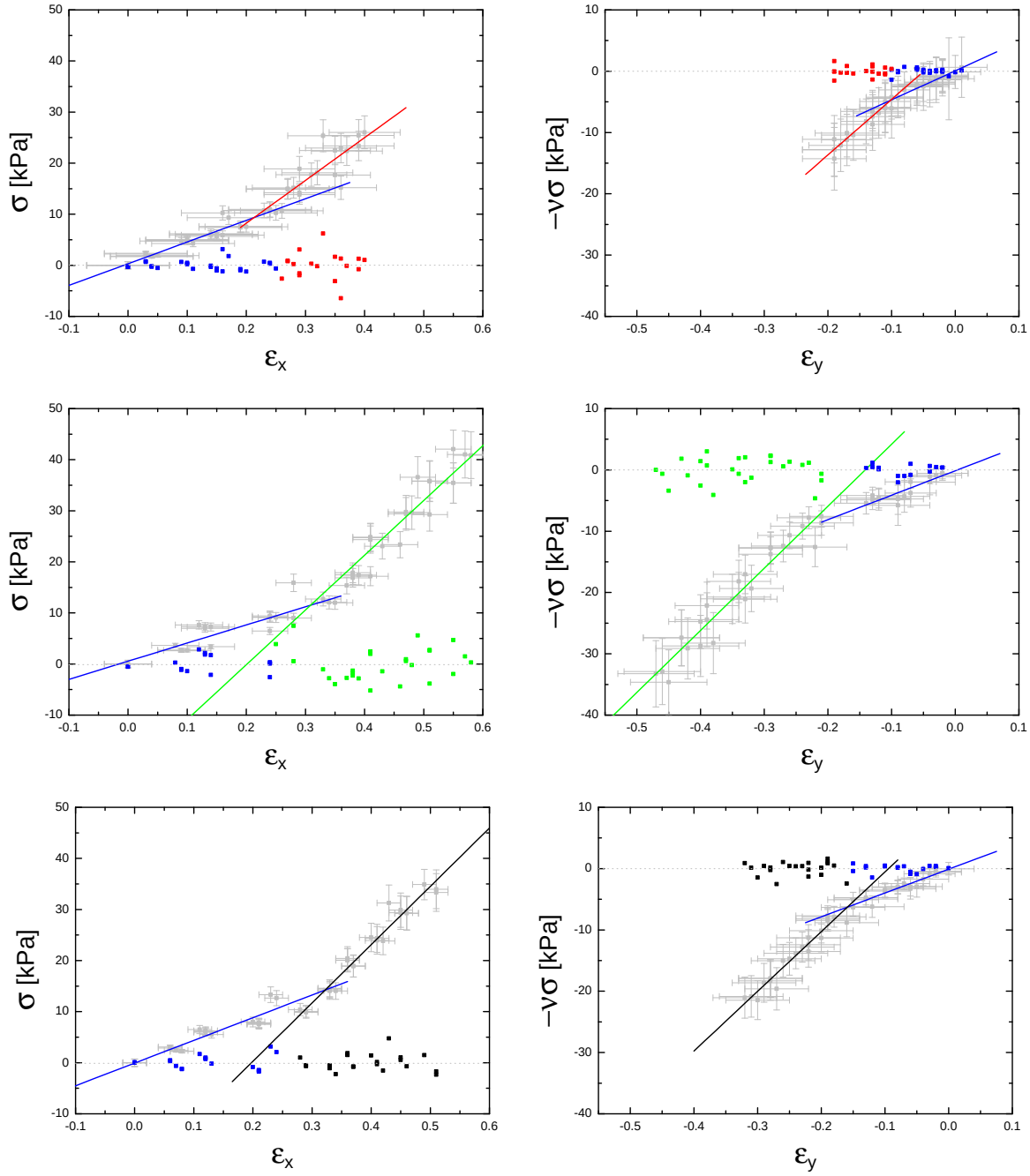

Figure 3.8 – Stress-strain curves for a single wing imaginal disc. During the course of one hour five force-extension curves were performed, repeatedly exhibiting the same elastic behavior. Left column shows the stress-strain for the axial direction x and the right column for the transversal direction y. In the top row the results for the wing pouch (red) are found, in the middle for the hinge-notum region (green) and at the bottom for the tissue in total (black). All experiments display a sharp change in slope at $\varepsilon_x \sim 0.25$, respectively at $\varepsilon_y \sim \nu\varepsilon_x$ for the transversal results. The scattered points are the residues to the corresponding linear fits. In blue the linear regressions for $\varepsilon_x < 0.25$.

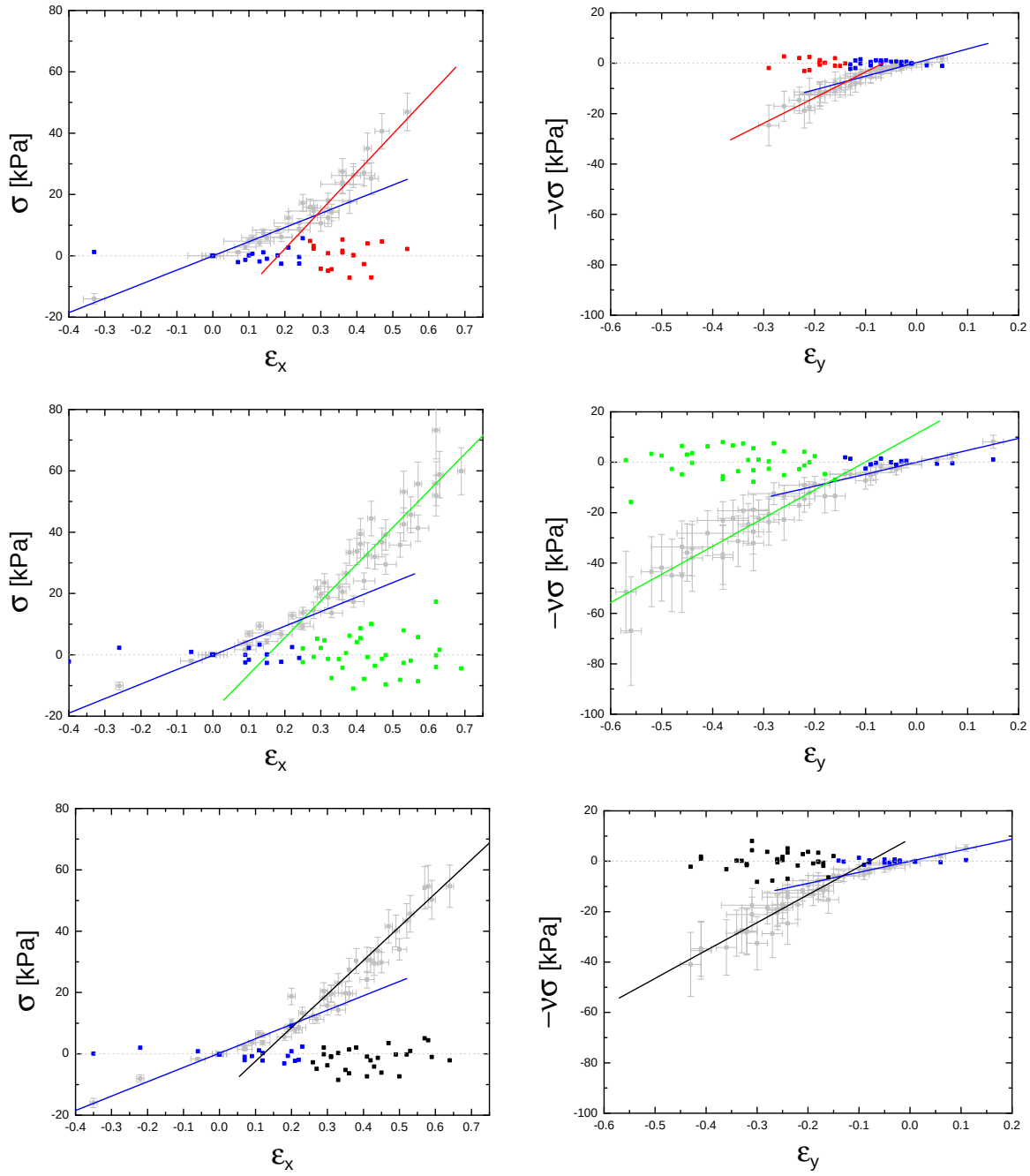

Figure 3.9 – Stress-strain curves of force-extension experiments of $N = 9$ samples. Left column shows the stress-strain for the axial direction x and the right column for the transversal direction y. In the top row the results for the wing pouch (red) are found, in the middle for the hinge-notum region (green) and at the bottom for the tissue in total (black). All axial results display a kink at $\varepsilon_x \sim 0.25$ and accordingly the transversal results display a kink at $\varepsilon_y \sim \nu\varepsilon_x$. In blue the linear regressions for $\varepsilon_x < 0.25$.

instar wing imaginal discs as first argumented for section 3.2.
Whether or not this can explain the observed factor in Young's moduli the following considerations are made:
The furrows within the tissue are most obvious for the hinge-notum region although they are also present around the wing pouch. To estimate the influences of the wing imaginal discs topology it will be modeled as simple as possible, namely a bending plate. If R is the radius of curvature and L the length of the bended plate, E the materials true Young's modulus and $I = h^3 w/12$ the second moment of inertia then the bending energy U is [153, 173]:

$$U = \frac{EI}{2}\frac{L}{R^2}.$$

Treating the folds like springs, the bending energy must equalize the potential energy

$$W = \frac{1}{2}k'\Delta L^2,$$

where $k' = E'A/L$ is the observed spring constant, respectively elastic modulus and $\Delta L = L - 2R$ the total extension of the folded sheet, assuming it is maximal folded at the beginning. Idealizing the folds as pure and circular bending the last assumption of $\pi R = L$ can be made. This leads to following expression:

$$E' = \frac{\pi^2}{12(1-2/\pi)^2}\frac{h^2}{L^2}\cdot E \approx 6.23 \cdot \frac{h^2}{L^2}E \tag{3.8}$$

With $h = 35\,\mu\text{m}$ and the length of a fold in the range of $L = 110 - 160\,\mu\text{m}$, estimated from figure 3.3 and 3.2 the correction factor is about 0.30 – 0.63, respectively 1.6 – 3.35. These crude considerations already imply that the difference in Young's moduli is partly due to the topology of late third instar wing imaginal discs. For tensile strains smaller than 0.25 the tissue is still not completely unfolded and the observed stiffness then mainly reflects the unfolding process. For tensile strains bigger 0.25 the load fully applies onto the material, such that the Young's modulus for $\varepsilon_x \gtrsim 0.25$ should be considered as the tissue's true elastic modulus.

3.4 Determinaton of the Photo-Elastic Constant

Birefringence is the difference of the refractive indices of the extraordinary and ordinary axis $\Delta n = n_{eo} - n_o$ and is proportional to the difference of principle stresses $\Delta\sigma = \sigma_1 - \sigma_2$ in photo-elastic materials. Light traversing a birefringent material encounters a phase-shift or retardance R, which is given by the birefringence of the material Δn and the physical length of the optical path h:

$$R = \Delta n \; h.$$

Then an observed retardance distribution can be directly related to a materials inner stress distribution

$$R = \; C \; h \; (\sigma_1 - \sigma_2).$$

when the material constant C is the stress-optical coefficient or photo-elastic constant is known.
In [16] Nienhaus et al. utilized the retardance of polarized light as stress read-out and discovered that retardance builts up with rising age and peaks within the wing pouch. The samples they investigated were kept in isotonic ringer solution and were either attached to a sample carrier in an unperturbed state or elongated roughly 30% by hand. But due to the lack of the photo-elastic constant C and the elastic modulus E of the wing imaginal disc, they could neither quantify nor estimate the internal stresses.
In order to determine the global photo-elastic constant of wing imaginal tissue, controlled stresses must be exerted on the tissue, while concurrently the change in birefringence is measured. The stretching setup was therefore used in combination with the polarization microscope, such that the relation between retardance ΔR, respectively the orientation of the slow axis and the applied lateral stress $\Delta\sigma_x$ could be investigated.
Similar to the experiments described in section 3.1, an external force was applied in discrete steps and at each step a birefringence measurement was performed. Such a measurement comprised the spatial retardance distribution and orientation of the slow axis of the birefringent tissue, which is given by the azimuth.[5] A visualization of spatial retardance and azimuth data for a wing imaginal disc that was exerted to compressional and tensile stresses is shown in figure 3.10.[6] A clear change in peak retardance and orientation is revealed when the retardance and orientation heat-maps of the compressed state are compared to the initial and stretched state. However, such an obvious and locally confined change in retardance and orientation was usually not observed. In most cases the retardance and its orientation changed more evenly distributed within the tissue. For this reason and to account for inhomogeneities of the tissue – be it of topological or elastic nature – mean retardances were evaluated. The generated birefringence data was therefore visualized as 8 bit grey-scale images either representing the retardance R or azimuth ϕ. From these images average gray values were retrieved for the wing pouch, the hinge-notum region and the tissue in total. Averaged values of the background were also extracted to take the birefringence of the cover slip into account and remove a possible bias. These values were then converted to absolute retardances, respectively orientations, with a relative uncertainty of $\sim$2%.

The externally applied forces induces stresses, which are longitudinal, respectively transversal to the axis of the applied force. At step i in force these stresses lead to a retardance which is

$$R_i = \; C \; h_i \; (\sigma_{x,i} - \sigma_{y,i}). \tag{3.9}$$

The change in retardance ΔR from the initial unstretched state R_0 to R_i is then

$$\frac{R_i}{h_i} - \frac{R_0}{h_0} = \; C \; \left((\sigma_{x,i} - \sigma_{y,i}) - (\sigma_{x,0} - \sigma_{y,0})\right).$$

[5] The azimuth is determined by the polarization microscope as the angle relative to the horizontal axis, that is to the $x-$axis, which is defined in figure 3.1..

[6] Technically the visualization of the slow axis' orientation is a combination of heat and intensity map. The colormap represents the azimuth, while the brightness gives the retardance.

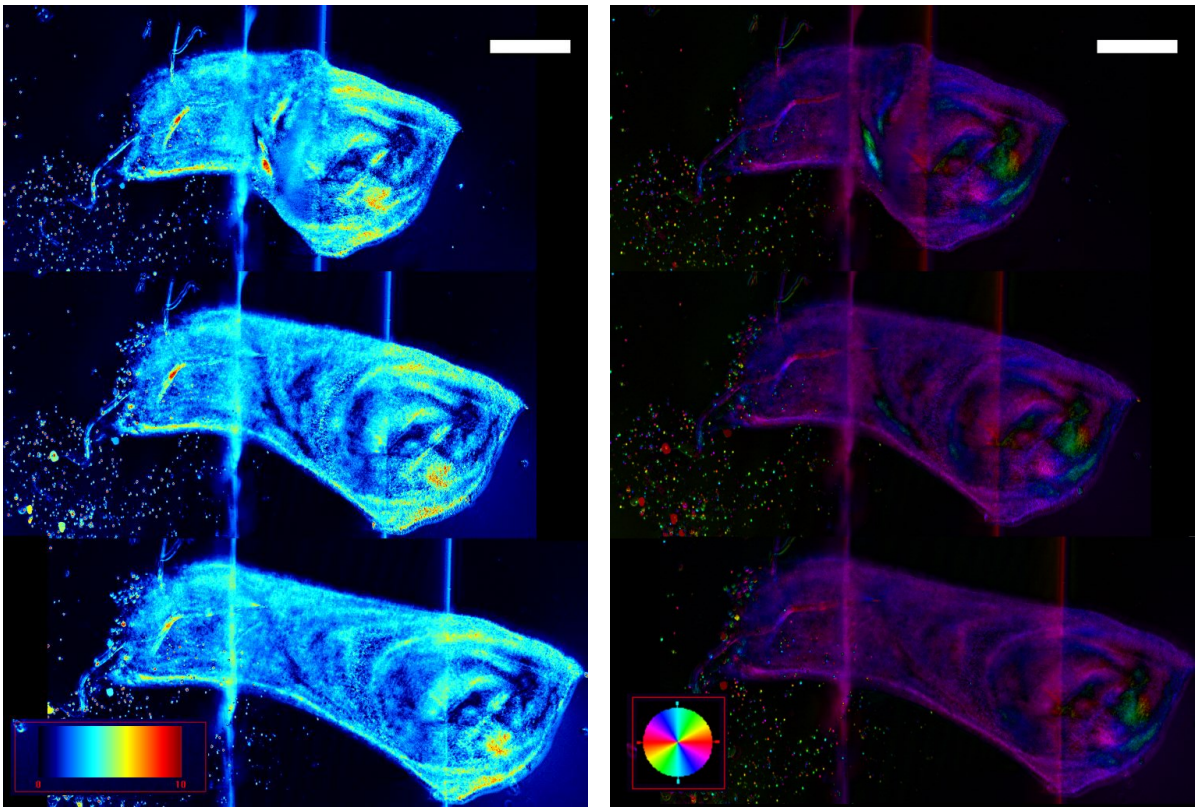

Figure 3.10 – Heat-maps of the spatial retardance distribution R (**left**) and the orientation of the slow axis ϕ (**right**) of a wing imaginal disc at different stages of stretching. The measured retardances range from 0 nm (black) to 10 nm (red). The orientations (the azimuth between the slow axis and the $x-$axis) ranges from 0° (red-purple) to 180° (orange-red). In the top figure the wing imaginal disc is compressed by a force of -144 ± 13 µN, in the middle panel the disc is in its initial state at a force of ± 4 µN, while in the bottom figure the wing imaginal disc is stretched by a force of 156 ± 14 µN. When comparing the top figure to the middle and bottom figures an unambiguous change of R and ϕ becomes visible in between the two glass slides. The depicted raw data belongs to sample 3 as referred to in figure 3.13 and figure 3.14. The scale bars equal 100 µm.

Inserting the transversal stress component $\sigma_{y,i} = \sigma_{y,0} - \nu\sigma_{x,i}$ and $F_0 = 0$ the relation becomes

$$\begin{aligned}
\frac{R_i}{h_i} - \frac{R_0}{h_0} &= C\ (\sigma_{x,i} + \nu_i\sigma_{x,i} - \sigma_{x,0}) \\
\frac{R_i}{h_i} - \frac{R_0}{h_0} &= C\ \left(\frac{F_i}{w_i\ h_i}\ (1+\nu_i) - \frac{F_0}{w_0\ h_0}\right) \\
\frac{R_i}{h_i} - \frac{R_0}{h_0} &= C\ \left(\frac{F_i}{w_i\ h_i}\ (1+\nu_i)\right)
\end{aligned}$$

In all conducted birefringence measurements the samples were illuminated perpendicularly to their basal-apical sides and thus the length of the optical path, i.e. the physical length the light traversed, equals the height of the wing imaginal disc. For the wing pouch the height corresponds to its thickness, but it does not for the hinge-notum region due to its buckled topology. As mentioned above the thickness of the wing pouch and the height of the buckled hinge-notum region can be considered roughly equal. The optical length traversed by the light is therefore in the same range and thus can be treated equally for all stress-birefringence measurements. The same assumption was made by [16] and in contrary to the stress-strain measurements described in section 3.3 the stress-birefringence measurements do not indicate any influence of a difference in thickness.

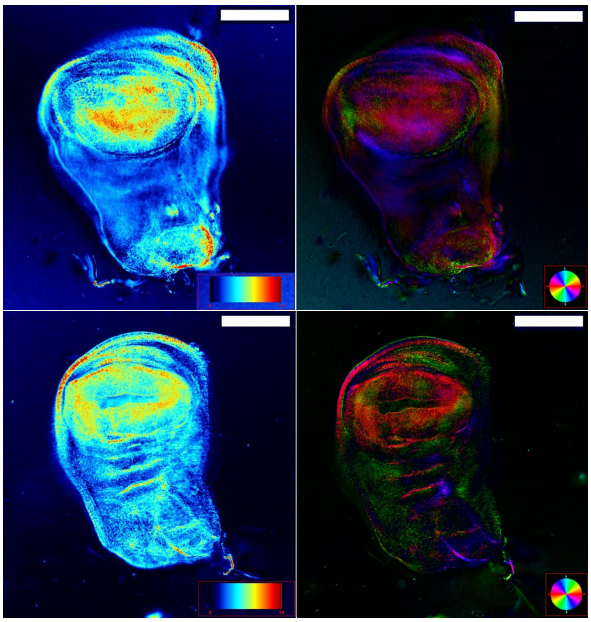

Figure 3.11 – Retardance and azimuth heat-maps for mechanical unperturbed wing imaginal discs. The measured retardances range from 0 nm (black) to 10 nm (red) in the top figure and from 0 nm (black) to 7.76 nm (red) in the bottom figure. The average retardance within the wing pouch was about 4.5(1) nm (top) and 4.7(1) nm (bottom). For the hinge-notum region the retardance was 2.0(1) nm (top) and 2.8(1) nm (bottom). The corresponding stresses are listed in table 3.6. Scale bars equal 100 µm.

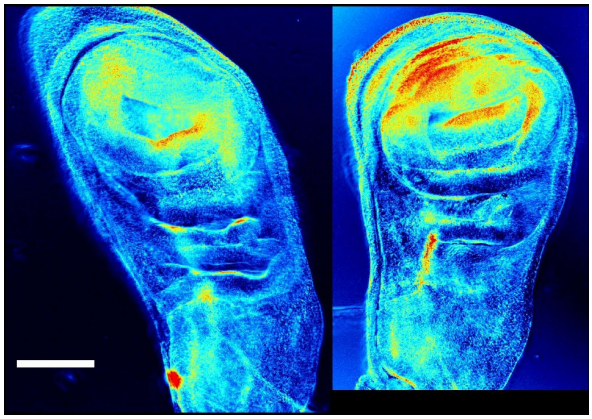

Figure 3.12 – Retardance maps of a single wing imaginal disc. On the right side the sample is seen in its unperturbed state and on the left side it is stretched by hand about 30%. The average retardance within the wing pouch of the elongated wing imaginal disc drops from 3.1(1) nm to 1.8(1) nm and persist for the hinge-notum region at 1.0(1) nm. The measured retardance ranges from 0 nm (black) to 10 nm (red). The corresponding stresses are listed in table 3.6 The scale bar equals 100 µm.

Furthermore, the optical paths show a similar behavior in the sense, that they decrease during the stretching experiments, although for different reasons. The optical path of the wing pouch decreases due to the constriction of the thickness, while the optical path of the hinge-notum region mainly decreases due to the unfolding of the tissue. The reduction in height at step i was taken into account and described by $h_i = h_0\ (1 - \nu_i \varepsilon_{x,i})$, which lead to

$$\frac{R_i}{h_0(1-\nu_i\varepsilon_{x,i})} - \frac{R_0}{h_0} = C\ \left(\frac{F_i(1+\nu_i)}{w_i\ h_0(1-\nu_i\varepsilon_{x,i})}\right).$$

The initial height h_0 cancels and the photo-elastic constant can be retrieved by

$$C = \frac{(R_i - (1-\nu_i\varepsilon_{x,i})\ R_0)\ w_i}{F_i\ (1+\nu_i)}. \tag{3.10}$$

The stress-birefringence measurements were sensitive to the samples preceded mechanical treatment. Samples, which had been loosely attached to a cover slip without further mechanical perturbation or treatment, for instance by repositioning on the sample carrier, exhibited retardance distributions, which correlated to stress-distributions as proposed by the growth model of Aegerter-Wilmsen et al. [13, 15]. In figure 3.11 retardance and orientation heat-maps of two unperturbed wing imaginal discs are given. For both samples a high retardance distribution was found in the wing pouch with an average retardance of 4.5(1) nm (top figure) and 4.7(1) nm (bottom figure), respectively peak values of 7.8 nm and 10 nm. In contrast to the wing pouch the average retardances of the hinge-notum region is in the order

of 2.0(1) nm (top figure) and 2.8(1) nm (bottom figure). The orientation of the slow axis were found circumferentially changing in the wing pouch and randomly distributed in the hinge-notum region and thus as expected by the growth model. As already pointed out by Nienhaus et al. [16] the high retardance distribution in the wing pouch must decrease for significant tensile stresses if the retardance results from compressional stresses. To test this assumption Nienhaus et al. elongated wing imaginal discs manually about 30% and observed significant reductions in retardance, which could not solely be explained by a reduction in sample height. A repetition of this experiment is shown in figure 3.12 and lead to a similar result with a decrease in peak retardance of $\sim 3\,\mathrm{nm}$ for a strain of ~ 0.25. The average retardance of the wing pouch decreased about 1.4(1) nm. Compared to these unperturbed samples the wing imaginal discs mounted on the stretching setup showed a much lower initial retardance R_0 and more oriented along the direction of force.
Figure 3.13 depicts the changes in mean retardances due to the induced planar stresses for six different samples. The curves were normalized to the initial retardances of each sample. Similarly, figure 3.14 shows the changes of mean orientations due to the applied stresses. The intial retardances R_0 and orientations ϕ are listed in the figures caption and range from $0.35 - 2.9\,\mathrm{nm}$, respectively from $30 - 70°$. The samples can roughly be grouped by the courses of $\Delta R(\sigma_x)$. Samples (1,2,3) show a clear decrease in retardance for tensional stresses in contrast to sample (4,5,6), which – aside the hinge-notum region of sample 4 – show an increase for tensional stresses. Besides the unconnected data points of diagram 5 the maximal change in retardance for the samples (4,5,6) was only in the order of $\sim 0.2\,\mathrm{nm}$, whereas the change in retardance for the samples (1,2,3) is in the order of $\sim 0.5\,\mathrm{nm}$. The unconnected data points of diagram 5 ranging between 0.5 nm and 0.9 nm had been retrieved after a full relaxation of the wing imaginal disc. It seems as if this relaxation step had some influence on the tissue, which is why these points are considered as outliers. In contrast to the stess-strain curves in section 3.3 the retardance and azimuth measurements did not reveal any systematic change at $\varepsilon_x \sim 0.25$, respectively $\sigma(\varepsilon_x \sim 0.25)$. This can be seen as an indication that for stress-birefringence not the thickness was relevant, but its height, i.e. the optical length traversed by the light. Furthermore the factors $(1 - \nu_i \varepsilon_{x,i})$ and $(1 - \nu_i \varepsilon_{x,i})$ used to weight ΔR in equation 3.10 was not found to play a decisive role in the course and behavior of $\Delta R(\sigma_x)$.
Although samples (1,2,3) show a decrease in retardance for externally applied tensile stresses, solely sample one fully support the assumption of the growth model. According to the model and the results of the birefringence measurements of the unperturbed wing imaginal disc (see 3.11) tensile stress should mainly reduce the retardance in the wing pouch and less in the hinge-notum region. In sample 1 the retardance raised again for higher stresses and is probably related to an accumulation of tensile stresses after the initial compressional stresses had been released. However, in sample (2,3) a raise in retardance was not observed for higher stresses, but then in contrast to sample 1 the behavior of ΔR for the regions of these samples did not differ either. Further evidence for accumulation of tensile stress is the increase in retardance in samples (4,5,6). The different observed behaviors of the two set of samples can be related to the preceded mechanical treatment during installation. Samples (4,5,6) were detached and attached at least once for necessary repositioning on the setup, while samples (1,2,3) could be installed without repositioning. Nevertheless most of the samples $(2 - 6)$ needed to be slightly pressed on the Poly-l-lisine coated surface to increase cohesion. The mechanical treatment of samples (4,5,6) probably lead to an relaxation of compressional stresses, such that these samples could accumulate tensional stresses from the very beginning of experiment. It is very likely, that the relaxation was not realized by cell-rearrangements, because no cell-rearrangements could be observed at any time during the stretching experiments described in chapter 4, in which cellular resolution had been available.
Although the behavior in change of retardance $\Delta R(\sigma_x)$ of the six presented samples differ widely, the behavior in their mean orientations $\Delta\phi(\sigma_x)$ are similar. With increasing stresses the azimuth increases and finally reaches absolute values between approximately 110° to 160°.

	wing pouch	hinge-notum region	wing disc total
sample	$[10^{-10}\,\mathrm{Pa}^{-1}]$	$[10^{-10}\,\mathrm{Pa}^{-1}]$	$[10^{-10}\,\mathrm{Pa}^{-1}]$
2.5(5)	2.09(5)	2.0(5)	
1.5(7)	1.2(8)	0.9(8)	
1.6(5)	1.3(6)	2.5(5)	
1.5(6)	1.0(4)	1.3(5)	
2.2(9)	2.2(12)	1.7(8)	
2.9(9)	3.1(7)	3.2(8)	
mean	2.0(7)	1.8(7)	1.9(7)

Table 3.5 – Average photo-elastic constants C of all samples for the wing pouch, the hinge-notum region and the entire wing disc tissue. The constants of the different samples are all in the same order of magnitude.

	$\varepsilon_x = 0$		$\varepsilon_x \sim 0.30$	
	σ_p	σ_{hn}	σ_p	σ_{hn}
sample	$[10^5\,\mathrm{Pa}]$	$[10^5\,\mathrm{Pa}]$	$[10^5\,\mathrm{Pa}]$	$[10^5\,\mathrm{Pa}]$
1	3.4(1)	1.7(1)		
2	3.3(1)	1.6(1)		
3	3.6(1)	1.5(1)	1.7(1)	1.3(1)
mean	3.4(1)	1.6(1)		

Table 3.6 – Average stresses for the wing pouch and hinge-notum region in the three unperturbed wing imaginal discs shown in figure 3.11 (top: sample 1, bottom: sample 2) and figure 3.12 (sample 3). The average stress was calculated using a global value for the photo-elastic constant of $C = 1.9(3) \cdot 10^{-10}\,\mathrm{Pa}^{-1}$ and a tissue height of $h = 45\,\mu\mathrm{m}$. The stresses in the elongated sample were calculated weighting the tissue height with $(1 - \nu\varepsilon_x) = (1 - \varepsilon_y)$. Longitudinal strain was $\varepsilon_x \sim 0.30$ and transversal strain was $\varepsilon_x \sim 0.15$.

Finally, the stress-birefringence measurements were used to determine the average photo-elastic constant C for the wing pouch, the hinge-notum region and the tissue in total deploying equation 3.10. The results for C are listed in table 3.5 and although the six samples differ greatly in $\Delta R(\sigma_x)$, the determined optical-stress coefficients are all in the same order of magnitude. The average stresses in the different areas of the unperturbed wing imaginal discs, which are shown in figure 3.11, were determined using the mean photo-elastic constant $C = 1.9(7) \cdot 10^{-10}\,\mathrm{Pa}^{-1}$ and the average tissue height $h = 45\,\mu\mathrm{m}$. The same values were used to specify the average stresses of the unperturbed wing imaginal disc, which is shown on the right side of figure 3.12. For the elongated state of this sample (shown on the left of figure 3.12) the height was weighted by $(1 - \nu\varepsilon_x)$ to take the reduction in height into account. The results are listed in table 3.6.
In late third instar wing imaginal discs the average stress in the wing pouch is in the order of $10^5\,\mathrm{Pa}$ and about two times higher than the stress found in the hinge-notum region. Moreover, the observed reduction in stress $\Delta\sigma = 1.9(2) \cdot 10^5\,\mathrm{Pa}$ within the wing pouch of the elongated sample shown in figure 3.12 is in compliance with the applied stress

$$\sigma_x = E\varepsilon_x = 1.2(4) \cdot 10^5\,\mathrm{Pa}\ \cdot 1.30(2) = 1.6(4)\,\mathrm{Pa},$$

which was calculated using the Young's modulus that was determined in section 3.3.

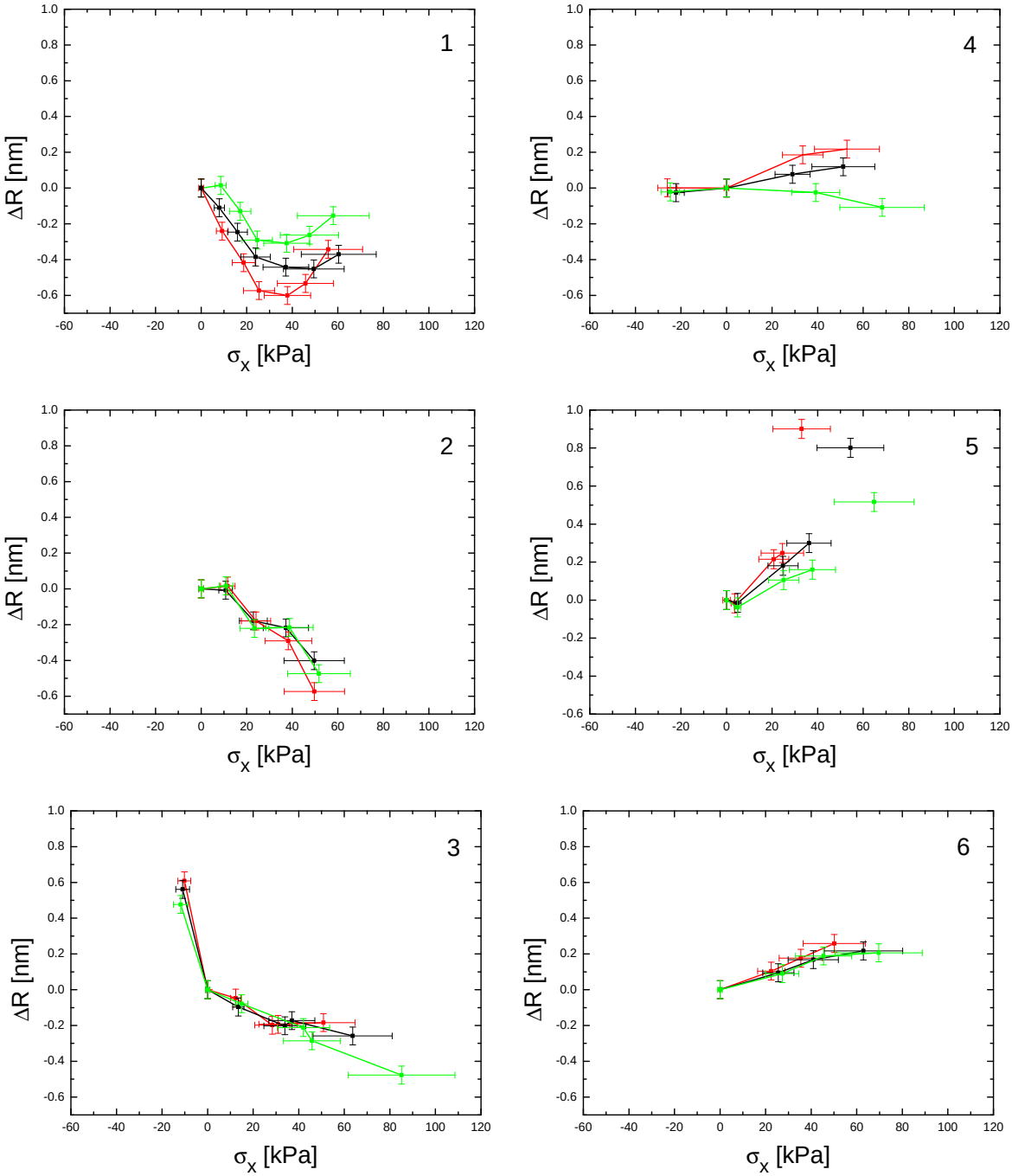

Figure 3.13 – The changes in retardance due to externally induced planar stresses are shown for six different samples. In red ΔR for the wing pouch, in green for the hinge-notum region and in black for the wing imaginal disc in total are shown. Retardances of the samples initial states R_0 were as following (wing pouch/hinge-notum/total): 1 – (1.8(1)/2.0(1)/2.2(1)) nm; 2 – (0.54(6)/0.34(6)/0.37(6)) nm; 3 – (2.8(1)/2.9(1)/2.9(1)) nm; 4 – (0.78(6)/0.60(6)/0.71(6)) nm; 5 – (0.78(6)/0.54(6)/0.54(6)) nm; 6 – (0.41(6)/0.20(6)/0.31(6)) nm.

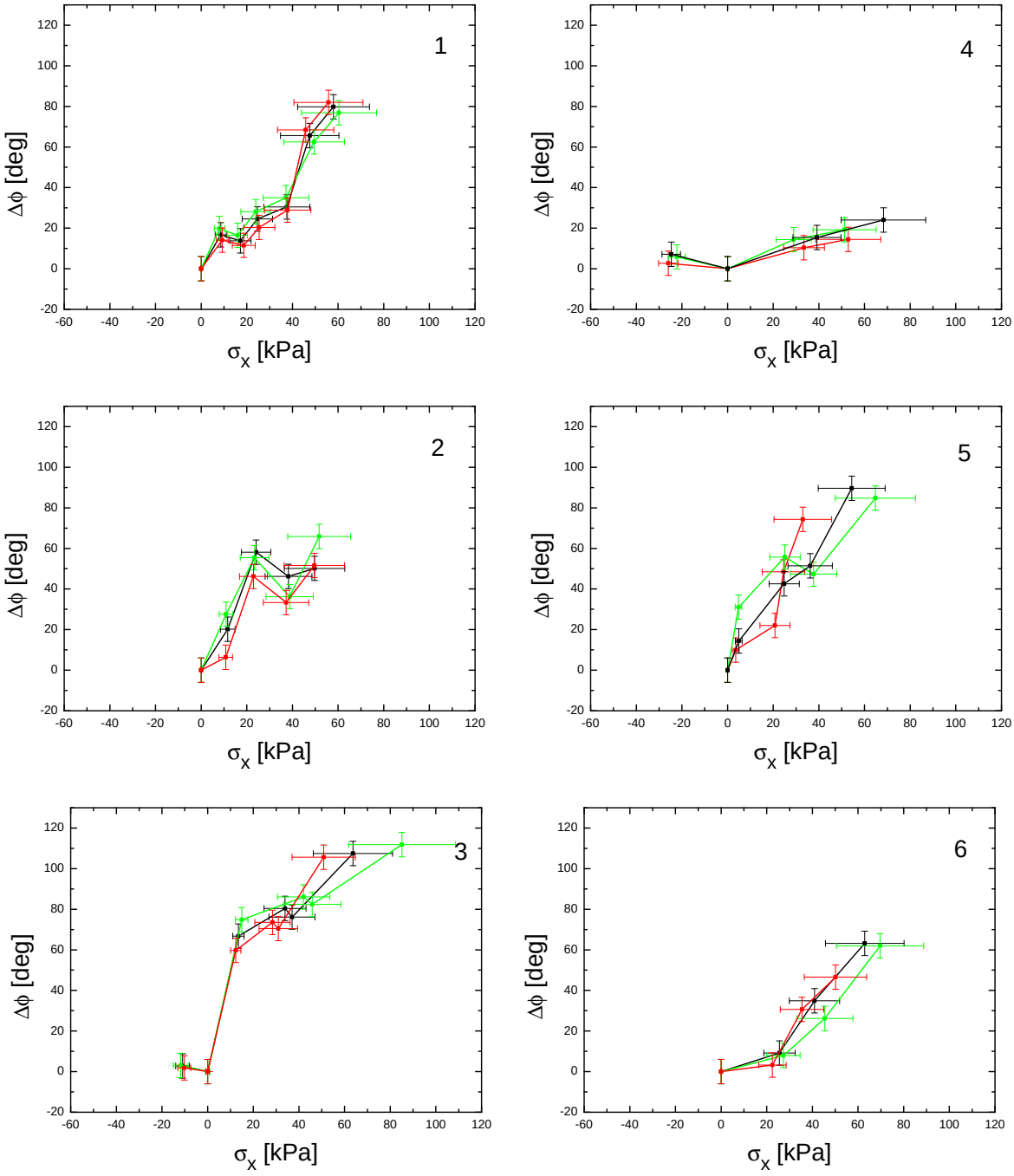

Figure 3.14 – The changes in orientation due to externally induced planar stresses are shown for six samples. In red $\Delta\phi$ for the wing pouch, in green for the hinge-notum region and in black for the wing imaginal disc in total are shown. The azimuth of the samples initial states ϕ were as following (wing pouch/hinge-notum/total): 1 – (75/81/79)°; 2 – (54/55/57)°; 3 – (27/22/25)°; 4 – (74/95/84)°; 5 – (23/27/24)°; 6 – (43/58/56)°. Uncertainties were all ±4°.

3.5 Dynamical Response of the Wing Imaginal Disc

In all previous sections samples were stretched in a stepwise manner and while keeping under constant stress their responses either in strain or stress were measured. This experimental approach allowed to investigate the wing imaginal discs in mechanical equilibrium and to determine its elastic properties. However, this approach is not feasible to study time-dependent responses, for instance its viscoelasticity. The experimental procedure was therefore modified and instead of applying forces in discrete steps and monitor the mechanical responses of the tissue in equilibrium, the applied force was increased linearly and monotonically over time. The tissue's behavior was documented by concurrent video recording, which then was split into single pictures constructing a timeline. For each point in time the length L of the total wing imaginal discs was extracted.
The main focus of the following studies based on the tissue's behavior for a sudden change in stress and on the time scale the tissue reacts.
The applied load was continuously increased by driving the piezo-stage that was used to deflect the cantilever beam with a constant velocity v_b, such that the force increased linearly over time.
The applied force $F(t)$ thus becomes:

$$F(t) = D\ v_b\ t, \tag{3.11}$$

wherein D is the spring constant of the cantilever beam defined in equation 2.7. The wing imaginal disc elongates over time with increasing force until the cohesion between the wing imaginal tissue and the glass surface becomes smaller than the applied force. At this point the tissue loosens and relaxes exponentially.
In order to model the wing imaginal disc, the tissue was considered as a damped system composed of a spring with spring constant k and a dashpot[7] of friction f in parallel. The constitutive equation without any external forces $t > t_l$ is

$$0 = k\Delta L + f\dot{\Delta L}. \tag{3.12}$$

Rewriting equation 3.12 using

$$\tau = \frac{f}{k} \tag{3.13}$$

the solution becomes

$$\Delta L(t) = \Delta L_0(t_l)\ \exp\left(-\frac{t - t_l}{\tau}\right). \tag{3.14}$$

For times $0 < t < t_l$ when external forces $F(t) = D\ v_b\ t$ are exceeded on the sample the constitutive equation is

$$D\ v_b\ t = k\Delta L + f\dot{\Delta L}, \tag{3.15}$$

respectively

$$\frac{D\ v_b}{k} = v + \tau\dot{v} \tag{3.16}$$

This equation in velocities can be solved using the variation of parameters method in combination with the boundary condition $v(0) = 0$. The solution is then

$$v(t) = \frac{D\ v_b}{k}\left(1 - \exp(-t/\tau)\right) \tag{3.17}$$

and the change in length ΔL can be calculated by integrating over $[0, t]$.
Using the abbreviation

$$Z = \frac{D\ v_b}{k}, \tag{3.18}$$

the solution for the extension is

$$\Delta L = Z\left(t + \tau(\exp(-t/\tau) - 1)\right). \tag{3.19}$$

[7] A dashpot is an idealized purely viscous unit, i.e. a mechanical resistance, which is linearly proportional to the experienced velocity.

Thus for the times $0 < t < t_l$ the change in length due to a linearly increasing external force is a superposition of two functions. The exponential term $\tau(\exp(-t/\tau)$ dominates at first and damps and delays the tissue's reaction on the externally applied forces due to inner friction. For bigger times the linear term dominates the mechanical response ΔL, which then follows the force delayed by the specific time τ.
In rheology this model of viscoelastic behavior is referred to as a Kelvin-Voigt material which is described by the constitutive relation

$$\sigma(t) = E\varepsilon(t) + \eta\dot{\varepsilon}(t). \tag{3.20}$$

In this case the specific time is defined similarly by the dynamic viscosity and the Young's modulus of the material, i.e. $\tau = \eta/E$. More details about rheologic models can be found in [174, 175].

The dynamic responses of twelve samples were analyzed to determine the effective spring constants k and time constants τ, from which the corresponding viscous damping coefficients f were calculated. First, for the time before detachment the extensions of the wing imaginal discs were linearly approximated. The slopes Z of the regression lines then allowed to determine the samples' spring constants k. Second, the time constants τ were extracted. This can either be done by shifting the regression line to the start of the experiment or by plotting the relaxation in elongation after the detachment of the tissue in a log-linear graph and perform a linear regression. The uncertainty in time due to the average maximal frame rate of the video recordings made method one very error prone, which is why method two was preferred. The maximal frame rate was at 1/3 Hz and thus estimated to be in the order of $\sim 3\,\mathrm{s}$.
In figure 3.15 raw and preprocessed data of two time-course measurements are shown representing typically dynamic responses of the wing pouch, hinge-notum region and the wing imaginal disc in total. All areas respond concurrently to the external perturbation, i.e. the start of change in length coincide. Furthermore all areas extend linearly in time before the tissue detaches and their slopes are according to equation 3.18 proportional to the inverse of their spring constants k, which in turn depend on their initial lengths.[8] Consistent with these considerations the lengths of the samples wing pouch and hinge-notum region differ as much as their spring constants. For the samples shown in figure 3.15 the relative difference was in the order of 10%. The sum of the slopes $Z_p + Z_{hn}$ was equal to the slope of the total area Z_t, which subsequently gives the relation for the effective spring constant of two springs in series, namely $k_t^{-1} = k_p^{-1} + k_{hn}^{-1}$. The thereby determined averaged total spring constant is consistent with the average values already found in chapter 3.1 and the strains of the different areas are equal within their uncertainties $\varepsilon_t = \varepsilon_p = \varepsilon_{hn}$. After the detachment of the tissue the wing pouch, the hinge-notum region and the total wing imaginal disc relaxed on equal time scales τ.
The main focus in this work was set to the question how the wing imaginal disc responses dynamically on external forces and on what time scale it responses. Figure 3.15 presents two of three samples, which were analyzed for their dynamic responses in respect to their wing pouch, hinge-notum region and overall tissue. It was found that an analysis of the partial areas does not yield any deeper insights regarding to the wing imaginal discs dynamic response on external forces. The results of the analysis are listed in table 3.7.

The constitutive equations 3.12 and 3.15 describe a damped oscillator characterized by its damping coefficient τ. In this description the wing imaginal disc acts like a mechanical low-pass-filter. This means that an external force or stress must act long enough upon the tissue to be internalized. The average decay time of the tissue is $\tau = 12(3)\,\mathrm{s}$ or about $0.1(3)\,\mathrm{Hz}$. A feeding larva contracts on average every second and therefore the precursor organ of the wing is exposed to a pulsing external forces of about 1 Hz.
Thus an effect of the larva's peristaltic contraction on the growth regulation of the wing imaginal disc can be excluded. On the time scales of a cell-cycle, i.e. several minutes, the tissue behaves elastic. If the time constant τ were in the same range of time mitosis takes place, the viscous behavior would dominate and stress could not built up by mitosis.

[8] The possible influence of varying elastic moduli was ruled out by the findings in section 3.3.

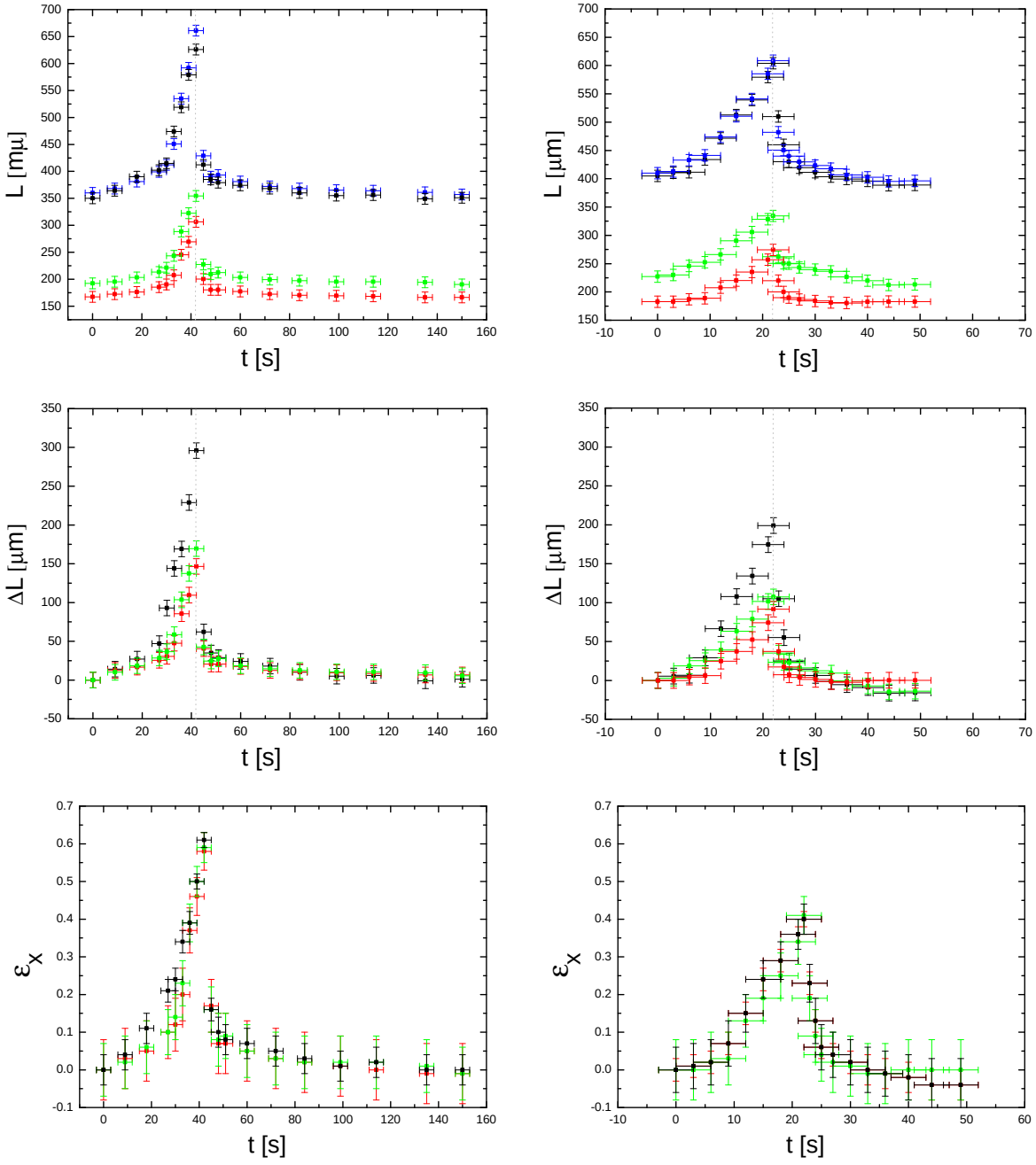

Figure 3.15 – Raw and preprocessed data of two typical time-course experiments. The left column relates to sample 7, the right column to sample 8 as listed in table 3.7. The top row of diagrams shows the absolute length L of the wing pouch (red), the hinge-notum region (green), the disc in total (black) and the sum (blue) of the wing pouch and hinge-notum region's lengths. The middle row depicts the changes in lengths ΔL while in the bottom row the corresponding longitudinal strains ε_x are plotted.

sample	$Z = (v_b \cdot D)/(k_t)$	k_t	τ	f
	[µm/s]	[N/m]	[s]	[Ns/m]
1	7.2(1)	0.57(1)	4(3)	2(2)
	6.2(3)	0.66(3)	5(3)	3(2)
2	7.2(2)	0.57(2)	3(3)	2(2)
3	5.7(3)	0.72(4)	7(3)	5(2)
4	4.3(3)	0.95(7)	7(3)	7(3)
5	8.3(7)	0.49(4)	20(3)	10(2)
	9.7(3)	0.42(1)	25(3)	11(1)
6	5.0(7)	0.8(1)	23(3)	19(4)
	4.3(2)	0.95(5)	18(3)	17(3)
7	3.1(2)	1.32(9)	17(3)	22(4)
	3.0(3)	1.4(1)	12(3)	16(4)
8	6.4(1)	0.64(1)	9(5)	6(3)
	5.7(3)	0.72(4)	9(3)	6(2)
9	5.0(2)	0.82(4)	12(3)	10(3)
	6.0(2)	0.7(1)	12(3)	4(2)
10	6.0(2)	0.68(8)	4(3)	3(2)
	5.5(6)	0.75(8)	6(3)	9(2)
11	3.0(5)	1.4(2)	24(4)	33(8)
12	3.0(3)	1.4(1)	9(5)	12(7)
13			15(2)	
14			18(1)	
15			6(1)	
16			15(2)	
mean	5.5(4)	0.8(1)	12(3)	10(3)

Table 3.7 – Results of the dynamic response measurements. For $N = 12$ samples the slope Z, the total spring constant k_t, viscous damping coefficient f and the dynamic response time τ were determined. For four further samples only the dynamic response times could be determined as the video recording was started too late. The average velocity of deflection for each measurement was $v_b = 16.2(2)$ µm/s and the spring constant of the cantilever beam was $D = 0.253(7)$ N/m (setup configuration I).

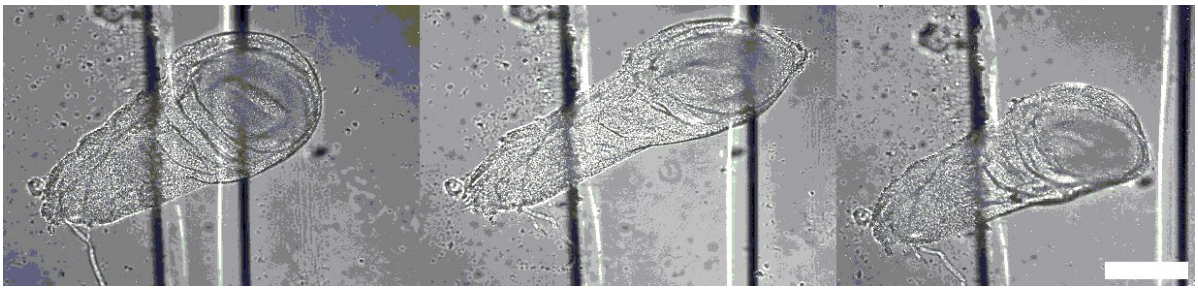

Figure 3.16 – Three pictures of a time-course experiment. The left figure shows the disc in its initial state before any forces were applied, the middle figure was taken during the course of the experiment and the right figure after loosening and full relaxation into its initial form and shape. This kind of elastic behavior was observed for all healthy samples, that did not show any sign of deterioration. Scale bar equals 100 µm.

In figure 3.16 three frames of such an time-course experiment are presented as an example of the high elasticity observed. After detachment the tissue fully relaxed to its original form and size. Wing imaginal discs did not show any considerable plasticity if kept under appropriate conditions. Wing imaginal discs, which had been kept in culture medium, preserved their complete elasticity for more than an hour. Some samples, which were only kept in phosphate buffered solution, even maintained their full elastic behavior for such a timespan. However such cultured discs seemed to start wearing out and loosing their elasticity after $90 - 120$ min. No systematic experiments had been performed on this issue, such that only the hypothesis can be raised, that the wing imaginal discs elasticity is a characteristic of its health and liveliness. Supporting evidence for this hypothesis was found in two major observations of plasticity, or to be more precise, loss of elasticity. One of these observations was unintended and coincidental, the second observation was intended. The observations can be found in figures 3.17 and 3.18. On the wing imaginal disc in figure 3.17 stress-birefringence measurements were performed as it was referred to in section 3.4 (sample 3). After finishing all stress-birefringence measurements within an hour the tissue was further kept in phosphate-buffered solution. A last stretching step was applied during which an unfamiliar behavior was observed. The tissue seemed to break on its edges; parts within the sample started to rearrange. The first and second retardance maps (from the top) equal the retardance measurements shown in 3.10, while the third and fourth image shows the disc in a state of being overstretched resulting in a plastic deformation. Note, that the other samples in good culture conditions and which were dissected freshly, did withstand even higher stresses and strains without plastic deformation.
In order to gather more evidence for the hypothesis that the elasticity of the wing imaginal disc is a property, which is strongly bound to the health of the organ, a sample was killed in ethanol after successful stress-strain measurements. A selection of the experiment's images are depictecd in figure 3.18. The upper four images (A – D) show how the sample was stretched from its initial state to maximal extension, release and another ensuing extension. Each time the wing imaginal disc relaxed completely. When the disc was finally flooding with ethanol (image E) in a high extended position, the tissue lost its elasticity and when releasing the applied force, the sample (F) arched downwards to compensate for its length. When the sample was pulled further until it detached, it also kept its form and did not relax at all. These observations do not give any insights on the mechanisms of the organs elasticity, but indicate that it is an actively preserved property by the wing imaginal disc. Further evidence is the observation of an insignificant mechanical hysteresis and the absence of creep and stress-relaxation.

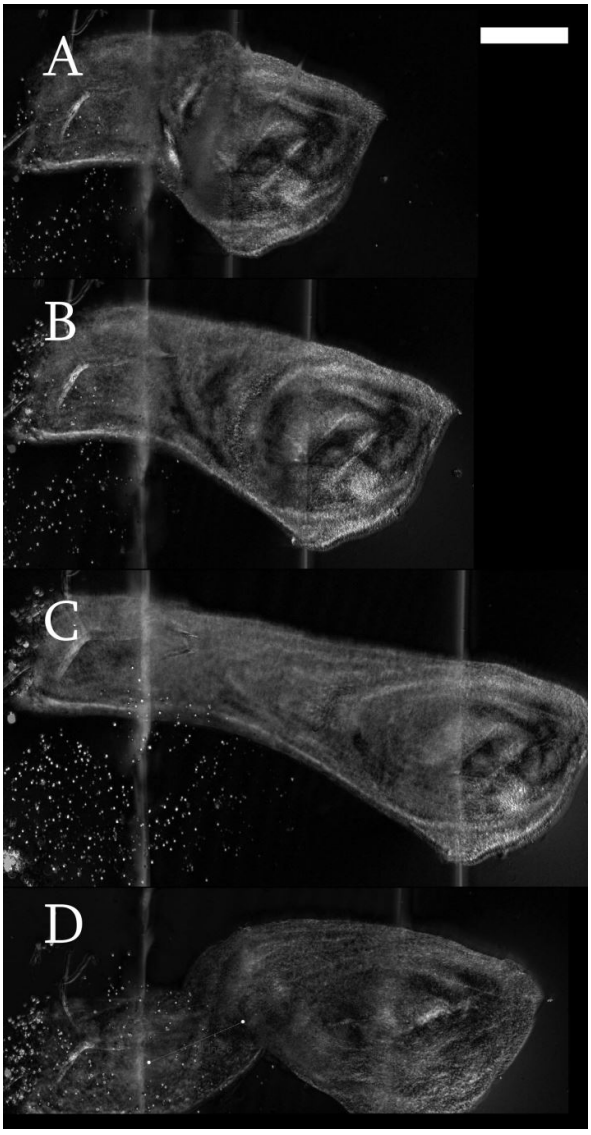

Figure 3.17 – A wing imaginal disc that was left in PBS after regular stress-birefringence experiments (A,B). After a few hours the sample was stretched further (C). During the elongation of the wing imaginal disc a break in the tissue's border was observed followed by a rearrangement within the tissue (C). When releasing some stress the disc did not relax as normally observed, but buckeled (D). Scale bar equals 100 µm.

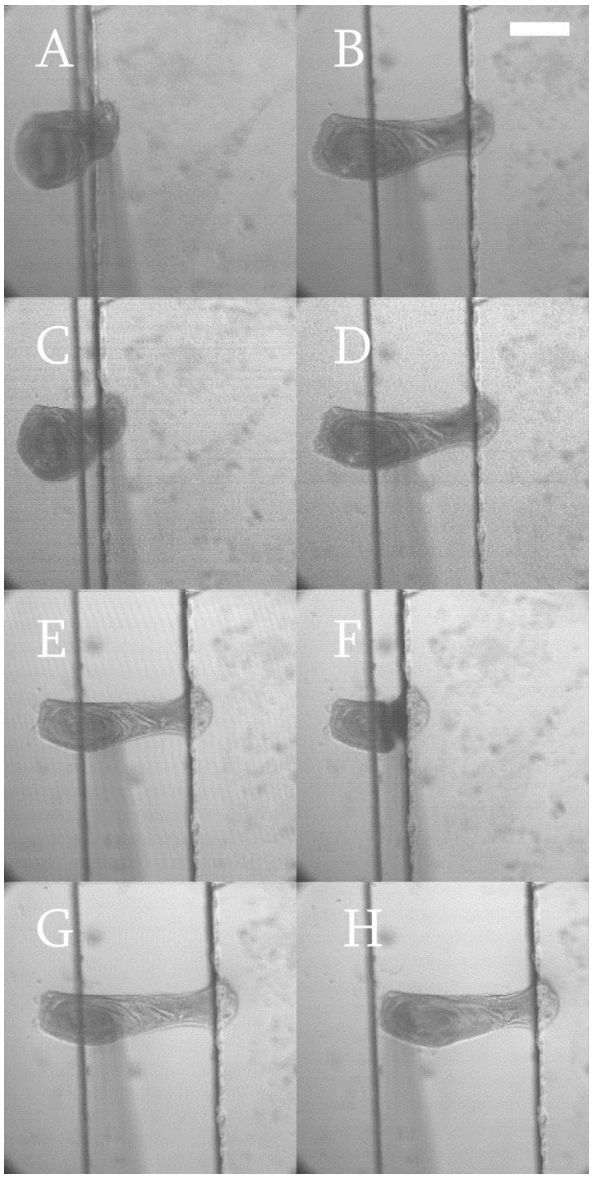

Figure 3.18 – A wing imaginal disc was stretched and released several times (images A – D) and then flooded with ethanol (E). After being flooded the tissue could not compensate for the shortening in length and arched downwards between the glass slides (F). The sample was then stretched again and unfolded (G) and finally detached (H). Note, that the wing imaginal disc did not change its shape in any form since flooded with ethanol. Scale bar equals 200 µm.

4 Mechanical Regulation of Growth

In the previous sections the wing imaginal tissue was characterized in its mechanical properties to scrutinize the first basic assumption of the mechanical growth model [13, 14, 15], which proclaims the accumulation of stresses within the tissue due to growth. The highly linear elastic behavior of the wing imaginal tissue described in section 3 in combination with the findings of other works supports this assumption.[1]

The second basic assumption of the model is the regulation of proliferation by mechanical stress, which explains the occurrence of spatially uniform proliferation and the cessation of growth. Most research on the mechano-regulation were performed on mammalian cell cultures, which showed a clear relation between the stress cells experience and their proliferation. Early works already showed an increase in proliferation upon the application of mechanical tension [176, 62] and in more recent works the proliferation of cancerous cells was down regulated enclosing them in spheres and thereby pressurize them [63]. Furthermore the mechanical regulation found in mammalian tissue cultures was related to biochemical pathways in the wing imaginal disc [177]. However, a direct regulatory effect of mechanical forces on cell proliferation in developing epithelial tissue was still not proven.

Here, the assumption of a promoting effect of tensile stresses was experimentally tested by stretching late third instar wing imaginal discs and concurrently determining their proliferation rates. This was realized using the home-built pulling setup with the fluorescent confocal microscope Leica SP1. The samples cell membranes were labeled with a yellow fluorescent protein (Lac-YFP [160]) and thereby allowed the observation of individual cells and thus mitotic cells of the wing pouch over time. During mitosis cells increase their apical cell area more than five fold relative to surrounding non-mitotic cells and thus can be clearly identified. Figure 4.1 shows an example for the increase in apical area.

Each sample was dissected and kept in phosphate-buffered solution (PBS) upon their installation on the stretching setup; a $10X$ objective was used for the installation of the wing imaginal discs, while a $40X$ oil-immersion objective was used for the actual measurement and acquisition of data. Due to the short working distance of this objective setup variation B shown in figure 2.1 had to be used.

The wing imaginal discs basal-ventral side was attached to the non-movable cover slip while its basal-dorsal side was attached to the free movable glass slip. Immediately after preparation and installation on the setup the PBS was removed via suction and replaced with Clone8 medium [155]. The time needed for dissecting the wing imaginal disc, installation on the pulling setup and exchanging the media took in total about 10 min. From then on the culture medium was exchanged every 20 min to 30 min for the whole course of the experiment.

The sample was either stretched by an external force of 160(9) µN or 350(15) µN and kept under the given load for the entire course of the experiment. Another set of samples, which served as control measurements, was equally prepared and installed, but left unstretched.

For experimental times less than 60 min a change in shape or form of the investigated wing imaginal disc was never observed and samples could still be induced to evaginate upon treatment with ecdyson.[2] Thus to ensure working with living tissue the duration of each experiment was restricted to $\Delta t = 60\,\text{min}$. To monitor the imaginal tissues temporal reaction on externally induced stress every $t_s = 6\,\text{min}$ a $z-$stacks was made. In [110] Gibson et al. found mitosis to endure 20 min to 30 min depending on the environmental temperature, such the proper sampling time could be estimated using the Nyquist and Shannons sampling-theorem [178]. With the maximal cell division frequency of $(20\,\text{min})^{-1}$, the

[1] These works were already referred to and elaborated in greater detail in section 1.5.5 and the beginning of section 2.

[2] Ecdyson is a steroidal hormone and induces the molting and pupation of the larva in conjunction with juvenile hormones. It also triggerst metarmorphosis to the imago.

sampling time should be at least $t_s = 10\,\text{min}$ or below. The sampling time, respectively the time between to consecutive $z-$stacks, was thus chosen to $t_s = 6\,\text{min}$ to be able to identify possible rapid changes in proliferation rate. In each case a $z-$stack of the unstretched wing pouch was made directly after the installation of the sample to obtain the initial present (mitotic) cells. The acquired stacks were analyzed in *ImageJ* layer-by-layer with regard to the observable mitotic cells. This was necessary to compensate for the curvature of the tissue and the deep localization of the used marker, which labels about one third of the cells membrane at the apical side. Consequently in projection of some $z-$stacks some single mitotic cells became concealed due to the additional fluorescent signal coming from several stack layers making some regions of the projective image appear slightly blurred.
The proliferation rate was calculated using [81]

$$g(t) = \frac{\mathrm{d}\ln(N(t))}{\mathrm{d}t} \approx \frac{\Delta N}{N(t)\Delta t} \tag{4.1}$$

by counting and tracing the number of newly dividing cells as well as cells finishing division.[3] The approximation $\Delta\ln(N) \approx \Delta N/N$ is valid as long the additional cells ΔN during the time $\Delta t = 60\,\text{min}$ is small compared to the initial amount of cells N. This holds true for the conducted experiments as the total number of cells in the field of view was between $N = 1600$ and $N = 2000$ and the number of newly added cells was between $\Delta N = 15$ and $\Delta N = 65$.
The samples were illuminated with 473 nm monochromatic light, which was damped to less than 0.1 mW to reduce bleaching and photo-toxicity to a minimum. This resulted in a low signal-to-noise ratio, which made the identification of mitotic cells in some cases and especially at the edges of the wing pouch ambiguous. The uncertainty in cell number was estimated to be between one and two cells and equals to a relative uncertainty of less than 5%, which is smaller than the variation in cell number between different samples.
In the previous sections a linear relation between the tissues stress and strain was found, such that the strain is a direct and equivalent measure for the stresses induced by the externally applied force. Furthermore the strains were accessible from the acquired $z-$stacks by measuring the distances of two mitotic cells directly before and after stretching of the tissue. These circumstances lead to the decision to deploy the strains for the final analysis.[4] Labeling the component parallel to the axis of the applied force of the distance between two mitotic cells before stretching as x_1 and after stretching as x_2, the true strain is accordingly to section 3 calculated by $\varepsilon_x = \ln(x_2/x_1)$. Similarly the transversal strain is given by $\varepsilon_y = \ln(y_2/y_1)$, where y_1, y_2 correspond to the each distances component perpendicular to the axis of the applied force.
In total twenty-two late third instar wing imaginal discs were processed, of which five were used for control measurements, six were stretched by a force of 160(9) µN and eight were stretched by 350(15) µN. Compression was tested on another four wing imaginal discs. All samples had been treated equally in respect to dissection, culturing and processing apart to the external force they had been subjected to.
In figure 4.2 a time course of the longitudinal and transversal strains ε_x, ε_y a sample stretched by 160(9) µN is shown. The strains were extracted from consecutive $z-$stacks with an uncertainty of $0.005 < \delta_\varepsilon < 0.01$, which resulted from the systematic uncertainty of 2 px when localizing the centers of the mitotic cells. This systematic error was comparable to the variation in strains, which were deduced from different cell pairs of different regions of the wing imaginal disc. Thus the strains remained constant over the course of time within their uncertainties, such that in compliance with the findings of section 3.5 a considerable creep and thus plastic deformation is absent.
An exemplary choice of $z-$stack projections showing the cell outlines at three different points in time for three differently stretched wing imaginal discs are given in figure 4.1. Sample A therein was left mechanically inert, while samples B and C had been stretched by 160(9) µN, respectively 350(15) µN. The unprimed subset of images (A, B, C) shows the cell outlines directly before and the primed images (A',B',C') directly after stretching, while the set of double-primed images (A",B",C") shows the wing

[3] Cells were only considered fully divided when a daughter cell could be clearly identified.
[4] The regulatory growth model also assumes a linear relation of the materials elasticity and actually all calculations are performed considering strains, which are finally translated to the internal stress distribution of the tissue.

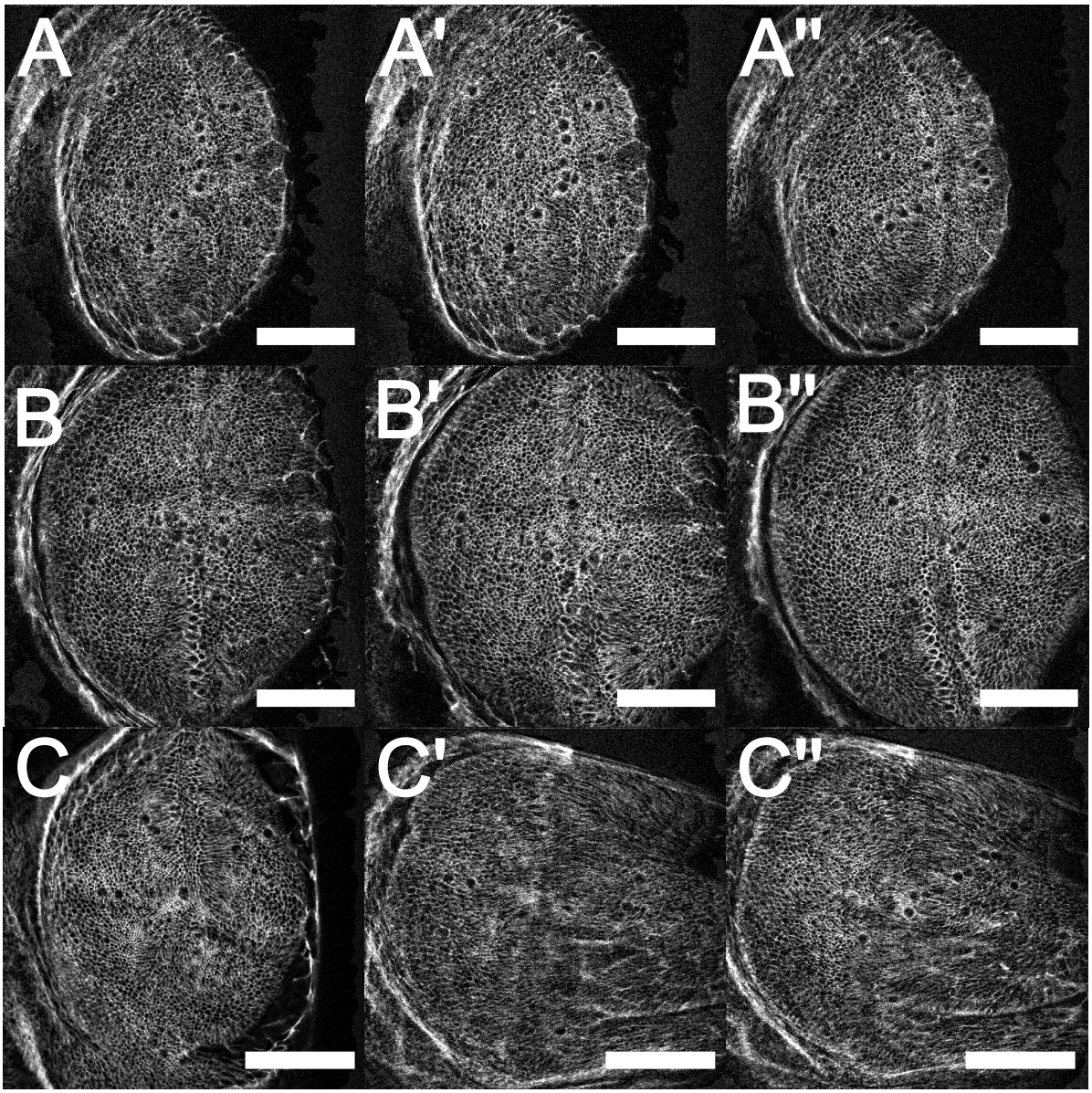

Figure 4.1 – The images are showing the cell outlines of the wing pouch for three different wing imaginal discs (A, B, C) with the discs arranged, such that the dorsal side is to the right of each image. The sample A was a control measurement and left unstretched, while sample B was stretched by 160(9) μN and sample C by 350(15) μN. The unprimed images on the left (A, B, C) depict the initial unstretched state direct after installing the sample on the setup, the images in the midsection (A',B',C') show the samples directly after application of force and the images on the right (A",B",C") after an hour of constant stretching. In the stretched samples B and C the number of mitotic cells is increased compared to the unstretched control A. Mitotic cells can be identified by their round shape and increase in apical area. Each image is an average projection of a confocal $z-$stacks. The scale bars equal 50 μm.

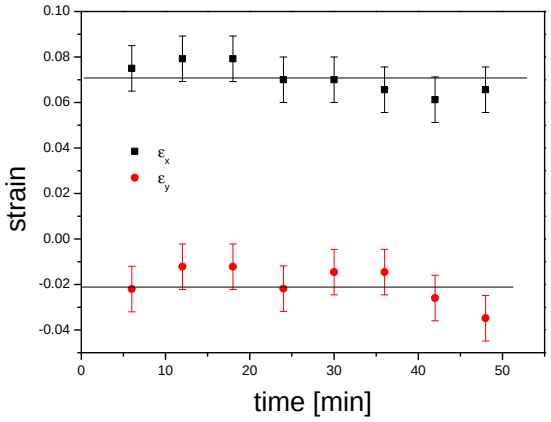

Figure 4.2 – The temporal behavior of longitudinal strain ε_x and transversal strain ε_y over a time of 60 min are shown. Strains were extracted from a sample stretched by a force of 160(9) µN. Both strains $\varepsilon_x, \varepsilon_x$ were calculated deploying the distances between different pairs of mitotic cells as explained in the text. The systematical uncertainty in determining each cell's center was between one and two pixels, which corresponded to an error of $0.005 < \delta_\varepsilon < 0.01$. This read-out error is comparable to the variation of the strains over time (standard error also ranged from 0.005 to 0.01), such that creep, respectively plastic deformation can be excluded.

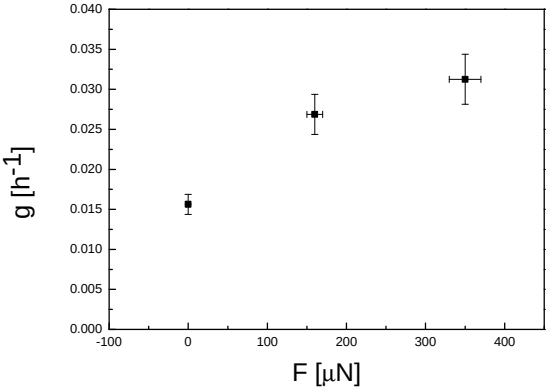

Figure 4.3 – Proliferation rates are shown as a function of two different applied forces, as well as for the unperturbed control. The data of the control correspond to an average of five samples, the data for 160(9) µN correpsonds to six and the data for 350(15) µN to eight different samples. The mean growth rate $g = 0.016(1)\,\mathrm{h}^{-1}$ of the control is considerably smaller than the in-vivo rate of $0.026(4)\,\mathrm{h}^{-1}$ and must be stretched by 160(9) µN to increase its proliferation rate to the in-vivo value. Applying a force of 350(15) µN nearly doubles the proliferation rate to $0.031(3)\,\mathrm{h}^{-1}$.

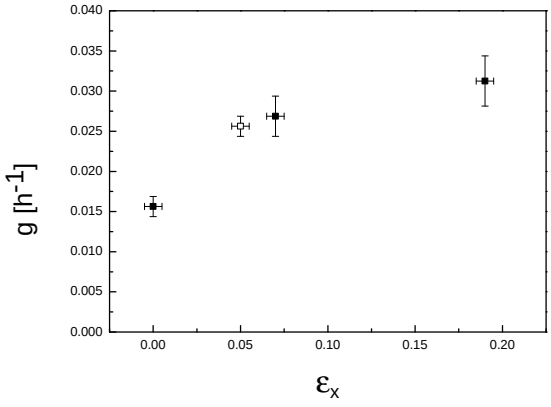

Figure 4.4 – The proliferation rates of figure 4.3 are shown as a function of the longitudinal strain ε_x in comparison to the proliferation rate of tissue that was stretched by buckling during the attempt of compressing the tissue. The data to the buckled tissue is shown by an open symbol.

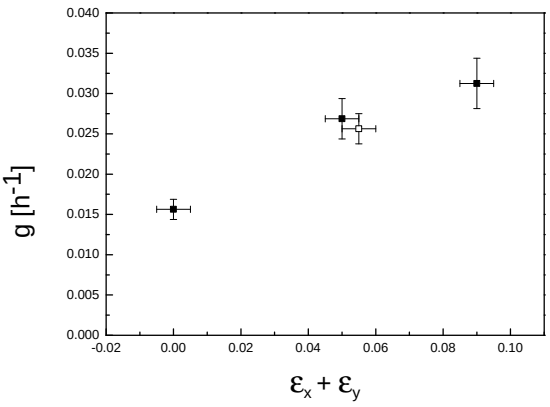

Figure 4.5 – The same data of proliferation rates of figure 4.3 is shown as a function of the trace of the strains $\varepsilon_x + \varepsilon_y$ and set in comparison to the proliferation rate of the buckled tissue. The data to the buckled tissue is shown by an open symbol.

imaginal disc after 60 min of constant external stretch.[5] Directly after the application of stress no significant change in the distribution of the mitotic cells were found, whereas the change became significant after an hour of mechanical perturbation. Comparing the stretched samples (B, C) to the unstretched control (A) an increase in dividing cells in the stretched samples relative to the unstretched control is indicated. The average change in growth rate due to an externally applied force is quantified and shown in diagram 4.3. The proliferation rate of the control measurements $g = 0.016(1)\,\mathrm{h}^{-1}$ was found to be below the in-vivo value $g = 0.026(4)\,\mathrm{h}^{-1}$ [179]. This finding may argue for restrains on the cellular proliferation resulting from non-ideal culturing conditions and the fixation of the tissue to glass. A reduction in growth rate due to the removal of mechanical stimulating structures during the dissection is possible, but seem less probable. In [180] Nienhaus et al. demonstrated and verified the existence of strain and thus stress inducing structures. These described structures were found during the early third instar and consisted of a fiber and muscle thread spanning and straining the wing imaginal tissue for roughly 20% to 50%. However, all used samples were late third instar wing imaginal discs and therefore considerably increased in size A structure that would still be able to regulate the growth of the tissue had to be of according strength and thus increased size, but such structures had not been described or found at the end of development [180, 181]. Besides these observations an externally straining structure would antagonize the accumulation and integration of the internal stresses deriving from cell proliferation. An influential external structure thus would shift the temporal point of growth cessation and should have been already observed in the transplantation experiments [6], which primarily showed the independent cessation of growth. The average number of mitotic cells one can expect in late third discs can be inferred from equation 4.1 and the in-vivo growth rate. The thereby calculated 20(4) initial mitotic cells was in good accordance to the observed numbers. Samples installed on the pulling setup and kept in Clone8 culture medium must be stretched by 160(9) µN to exhibit a proliferation rate ($g = 0.027(3)\,\mathrm{h}^{-1}$) similar to the rate in-vivo. A further increase in applied force to 350(15) µN results in an nearly doubled increase in growth rate ($g = 0.031(3)\,\mathrm{h}^{-1}$).
A wounding of the tissue for the here analyzed forces up to 350(15) µN was not observed, although for higher forces a tearing of the tissue in the hinge-notum region could be observed under the rare circumstance that the adhesion between tissue and glass was sufficiently high enough. In the wing pouch wounding was never witnessed and the strains observed were in the order of the physiological strains found in-vivo for the early stages of development [180]. All these findings suggest that the increase in proliferation rate on mechanical pulling is unlikely to be a wounding response.

To not only test the assumption that proliferation is promoted by tensile stresses, but also to scrutinize the assumptive relation between mechanical compression and suppression of growth, four wing imaginal disc were tried to be compressed. Before mounting these samples on the setup, the cantilever beam was pre-deflected and thereby pretensioned, such that a release of the cantilever resulted in a compressional force of roughly $80 - 100\,\mu\mathrm{N}$. However, due to the design of the pulling setup the wing imaginal tissue was buckling upwards instead of being compressed. A real compression of the tissue was thus technically not feasible and finally resulted in a stretching of the tissues apical side. The proliferation rate $g = 0.026(2)\,\mathrm{h}^{-1}$ of the buckled tissue equals to the proliferation rate of wing imaginal discs when stretched by 160(9) µN. However, the stretching in these both cases differ. In the case of tensile stretching an additional compressional force perpendicular to the applied force occurs, while in case of the buckled tissue such a component is missing. The average longitudinal strain for samples stretched by 160(9) µN was found to be $\varepsilon_x = 7.0(5)\%$, respectively $\varepsilon_x = 5.0(5)\%$ for the buckled tissue. Considering these longitudinal strains, the proliferation rates of the buckled and stretched tissue seem to be the results of two different strains, which is shown in figure 4.4. Taking the transversal constriction into account, i.e. determining the trace of the strain $\varepsilon_x + \varepsilon_y$, the two observed proliferation rates as well as the resulting net strain fall together. This is shown in figure 4.5 and indicates that the trace is the relevant quantity for the regulation of growth.

[5] In the case of sample A the applied stretch is 0 µN and thus of a rather hypothetical nature.

5 Summary

The objective of the thesis presented here was to gather experimental evidence to scrutinize the basic assumptions of the mechanical feedback models [11, 12, 13, 14, 15] with a special focus on the mechanical feedback model presented by Aegerter-Wilmsen et al. [13, 14, 15]. On the one hand the mechanical properties of late third instar wing imaginal disc were investigated, while on the other hand the proposed link between proliferation rate and additional mechanical stress were tested.
This was realized by designing and building a setup, which allowed the application of an uniaxial and quantitative force in the order of 10 µN to 1000 µN on a wing imaginal disc in-vitro. Further design specification have been that stretching is a non-invasive process and that the dimensions of the pulling setup are small enough to fit on an inverted microscope, allowing to monitor the imaginal tissues mechanical responses concurrently.

First force-extension measurements were performed. In these experiments wing imaginal discs were stretched in discrete steps, while their mechanical response in length and width was monitored. From the acquired data the spring constants k, the Poisson-ratio ν and the Young's modulus E had been inferred for the wing pouch and hinge-notum region as well as for the entire wing imaginal tissue. Due to the different dimensions of the wing pouch and the hinge-notum region the spring constants of these regions differed strongly. The value for the wing pouch was found to be $k_p = 2.3(1)\,\mathrm{N/m}$ and for the hinge-notum region $k_{hn} = 1.2(1)\,\mathrm{N/m}$. However, when considering these two regions as springs in series the calculated effective spring constant equaled the experimentally determined spring constant for the total tissue, i.e. $(k_p^{-1} + k_{hn}^{-1})^{-1} = k_t = 0.8(1)\,\mathrm{N/m}$.

Poisson's ratio of the hinge-notum regions and the wing pouch showed a significantly different behavior. While Poisson's ratio of the wing pouch was within the theoretical margin, i.e. $0 < \nu < 0.5$, Poisson-ration for the hinge-notum region exceeded 0.5 and went up near 1. This difference in behavior lead to the conclusion that the constriction in height can be neglected for the hinge-notum region, but not for the region of the wing pouch. Taking the differences in height and in mechanical behavior into account the elastic moduli parallel to the applied force E_x and perpendicular to the applied force E_y were calculated. The determined stress-strain curves showed a clear change in slope for longitudinal strains of 25% and higher. This change could be related to the unfolding of the tissue and a corresponding estimations had been made in section 3.3. Based on these considerations Young's moduli for longitudinal strains bigger 25% were taken as the materials elastic moduli. All elastic moduli were found to be equal within their uncertainties, such that the differences in spring constants and Poisson-ratios can be traced back to the the tissues geometry and its tear-drop shape.

The next set of experiments consisted of birefringence measurements, similar to the experiments done by Nienhaus et al. [16]. However in this case the possibility was given to quantitatively apply a force on the tissue and thereby determine the photo-elastic constant C, which was found to be on average $C = 1.9(7) \cdot 10^{-10}\,\mathrm{Pa}^{-1}$. Deploying the photo-elastic constant, the stresses of dissected but otherwise untreated late third wing imaginal disc were quantified. The stresses within the wing pouch were found to be about $3.4(1) \cdot 10^5\,\mathrm{Pa}$ and half in the hinge-notum area $1.6(1) \cdot 10^5\,\mathrm{Pa}$. Straining such a sample by hand about 30%, resulted in a significant drop of the stresses in the wing pouch from $3.6(1) \cdot 10^5\,\mathrm{Pa}$ to $1.7(1) \cdot 10^5\,\mathrm{Pa}$ and is consistend with the applied tensile stress of $1.6(1)10^5\,\mathrm{Pa}$, while the level of the hinge-notum region hardly changed. These results support the assumption of an accumulation of compressional stresses during the development of the wing discs.

To test the wing imaginal discs temporal response, samples were elongated until one side loosened and eventually relaxed. Modeling the imaginal discs as a damped system the spring constant of the tissue k_t and the tissues dynamic response time τ could be calculated. The spring constant was found to be $k_t = 0.8(1)\,\mathrm{N/m}$ and thus is consistent with the values found earlier. The dynamic response time was determined to $\tau = 12(3)\,\mathrm{s}$, meaning that strains exerted for a longer time on the tissue will contribute to the tissues inner stress distribution. Proliferation, which happens on a time scale of several minutes thus contributes to mechanical stress. On the other hand the dynamical response time τ is bigger than the time of the larva's peristaltic movement, such that the strains exerted by this movement can not contribute to the tissues stress distribution.
The wing imaginal tissue obeys Hooke's law and behaves linear elastic over an remarkably range of strain. It does not reveal any considerable mechanical hysteresis and it did not show plasticity unless it was seriously affected in its health, which however was only shown in a proof of principles.

Finally the influence of tensile stress on the proliferation rates were investigated by stretching wing imaginal discs constantly over the course of one hour and monitoring the mitotic activity in the wing pouch. The externally applied forces ranged from 0 µN over 160(9) µN to 350(15) µN with the measurement at 0 µN being control measurements. The acquired data indicates a relation between tensile stress and cell proliferation, because the observed proliferation rates increased with increased externally applied force. The attempted test to compress the wing imaginal disc failed, as the tissue always buckled[1], which resulted in an effective stretching without any transversal compressional component. Comparing the data of buckled to elongated wing imaginal disc indicates that cells sense the total amount of stress they are exposed to. Creep could not be observed within the tissue as the monitoring of longitudinal and transversal strains over course of one hour indicated.

In conclusion it can be said, that the wing imaginal tissue is highly elastic and shows little to no plasticity or creep making the accumulation of stress possible. Its dynamical response time is in a range, that allows stresses to built up on timescales greater than its dynamic response time and keeps the system mechanical separated from perturbations on short timescales like the peristaltic movement of the larva. Tensile stress seem to reduce the stresses in the wing disc pouch indicating that compressional stress is present in the pouch. Tensile stress also seems to increase cell proliferation. All these experimental findings presented in this thesis speak strongly for the assumptions made by the mechanical feedback models and for the feedback model itself.

[1] Not to be confused with the folded topology of the wing imaginal disc

Curriculum Vitae

Personal Information

Name	Thomas Schluck
Date of Birth	1980/07/29
Place of Birth	Hechingen
Nationality	German

Education

08/2008 - 12/2013	PhD at the University of Zurich, Title of thesis: "Mechanical Perturbation and Stimulation of *Drosophila* Wing Imaginal Discs"
01/2008	Diploma in physics, Title of thesis: "Erzeugung definierter Defekte in metallischen Nanodrähten mit Hilfe eines Rastertunnelmikroskops"
2000	Abitur, Gymnasium Hechingen

Scholarships and Fundings

09/2004 - 07/2005	Scholarship from Fudan University, academic year at Fudan university, Shanghai
10/2011 - 07/2012	Funding from the "Forschungskredit" of the University of Zurich

Acknowledgments

I would like to thank all the people without whom this thesis might not have been written.
Foremost, I would like to express my deep appreciation and gratitude to my advisor, Dr. Christof Aegerter, for giving me the opportunity to work on a most interesting and interdisciplinary field of science. Being allowed to contribute and help building up our research group from the very beginning has been an invaluable experience to me and fills me with pride. The granted freedom in my work and research as well as our profound and intense discussions helped me to grow as a scientist and person.
Special thanks to my second examiner Richard Smith, who was not only spending his time on reading, but also correcting my thesis. His comments, suggestions and annotations as well as our disscusion were uttermost helpful and I have greatly benefited from these.
I would also like to show my appreciation to the members of my committee, Hugo Keller and Damian Brunner, making my defense insightful and joyful.
I would like to thank Tinri Aegerter-Wilmsen for all the discussions about the theory and experiments on growth regulation and especially for the discussions interpreting my results.
My deepest gratitude to my colleagues and lab-members Ulrike Nienhaus, Giulia Ghielmetti, Dominik Eder and Daniel Assmann for sharing this part of my life's journey with me. Thank you for all the discussions on research and non-research and for helping each other whenever necessary and possible. My special appreciation I owe to Ulrike for sharing her knowledge on larval dissection with me.
I am in debt to many students, who I was allowed to supervise and mentor. Related to this work I have to mention Michael Schindlberger who helped me building the pulling setup in his BA thesis, Susanne Guldener-Guggenbach who did most of the dynamic response measurement during her internship in our lab and Seline Eisenring and Kay Hänggi who did some of the photo-elastic measurements. All of them did an outstanding job.
To the Physics Institute and its staff, giving me a home at the university and being a starting point for any task I was challenged with. Explicitly, I would like to express my dearest thanks to Roland Bernet who helped me out with all IT issues during and after building our group, to Kurt Bösiger, Reto Maier, Bruno Lussi, Marcel Schaffner and Silvio Scherr from the outstanding workshop of the institute and to the institute's secretaries Ruth Halter and Monika Röllin leading and guiding me through the depths of the university's bureaucracy.
When working in an interdisciplinary field profound collaborations are essential. Without our many different collaborators many of the experiments presented and discussed here would not have been realized. Stefan Luschnig's comments and our regular group meetings of physicists and biologists were an enormous help for me and provided a mean to me to develop a better biological understanding. Stefan as well as Konrad Basler and his group provided me with different kind of flies for my experiments and allowed me to use their laboratory's infrastructure, which I am deeply grateful for. Particularly, I would like to thank Jeremiah Zartman for an insightful discussion about culture media and providing me with a batch of ordinary Clone8 to jump start my experiments on the mechanical regulation of growth. In this context, my special appreciations to Simon Restrepo for his impressive lecture on differences in cultures.
Without the proper funding all of this work would not have been possible and so I also would like to express my gratitude to the WingX initiative and the Forschungskredit of the University of Zurich for their financial support.

My warm and dearest thanks to Silke. Thank you for coaching, supporting and working with me and especially for your friendly ear in a very tough period of this thesis. To Sue and Fluff and Janine a big "Thanks!" for hours of proof-reading.
I am overwhelmingly grateful to my family and especially my wife and daughter. My dear wife Judith supported me, accompanied me and stood by my side at all times. Thank you for your good energy, love, trust and keeping up with my (long-distance) final rush. My daughter Leopoldina certainly did not make me start my thesis, but surely helped me finish it. Thank you.

Bibliography

[1] W. Bialek and D. Botstein, "Introductory science and mathematics education for 21st-century biologists," *Science Signaling*, vol. 303, no. 5659, p. 788, 2004.

[2] A. Lander, Q. Nie, B. Vargas, and F. Wan, "Size-normalized robustness of dpp gradient in drosophila wing imaginal disc," *Journal of mechanics of materials and structures*, vol. 6, no. 1-4, p. 321, 2011.

[3] G. Schwank and K. Basler, "Regulation of organ growth by morphogen gradients," *Cold Spring Harbor perspectives in biology*, vol. 2, no. 1, pp. 1–16, 2010.

[4] P. Bryant and P. Levinson, "Intrinsic growth control in the imaginal primordia of drosophila, and the autonomous action of a lethal mutation causing overgrowth," *Developmental biology*, vol. 107, no. 2, pp. 355–363, 1985.

[5] F. A. Martín, S. C. Herrera, and G. Morata, "Cell competition, growth and size control in the drosophila wing imaginal disc," *Development*, vol. 136, pp. 3747–3756, Nov. 2009.

[6] S. Day and P. Lawrence, "Measuring dimensions: the regulation of size and shape," *Development*, vol. 127, no. 14, pp. 2977–2987, 2000.

[7] M. Affolter and K. Basler, "The decapentaplegic morphogen gradient: from pattern formation to growth regulation," *Nature Reviews Genetics*, vol. 8, no. 9, pp. 663–674, 2007.

[8] M. Milán, S. Campuzano, and A. García-Bellido, "Cell cycling and patterned cell proliferation in the wing primordium of drosophila," *Proceedings of the National Academy of Sciences*, vol. 93, pp. 640–645, Jan 1996.

[9] G. Schwank, S. Restrepo, and K. Basler, "Growth regulation by dpp: an essential role for brinker and a non-essential role for graded signaling levels," *Development*, vol. 135, no. 24, pp. 4003–4013, 2008.

[10] G. Schwank, S. Dalessi, S.-F. Yang, R. Yagi, A. M. de Lachapelle, M. Affolter, S. Bergmann, and K. Basler, "Formation of the long range dpp morphogen gradient," *PLoS Biol*, vol. 9, p. e1001111, 07 2011.

[11] B. I. Shraiman, "Mechanical feedback as a possible regulator of tissue growth," *Proceedings of the National Academy of Sciences of the United States of America*, vol. 102, pp. 3318–3323, Jan. 2005.

[12] L. Hufnagel, A. Teleman, H. Rouault, S. Cohen, and B. Shraiman, "On the mechanism of wing size determination in fly development," *Proceedings of the National Academy of Sciences*, vol. 104, no. 10, pp. 3835–3840, 2007.

[13] T. Aegerter-Wilmsen, C. M. Aegerter, E. Hafen, and K. Basler, "Model for the regulation of size in the wing imaginal disc of drosophila," *Mechanisms of Development*, vol. 124, pp. 318–326, Apr. 2007.

[14] T. Aegerter-Wilmsen, A. Smith, A. Christen, C. Aegerter, E. Hafen, and K. Basler, "Exploring the effects of mechanical feedback on epithelial topology," *Development*, vol. 137, no. 3, pp. 499–506, 2010.

[15] T. Aegerter-Wilmsen, M. Heimlicher, A. Smith, P. de Reuille, R. Smith, C. Aegerter, and K. Basler, "Integrating force-sensing and signaling pathways in a model for the regulation of wing imaginal disc size," *Development*, vol. 139, no. 17, pp. 3221–3231, 2012.

[16] U. Nienhaus, T. Aegerter-Wilmsen, and C. M. Aegerter, "Determination of mechanical stress distribution in drosophila wing discs using photoelasticity," *Mechanisms of Development*, vol. 126, no. 11-12, pp. 942 – 949, 2009.

[17] S. Ishihara and K. Sugimura, "Bayesian inference of force dynamics during morphogenesis," *Journal of Theoretical Biology*, vol. 313, no. 0, pp. 201 – 211, 2012.

[18] L. Wolpert and C. Tickle, *Principles of Development*. Oxford University Press, 4th edition. ed., Jan. 2011.

[19] G. F. Oster, J. D. Murray, and A. K. Harris, "Mechanical aspects of mesenchymal morphogenesis," *Journal of Embryology and Experimental Morphology*, vol. 78, pp. 83–125, Jan. 1983.

[20] V. Petrov and C. Aegerter, "Integrating mechanical control theory into models of biological development - analytical review," *Journal of Mechanics in Medicine and Biology*, vol. 11, pp. 713–734, Sept. 2011.

[21] B. Alberts, *Essential Cell Biology: An introducton to the Molecular Biology of the Cell*, vol. 3. Garland Science, 2009.

[22] B. Alberts, A. Johnson, J. Lewis, M. Raff, K. Roberts, and P. Walter, *Molecular biology of the cell*. Garland Science Taylor & Francis Group, 5 ed., 2008.

[23] L. Wolpert, R. Beddington, T. Jessell, P. Lawrence, E. Meyerowitz, and J. Smith, *Principles of development*, vol. 3. Oxford University Press New York, 2002.

[24] J. Shannon and D. Pitelka, "The influence of cell shape on the induction of functional differentiation in mouse mammary cells in vitro," *In Vitro*, vol. 17, pp. 1016–1028, 1981.

[25] C. M. Nelson, "Geometric control of tissue morphogenesis," *Biochimica et Biophysica Acta (BBA) - Molecular Cell Research*, vol. 1793, no. 5, pp. 903 – 910, 2009.

[26] C. Nelson and M. Bissell, "Of extracellular matrix, scaffolds, and signaling: tissue architecture regulates development, homeostasis, and cancer," *Annual review of cell and developmental biology*, vol. 22, p. 287, 2006.

[27] A. J. Koch and H. Meinhardt, "Biological pattern formation: from basic mechanisms to complex structures," *Rev. Mod. Phys.*, vol. 66, pp. 1481–1507, Oct 1994.

[28] A. Turing, "The chemical basis of morphogenesis," *Philosophical Transactions of the Royal Society of London. Series B, Biological Sciences*, vol. 237, pp. 37–72, August 1952. Classics of Theoretical Biology.

[29] A. Gierer and H. Meinhardt, "A theory of biological pattern formation," *Biological Cybernetics*, vol. 12, no. 1, pp. 30–39, 1972.

[30] H. Meinhardt, *Models of biological pattern formation*, vol. 6. Academic Press London, 1982.

[31] H. Meinhardt, "Models for the generation and interpretation of gradients," *Cold Spring Harbor perspectives in biology*, vol. 1, no. 4, pp. 1–14, 2009.

[32] H. Ashe and J. Briscoe, "The interpretation of morphogen gradients," *Development*, vol. 133, no. 3, pp. 385–394, 2006.

[33] L. Wolpert, "Positional information and the spatial pattern of cellular differentiation," *Journal of Theoretical Biology*, vol. 25, no. 1, pp. 1 – 47, 1969.

[34] H. Meinhardt, "Space-dependent cell determination under the control of a morphogen gradient," *Journal of theoretical biology*, vol. 74, no. 2, pp. 307–321, 1978.

[35] H. Othmer and E. Pate, "Scale-invariance in reaction-diffusion models of spatial pattern formation," *Proceedings of the National Academy of Sciences*, vol. 77, no. 7, pp. 4180–4184, 1980.

[36] S. Ishihara and K. Kaneko, "Turing pattern with proportion preservation," *Journal of theoretical biology*, vol. 238, no. 3, pp. 683–693, 2006.

[37] M. S. Steinberg, "Reconstruction of tissues by dissociated cells. some morphogenetic tissue movements and the sorting out of embryonic cells may have a common explanation.," *Science*, vol. 141, no. 3579, pp. 401–408, 1963.

[38] L. P.-F. Lecuit, Thomas, "Cell surface mechanics and the control of cell shape, tissue patterns and morphogenesis," *Nat Rev Mol Cell Biol*, vol. 8, pp. 633 – 644, August 2007.

[39] R. A. Foty and M. S. Steinberg, "The differential adhesion hypothesis: a direct evaluation," *Developmental Biology*, vol. 278, no. 1, pp. 255 – 263, 2005.

[40] T. Hayashi and R. Carthew, "Surface mechanics mediate pattern formation in the developing retina," *Nature*, vol. 431, no. 7009, pp. 647–652, 2004.

[41] M. Steinberg and M. Takeichi, "Experimental specification of cell sorting, tissue spreading, and specific spatial patterning by quantitative differences in cadherin expression," *Proceedings of the National Academy of Sciences*, vol. 91, no. 1, pp. 206–209, 1994.

[42] D. Beysens, G. Forgacs, and J. Glazier, "Cell sorting is analogous to phase ordering in fluids," *Proceedings of the National Academy of Sciences*, vol. 97, no. 17, pp. 9467–9471, 2000.

[43] C. M. Niessen and B. M. Gumbiner, "Cadherin-mediated cell sorting not determined by binding or adhesion specificity," *The Journal of Cell Biology*, vol. 156, no. 2, pp. 389–400, 2002.

[44] G. Brodland *et al.*, "The differential interfacial tension hypothesis (dith): a comprehensive theory for the self-rearrangement of embryonic cells and tissues.," *Journal of biomechanical engineering*, vol. 124, no. 2, p. 188, 2002.

[45] R. Farhadifar, J.-C. Röper, B. Aigouy, S. Eaton, and F. Jülicher, "The influence of cell mechanics, cell-cell interactions, and proliferation on epithelial packing," *Current Biology*, vol. 17, no. 24, pp. 2095 – 2104, 2007.

[46] J. Amack and M. Manning, "Knowing the boundaries: Extending the differential adhesion hypothesis in embryonic cell sorting," *Science*, vol. 338, no. 6104, pp. 212–215, 2012.

[47] F. Pilot and T. Lecuit, "Compartmentalized morphogenesis in epithelia: from cell to tissue shape," *Developmental dynamics*, vol. 232, no. 3, pp. 685–694, 2005.

[48] C. Bertet, L. Sulak, and T. Lecuit, "Myosin-dependent junction remodelling controls planar cell intercalation and axis elongation," *Nature*, vol. 429, no. 6992, pp. 667–671, 2004.

[49] B. A. Edgar and C. F. Lehner, "Developmental control of cell cycle regulators: A fly's perspective," *Science*, vol. 274, no. 5293, pp. 1646–1652, 1996.

[50] T. T. Su and P. H. O'Farrell, "Size control: Cell proliferation does not equal growth," *Current Biology*, vol. 8, no. 19, pp. R687 – R689, 1998.

[51] D. Morgan, *The Cell Cycle: Principles of Control*. Primers in Biology, New Science Press, 2007.

[52] G. Johnston, J. Pringle, and L. Hartwell, "Coordination of growth with cell division in the yeast saccharomyces cerevisiae," *Experimental Cell Research*, vol. 105, no. 1, pp. 79 – 98, 1977.

[53] G. Johnston, C. Ehrhardt, A. Lorincz, and B. Carter, "Regulation of cell size in the yeast saccharomyces cerevisiae.," *Journal of bacteriology*, vol. 137, no. 1, pp. 1–5, 1979.

[54] L. J. Saucedo and B. A. Edgar, "Why size matters: altering cell size," *Current Opinion in Genetics & Development*, vol. 12, no. 5, pp. 565 – 571, 2002.

[55] P. Jorgensen and M. Tyers, "How cells coordinate growth and division," *Current Biology*, vol. 14, no. 23, pp. R1014 – R1027, 2004.

[56] I. Conlon and M. Raff, "Size control in animal development," *Cell*, vol. 96, no. 2, pp. 235 – 244, 1999.

[57] I. Conlon and M. Raff, "Differences in the way a mammalian cell and yeast cells coordinate cell growth and cell-cycle progression," *Journal of Biology*, vol. 2, no. 1, p. 7, 2003.

[58] S. Grewal and B. Edgar, "Controlling cell division in yeast and animals: does size matter?," *Journal of Biology*, vol. 2, no. 1, p. 5, 2003.

[59] G. A. Wray and E. Abouheif, "When is homology not homology?," *Current Opinion in Genetics & Development*, vol. 8, no. 6, pp. 675 – 680, 1998.

[60] D. E. Ingber, "Mechanical control of tissue morphogenesis during embryological development," *The International Journal of Developmental Biology*, vol. 50, no. 2-3, pp. 255–266, 2006.

[61] C. M. Nelson, R. P. Jean, J. L. Tan, W. F. Liu, N. J. Sniadecki, A. A. Spector, and C. S. Chen, "Emergent patterns of growth controlled by multicellular form and mechanics," *Proceedings of the National Academy of Sciences of the United States of America*, vol. 102, no. 33, pp. 11594–11599, 2005.

[62] D. M. Brunette, "Mechanical stretching increases the number of epithelial cells synthesizing DNA in culture," *Journal of Cell Science*, vol. 69, pp. 35–45, Jan. 1984.

[63] F. Montel, M. Delarue, J. Elgeti, L. Malaquin, M. Basan, T. Risler, B. Cabane, D. Vignjevic, J. Prost, G. Cappello, and J.-F. Joanny, "Stress clamp experiments on multicellular tumor spheroids," *Physical Review Letters*, vol. 107, p. 188102, Oct. 2011.

[64] P. Bryant and P. Simpson, "Intrinsic and extrinsic control of growth in developing organs," *Quarterly Review of Biology*, pp. 387–415, 1984.

[65] R. Wehner and W. Gehring, *Zoologie*. Thieme, 24 ed., 2007.

[66] G. Fankhauser, "Nucleo-cytoplasmic relations in amphibian development," vol. 1 of *International Review of Cytology*, pp. 165 – 193, Academic Press, 1952.

[67] P. Nurse, "The genetic control of cell volume," *The evolution of genome size*, pp. 185–196, 1985.

[68] R. J. Goss *et al.*, *The physiology of growth.* Academic Press Inc.(London) Ltd., 1978.

[69] W. Bursch, H. Taper, B. Lauer, and R. Schulte-Hermann, "Quantitative histological and histochemical studies on the occurrence and stages of controlled cell death (apoptosis) during regression of rat liver hyperplasia," *Virchows Archiv B*, vol. 50, pp. 153–166, 1986.

[70] G. K. Michalopoulos and M. C. DeFrances, "Liver regeneration," *Science*, vol. 276, no. 5309, pp. 60–66, 1997.

[71] P. Bryant and O. Schmidt, "The genetic control of cell proliferation in drosophila imaginal discs.," *Journal of cell science.*, vol. 13, p. 169, 1990.

[72] P. A. Lawrence, *The Making of a Fly: The Genetics of Animal Design.* Wiley-Blackwell, 1 ed., Apr. 1992.

[73] V. French, M. Feast, and L. Partridge, "Body size and cell size in drosophila: the developmental response to temperature," *Journal of Insect Physiology*, vol. 44, no. 11, pp. 1081 – 1089, 1998.

[74] R. J. Greenspan, *Fly Pushing: The Theory and Practice of Drosophila Genetics.* Cold Spring Harbor Laboratory, 0002 ed., July 2004.

[75] J. Kang, H.-G. Lemaire, A. Unterbeck, J. M. Salbaum, C. L. Masters, K.-H. Grzeschik, G. Multhaup, K. Beyreuther, and B. Müller-Hill, "The precursor of alzheimer's disease amyloid a4 protein resembles a cell-surface receptor," 1987.

[76] B. Sanson, "Generating patterns from fields of cells," *EMBO reports 2*, vol. 12, pp. 1083–1088, November 2001.

[77] T. Phillips, "Genetic signaling: Transcription factor cascades and segmentation." http://www.nature.com/scitable/topicpage/genetic-signaling-transcription-factor-cascades-and-segmentation-1058, 2008.

[78] S. C. Little, G. Tkačik, T. B. Kneeland, E. F. Wieschaus, and T. Gregor, "The formation of the bicoid morphogen gradient requires protein movement from anteriorly localized mRNA," *PLoS Biol*, vol. 9, p. e1000596, Mar. 2011.

[79] B. Cohen, A. Simcox, and S. Cohen, "Allocation of the thoracic imaginal primordia in the drosophila embryo," *Development*, vol. 117, no. 2, pp. 597–608, 1993.

[80] N. Serrano and P. H. O'Farrell, "Limb morphogenesis: connections between patterning and growth," *Current Biology*, vol. 7, pp. R186 – R195, Mar 1997.

[81] T. Bittig, O. Wartlick, M. Gonzalez-Gaitan, and F. Jülicher, "Quantification of growth asymmetries in developing epithelia," *The European Physical Journal E*, vol. 30, pp. 93–99, Sept. 2009.

[82] V. Jursnich, S. Fraser, L. Held, J. Ryerse, and P. Bryant, "Defective gap-junctional communication associated with imaginal disc overgrowth and degeneration caused by mutations of the dco gene in drosophila," *Developmental biology*, vol. 140, no. 2, pp. 413–429, 1990.

[83] C. K. Mirth and L. M. Riddiford, "Size assessment and growth control: how adult size is determined in insects," *Bioessays*, vol. 29, no. 4, pp. 344–355, 2007.

[84] M. Butler, T. Jacobsen, D. Cain, M. Jarman, M. Hubank, J. Whittle, R. Phillips, and A. Simcox, "Discovery of genes with highly restricted expression patterns in the drosophila wing disc using dna oligonucleotide microarrays," *Development*, vol. 130, no. 4, pp. 659–670, 2003.

[85] C. Dahmann and K. Basler, "Compartment boundaries: at the edge of development," *Trends in Genetics*, vol. 15, no. 8, pp. 320 – 326, 1999.

[86] K. Basler, G. Struhl, *et al.*, "Compartment boundaries and the control of drosophila limb pattern by hedgehog protein," *Nature*, vol. 368, pp. 208–214, Mar 1994.

[87] S. Blair and A. Ralston, "Smoothened-mediated hedgehog signalling is required for the maintenance of the anterior-posterior lineage restriction in the developing wing of drosophila," *Development*, vol. 124, no. 20, pp. 4053–4063, 1997.

[88] I. Rodriguez and K. Basler, "Control of compartmental affinity boundaries by hedgehog," *Nature*, vol. 389, no. 6651, pp. 614–618, 1997.

[89] C. Dahmann and K. Basler, "Opposing transcriptional outputs of hedgehog signaling and engrailed control compartmental cell sorting at the drosophila a/p boundary," *Cell*, vol. 100, no. 4, pp. 411 – 422, 2000.

[90] T. Lecuit, W. Brook, M. Ng, M. Calleja, H. Sun, and S. Cohen, "Two distinct mechanisms for long-range patterning by decapentaplegic in the drosophila wing," *Nature*, vol. 381, no. 6581, pp. 387–393, 1996.

[91] D. Nellen, R. Burke, G. Struhl, and K. Basler, "Direct and long-range action of a dpp morphogen gradient," *Cell*, vol. 85, no. 3, pp. 357 – 368, 1996.

[92] M. Moser and G. Campbell, "Generating and interpreting the brinker gradient in the drosophila wing," *Developmental Biology*, vol. 286, no. 2, pp. 647 – 658, 2005.

[93] B. Müller, B. Hartmann, G. Pyrowolakis, M. Affolter, and K. Basler, "Conversion of an extracellular dpp/bmp morphogen gradient into an inverse transcriptional gradient," *Cell*, vol. 113, no. 2, pp. 221 – 233, 2003.

[94] O. Wartlick, P. Mumcu, F. Jülicher, and M. Gonzalez-Gaitan, "Understanding morphogenetic growth control - lessons from flies," *Nature Reviews Molecular Cell Biology*, vol. 12, pp. 594–604, Sept. 2011.

[95] A. A. Teleman and S. M. Cohen, "Dpp gradient formation in the drosophila wing imaginal disc," *Cell*, vol. 103, pp. 971–980, Dec. 2000.

[96] A. D. Lander, Q. Nie, and F. Y. Wan, "Do morphogen gradients arise by diffusion?," *Developmental Cell*, vol. 2, no. 6, pp. 785 – 796, 2002.

[97] A. Kicheva, P. Pantazis, T. Bollenbach, Y. Kalaidzidis, T. Bittig, F. Julicher, and M. González-Gaitán, "Kinetics of morphogen gradient formation," *Science Signalling*, vol. 315, no. 5811, p. 521, 2007.

[98] T. Bollenbach, K. Kruse, P. Pantazis, M. González-Gaitán, and F. Jülicher, "Robust formation of morphogen gradients," *Phys. Rev. Lett.*, vol. 94, p. 018103, Jan 2005.

[99] S. Zhou, W.-C. Lo, J. Suhalim, M. Digman, E. Gratton, Q. Nie, and A. Lander, "Free extracellular diffusion creates the dpp morphogen gradient of the drosophila wing disc," *Current Biology*, vol. 22, no. 8, pp. 668 – 675, 2012.

[100] A. Kicheva and M. González-Gaitán, "The decapentaplegic morphogen gradient: a precise definition," *Current Opinion in Cell Biology*, vol. 20, no. 2, pp. 137 – 143, 2008. Cell regulation.

[101] O. Wartlick, A. Kicheva, and M. González-Gaitán, "Morphogen gradient formation," *Cold Spring Harbor Perspectives in Biology*, vol. 1, no. 3, pp. 1–22, 2009.

[102] P. A. Lawrence and G. Struhl, "Morphogens, compartments, and pattern: Lessons from drosophila?," *Cell*, vol. 85, no. 7, pp. 951 – 961, 1996.

[103] K. Irvine and C. Rauskolb, "Boundaries in development: formation and function," *Annual review of cell and developmental biology*, vol. 17, no. 1, pp. 189–214, 2001.

[104] F. Diaz-Benjumea and S. Cohen, "Interaction between dorsal and ventral cells in the imaginal disc directs wing development in drosophila," *Cell*, vol. 75, no. 4, pp. 741–752, 1993.

[105] A. González, C. Chaouiya, and D. Thieffry, "Dynamical analysis of the regulatory network defining the dorsal–ventral boundary of the drosophila wing imaginal disc," *Genetics*, vol. 174, no. 3, pp. 1625–1634, 2006.

[106] M. Zecca, K. Basler, and G. Struhl, "Direct and long-range action of a wingless morphogen gradient," *Cell*, vol. 87, no. 5, pp. 833 – 844, 1996.

[107] J. Williams, S. Paddock, and S. Carroll, "Pattern formation in a secondary field: a hierarchy of regulatory genes subdivides the developing drosophila wing disc into discrete subregions," *Development*, vol. 117, no. 2, pp. 571–584, 1993.

[108] S. Swarup and E. M. Verheyen, "Wnt/wingless signaling in drosophila," *Cold Spring Harbor Perspectives in Biology*, vol. 4, pp. 1–15, Jan 2012.

[109] A. García-Bellido, P. Ripoll, and G. Morata, "Developmental compartmentalisation of the wing disk of drosophila," *Nature*, vol. 245, pp. 251–253, Oct. 1973.

[110] M. C. Gibson, A. B. Patel, R. Nagpal, and N. Perrimon, "The emergence of geometric order in proliferating metazoan epithelia," *Nature*, vol. 442, no. 7106, pp. 1038–1041, 2006.

[111] K. P. Landsberg, R. Farhadifar, J. Ranft, D. Umetsu, T. J. Widmann, T. Bittig, A. Said, F. Jülicher, and C. Dahmann, "Increased cell bond tension governs cell sorting at the drosophila anteroposterior compartment boundary," *Current Biology*, vol. 19, no. 22, pp. 1950 – 1955, 2009.

[112] B. Monier, A. Pélissier-Monier, A. Brand, and B. Sanson, "An actomyosin-based barrier inhibits cell mixing at compartmental boundaries in drosophila embryos," *Nature cell biology*, vol. 12, no. 1, pp. 60–65, 2009.

[113] S. Schilling, M. Willecke, T. Aegerter-Wilmsen, O. A. Cirpka, K. Basler, and C. von Mering, "Cell-sorting at the a/p boundary in the drosophila wing primordium: A computational model to consolidate observed non-local effects of hh signaling," *PLoS Comput Biol*, vol. 7, p. e1002025, 04 2011.

[114] M. Aliee, J.-C. Röper, K. Landsberg, C. Pentzold, T. Widmann, F. Jülicher, and C. Dahmann, "Physical mechanisms shaping the drosophila dorsoventral compartment boundary," *Current Biology*, vol. 22, no. 11, pp. 967 – 976, 2012.

[115] J. Kim, A. Sebring, J. Esch, M. Kraus, K. Vorwerk, J. Magee, and S. Carroll, "Integration of positional signals and regulation of wing formation and identity by drosophila vestigial gene," *Nature*, vol. 382, pp. 133–138, 1996.

[116] M. Zecca and G. Struhl, "Recruitment of cells into the drosophila wing primordium by a feed-forward circuit of vestigial autoregulation," *Development*, vol. 134, no. 16, pp. 3001–3010, 2007.

[117] M. Zecca and G. Struhl, "A feed-forward circuit linking wingless, fat-dachsous signaling, and the warts-hippo pathway to drosophila wing growth," *PLoS Biol*, vol. 8, p. e1000386, 06 2010.

[118] G. Beadle, E. Tatum, and C. Clancy, "Food level in relation to rate of development and eye pigmentation

in drosophila melanogaster," *The Biological Bulletin*, vol. 75, no. 3, pp. 447–462, 1938.

[119] M. Sturtevant, B. Biehs, E. Marin, and E. Bier, "The spalt gene links the a/p compartment boundary to a linear adult structure in the drosophila wing," *Development*, vol. 124, no. 1, pp. 21–32, 1997.

[120] T. Bollenbach, P. Pantazis, A. Kicheva, C. Bökel, M. González-Gaitán, and F. Jülicher, "Precision of the dpp gradient," *Development*, vol. 135, no. 6, pp. 1137–1146, 2008.

[121] J. Hériché, D. Ang, E. Bier, and P. O'Farrell, "Involvement of an scfslmb complex in timely elimination of e2f upon initiation of dna replication in drosophila," *BMC genetics*, vol. 4, no. 1, p. 9, 2003.

[122] F. Hamaratoglu, A. M. de Lachapelle, G. Pyrowolakis, S. Bergmann, and M. Affolter, "Dpp signaling activity requires pentagone to scale with tissue size in the growing drosophila wing imaginal disc," *PLoS Biol*, vol. 9, p. e1001182, 10 2011.

[123] O. Wartlick, P. Mumcu, A. Kicheva, T. Bittig, C. Seum, F. Jülicher, and M. González-Gaitán, "Dynamics of dpp signaling and proliferation control," *Science*, vol. 331, pp. 1154–1159, Apr. 2011.

[124] D. Ben-Zvi, G. Pyrowolakis, N. Barkai, and B.-Z. Shilo, "Expansion-repression mechanism for scaling the dpp activation gradient in drosophila wing imaginal discs," *Current Biology*, vol. 21, no. 16, pp. 1391 – 1396, 2011.

[125] D. Ben-Zvi and N. Barkai, "Scaling of morphogen gradients by an expansion-repression integral feedback control," *Proceedings of the National Academy of Sciences*, vol. 107, no. 15, pp. 6924–6929, 2010.

[126] M. González-Gaitán, M. P. Capdevila, and A. García-Bellido, "Cell proliferation patterns in the wing imaginal disc of drosophila," *Mechanisms of Development*, vol. 46, no. 3, pp. 183 – 200, 1994.

[127] G. Morata and P. Ripoll, "Minutes: Mutants of drosophila autonomously affecting cell division rate," *Developmental Biology*, vol. 42, no. 2, pp. 211 – 221, 1975.

[128] P. Simpson and G. Morata, "Differential mitotic rates and patterns of growth in compartments in the drosophila wing," *Developmental Biology*, vol. 85, no. 2, pp. 299 – 308, 1981.

[129] T. P. Neufeld, A. F. A. de la Cruz, L. A. Johnston, and B. A. Edgar, "Coordination of growth and cell division in the drosophila wing," *Cell*, vol. 93, no. 7, pp. 1183 – 1193, 1998.

[130] K. Weigmann, S. Cohen, and C. Lehner, "Cell cycle progression, growth and patterning in imaginal discs despite inhibition of cell division after inactivation of drosophila cdc2 kinase," *Development*, vol. 124, no. 18, pp. 3555–3563, 1997.

[131] V. French, P. Bryant, S. Bryant, *et al.*, "Pattern regulation in epimorphic fields.," *Science (New York, NY)*, vol. 193, no. 4257, p. 969, 1976.

[132] P. J. Bryant, "Pattern formation in the imaginal wing disc of drosophila melanogaster: Fate map, regeneration and duplication," *Journal of Experimental Zoology*, vol. 193, no. 1, pp. 49–77, 1975.

[133] S. A. Kauffman and E. Ling, "Regeneration by complementary wing disc fragments of drosophila melanogaster," *Developmental Biology*, vol. 82, no. 2, pp. 238 – 257, 1981.

[134] R. Sharma and V. Chopra, "Effect of the wingless (wg1) mutation on wing and haltere development in drosophila melanogaster," *Developmental Biology*, vol. 48, no. 2, pp. 461 – 465, 1976.

[135] M. Zecca, K. Basler, and G. Struhl, "Sequential organizing activities of engrailed, hedgehog and decapentaplegic in the drosophila wing," *Development*, vol. 121, no. 8, pp. 2265–2278, 1995.

[136] F. A. Spencer, F. Hoffmann, and W. M. Gelbart, "Decapentaplegic: A gene complex affecting morphogenesis in drosophila melanogaster," *Cell*, vol. 28, no. 3, pp. 451 – 461, 1982.

[137] C. Chen and G. Struhl, "Wingless transduction by the frizzled and frizzled2 proteins of drosophila," *Development*, vol. 126, no. 23, pp. 5441–5452, 1999.

[138] R. Burke and K. Basler, "Dpp receptors are autonomously required for cell proliferation in the entire developing drosophila wing," *Development*, vol. 122, no. 7, pp. 2261–2269, 1996.

[139] D. Rogulja and K. D. Irvine, "Regulation of cell proliferation by a morphogen gradient," *Cell*, vol. 123, no. 3, pp. 449 – 461, 2005.

[140] A. Lander, "Pattern, growth, and control," *Cell Press*, vol. 144, pp. 955 – 969, March 2011.

[141] C. Martin-Castellanos and B. A. Edgar, "A characterization of the effects of dpp signaling on cell growth and proliferation in the drosophila wing," *Development*, vol. 129, no. 4, pp. 1003–1013, 2002.

[142] H. Nijhout, "The control of body size in insects," *Developmental Biology*, vol. 261, no. 1, pp. 1 – 9, 2003.

[143] G. Schwank, G. Tauriello, R. Yagi, E. Kranz, P. Koumoutsakos, and K. Basler, "Antagonistic growth regulation by dpp and fat drives uniform cell proliferation," *Developmental cell*, vol. 20, no. 1, pp. 123–130, 2011.

[144] M. Zecca and G. Struhl, "Control of drosophila wing growth by the vestigial quadrant enhancer," *Development*, vol. 134, no. 16, pp. 3011–3020, 2007.

[145] L. Baena-Lopez and A. García-Bellido, "Control of growth and positional information by the graded vestigial expression pattern in the wing of drosophilamelanogaster," *Proceedings of the National Academy of Sciences*, vol. 103, no. 37, pp. 13734–13739, 2006.

[146] Y. Mao, A. L. Tournier, P. A. Bates, J. E. Gale, N. Tapon, and B. J. Thompson, "Planar polarization of the atypical myosin dachs orients cell divisions in drosophila," *Genes & development*, vol. 25, no. 2, pp. 131–136, 2011.

[147] siskiyou, "Dovetail xyz stages." `http://siskiyou.com/translation-stage_dt100series.shtml`. accessed 2013/06/18.

[148] Smaract, "Simple control units (scu)." `http://www.smaract.de/index.php/products/controlsystems`. accessed 2013/06/18.

[149] Physikinstrumente, "M-531 heavy-duty micropositioning stage." `http://www.physikinstrumente.com/en/pdf/M511_M521_M531_Datasheet.pdf`. accessed 2013/06/21.

[150] A. Biometrix, "Poly-l-lisine." `http://www.purecol.nu/dfu_Poly-L-Lysine.pdf`. accessed 2013/06/23.

[151] "Poly-l-lisine." `http://www4.mpbio.com/ecom/docs/proddata.nsf/%28webtds2%29/150175`.

[152] B. Jacobson and D. Branton, "Plasma membrane: rapid isolation and exposure of the cytoplasmic surface by use of positively charged beads," *Science*, vol. 195, no. 4275, pp. 302–304, 1977.

[153] J. Gere and B. Goodno, *Mechanics of Materials*. Available Titles Cengage NOW Series, Cengage Learning, 2009.

[154] Femtotools, "Ft-s microforce sensing probe." `http://www.femtotools.com/fileadmin/datasheets/FT-S1000_Datasheet.pdf`. accessed 2013/06/22.

[155] D. Currie, M. Milner, and C. Evans, "The growth and differentiation in vitro of leg and wing imaginal disc cells from drosophila melanogaster," *Development*, vol. 102, no. 4, pp. 805–814, 1988.

[156] O. B. Microscopes, "Ix71 inverted microscope." `http://www.olympusamerica.com/seg_section/product.asp?product=1023&c=0`. accessed 2013/07/13.

[157] O. B. Microscopes, "Uplsapo series." `http://microscope.olympus-global.com/uis2/en/uplsapo/`. accessed 2013/07/13.

[158] R. Oldenbourgh, "Lc-polscope." `http://www.mbl.edu/cdp/oldenbourg-lab/lc-polscope/`.

[159] H. Oda and S. Tsukita, "Real-time imaging of cell-cell adherens junctions reveals that drosophila mesoderm invagination begins with two phases of apical constriction of cells," *Journal of Cell Science*, vol. 114, no. 3, pp. 493–501, 2001.

[160] J. S. Rees, N. Lowe, I. M. Armean, J. Roote, G. Johnson, E. Drummond, H. Spriggs, E. Ryder, S. Russell, D. St Johnston, *et al.*, "In vivo analysis of proteomes and interactomes using parallel affinity capture (ipac) coupled to mass spectrometry," *Molecular & Cellular Proteomics*, vol. 10, no. 6, pp. 1–10, 2011.

[161] F. G. Prendergast and K. G. Mann, "Chemical and physical properties of aequorin and the green fluorescent protein isolated from aequorea forskalea," *Biochemistry*, vol. 17, no. 17, pp. 3448–3453, 1978.

[162] R. Y. Tsien, "The green fluorescent protein," *Annual Review of Biochemistry*, vol. 67, no. 1, pp. 509–544, 1998. PMID: 9759496.

[163] H.-A. J. Müller and O. Bossinger, "Molecular networks controlling epithelial cell polarity in development," *Mechanisms of Development*, vol. 120, no. 11, pp. 1231 – 1256, 2003. The Cell in Development.

[164] I. M. L. Somorjai and A. Martinez-Arias, "Wingless signalling alters the levels, subcellular distribution and dynamics of armadillo and e-cadherin in third instar larval wing imaginal discs," *PLoS ONE*, vol. 3, p. e2893, 08 2008.

[165] S. Luschnig. Personal communication.

[166] N. I. of Health, "Imagej - image processing and analysis in java." `http://rsbweb.nih.gov/ij/`. accessed 2013/08/13.

[167] T. J. Widmann and C. Dahmann, "Wingless signaling and the control of cell shape in drosophila wing imaginal discs," *Developmental Biology*, vol. 334, no. 1, pp. 161 – 173, 2009.

[168] D. E. Breen, T. Widmann, L. Bai, F. Jülicher, and C. Dahmann, "Epithelial cell reconstruction and visualization of the developing drosophila wing imaginal disc," in *Biological Data Visualization (BioVis), 2012 IEEE Symposium on*, pp. 77–84, IEEE, 2012.

[169] G. Greaves, A. Greer, R. Lakes, and T. Rouxel, "Poisson's ratio and modern materials," *Nature materials*, vol. 10, no. 11, pp. 823–837, 2011.

[170] S. Timoshenko, S. Woinowsky-Krieger, and S. Woinowsky, *Theory of plates and shells*, vol. 2. McGraw-hill New York, 1959.

[171] D. of Aerospace Engineering Sciences University of Colorado at Boulder, "Introduction to finite element methods (asen 5007)." `http://www.colorado.edu/engineering/cas/courses.d/IFEM.d/IFEM.Ch14.d/IFEM.Ch14.index.html`, 2013. accessed 2013/08/28.

[172] S. Brandt and H. D. Dahmen, *Mechanik: eine Einführung in Experiment und Theorie*. Springer, 1996.

[173] R. Phillips, J. Kondev, J. Theriot, H. Garcia, B. Chasan, *et al.*, "Physical biology of the cell," *American Journal of Physics*, vol. 78, p. 1230, 2010.

[174] L. Figura, "Lebensmittelphysik," in *Taschenbuch für Lebensmittelchemiker*, pp. 1023–1033, Springer, 2006.

[175] I. P. Herman, *Physics of the human body*. Springer, 2007.

[176] D. Y. Leung, S. Glagov, and M. B. Mathews, "Cyclic stretching stimulates synthesis of matrix components by arterial smooth muscle cells in vitro," *Science*, vol. 191, pp. 475–477, June 1976.

[177] S. Dupont, L. Morsut, M. Aragona, E. Enzo, S. Giulitti, M. Cordenonsi, F. Zanconato, J. L. Digabel, M. Forcato, S. Bicciato, N. Elvassore, and S. Piccolo, "Role of YAP/TAZ in mechanotransduction," *Nature*, vol. 474, pp. 179–183, June 2011.

[178] E. Guillemin, *Theory of linear physical systems: theory of physical systems from the viewpoint of classical dynamics, including Fourier methods*. Wiley, 1963.

[179] T. Schluck, U. Nienhaus, T. Aegerter-Wilmsen, and C. Aegerter, "Mechanical control of organ size in the development of the drosophila wing disc," *PLoSOne*, vol. 8, p. e76171, 2013.

[180] U. Nienhaus, T. Aegerter-Wilmsen, and C. Aegerter, "In-vivo imaging of the drosophila wing imaginal disc over time: Novel insights on growth and boundary formation," *PLoS ONE*, vol. 7, no. 10, p. e47594, 2012.

[181] U. Nienhaus. Personal communication.